IMPROVING THE DISCRIMINATION OF UNEXPLODED ORDNANCES

A DISSERTATION
SUBMITTED TO THE DEPARTMENT OF AERONAUTICS & ASTRONAUTICS
AND THE COMMITTEE ON GRADUATE STUDIES
OF STANFORD UNIVERSITY
IN PARTIAL FULFILLMENT OF THE REQUIREMENTS
FOR THE DEGREE OF
DOCTOR OF PHILOSOPHY

Alan Yehren Chen
November 2010

I certify that I have read this dissertation and that, in my opinion, it is fully adequate in scope and quality as a dissertation for the degree of Doctor of Philosophy.

Per Enge, Primary Adviser

I certify that I have read this dissertation and that, in my opinion, it is fully adequate in scope and quality as a dissertation for the degree of Doctor of Philosophy.

Stephen Rock

I certify that I have read this dissertation and that, in my opinion, it is fully adequate in scope and quality as a dissertation for the degree of Doctor of Philosophy.

Sherman Lo

Approved for the Stanford University Committee on Graduate Studies.

Patricia J. Gumport, Vice Provost Graduate Education

This signature page was generated electronically upon submission of this dissertation in electronic format. An original signed hard copy of the signature page is on file in University Archives.

Abstract

UNEXPLODED ORDNANCES, UXOs, are a significant safety and economic problem in the US and worldwide. Typically, they consist of munitions such as rockets, artillery shells, and missiles. They are buried in unknown locations and present a danger due to both their explosive nature and their environmental impact. Across the US, UXOs are suspected to infest over 15 million acres of land consisting of troop training areas, weapons testing sites, and munitions storage facilities. In 2003, the Department of Defense estimated the final cost of clearing all of the US's contaminated lands using existing technologies would be $35 billion. One of the difficult challenges facing UXO clearance work is discriminating whether a detected target is an UXO and needs to be excavated or an inert object that can be left in the ground. An electromagnetic induction, EMI, sensor is commonly used in UXO clearance work. This research introduces two strategies that change the way the EMI sensor is used in order to improve discrimination.

The first strategy is to use more target specific sensor swaths and to use an odometer based positioning system. In most discrimination work, data is first taken with a vehicle driven to cover an entire field. Each sensor measurement is geotagged with GPS information and then the data is post processed. This research shows that a focused search above the estimated target's location using odometry can improve discrimination over the GPS approach because there is less relative error in the sensor position estimates.

The next strategy is to use an adaptive sensing algorithm to determine where to move and how to orient an EMI sensor. Traditionally, the EMI sensor is moved around a field in a fixed orientation. Allowing the sensor to rotate increases the directions at which the target can be illuminated. The adaptive sensing algorithm exploits this new flexibility to

maximize the information obtained during a sensor run, thereby improving UXO discrimination.

Acknowledgements

I have read a large number of dissertations to get inspiration, to learn about algorithms, and to find specific equations. I have tried to develop those ideas into something unique for my thesis. However, one section that is not novel is the acknowledgements section. The simple truth, that all the other dissertations have stated, is that the path to a Ph.D. is not done in a vacuum. In fact, without the help of others, it is impossible. With that in mind, I would like to begin with thanking my advisors.

I have been blessed with being advised by three great individuals who also make up my reading committee. Professor Enge has been everything I could ask for in an advisor and a role model. He gave me the opportunity to explore the research I was interested in and taught me many subjects ranging from GPS to sextants to how Tycho Brahe got his gold nose. While I cannot mimic the impact of his laugh, I can try to copy his leadership and teaching qualities.

Professor Rock has also been a great advisor. He has created a great environment in the Aerospace Robotics Lab, ARL, for students to explore and grow. He allows his students to struggle to find their way, which in the end forces them to become better researchers. He has also taught me to keep an eye on the big picture issues even when I am fully immersed in a specific problem. One of these days, an entrepreneurial student will package Professor Rock's speeches into a book and sell it to prospective Ph.D. students in other labs.

The third member of my reading committee is Dr. Sherman Lo. Not only has he been a great advisor and mentor to me, he has also been a great friend. Countless times I was stuck on some problem in my research. I went up to Sherman's office, and we started brain storming. Each time, I left with a better understanding of the problem and several potential solutions to pursue.

Along with having three mentors, I was also associated with two labs: the ARL and the GPS lab. There were always interesting discussions about particle filters and new Compass signals, but that is not what I will remember. I spanned two generations in the ARL so I had the privilege of being cube mates with Masa and Peter. Fittingly, I went surfing with Masa and played water polo with Peter. Debbie helped facilitate my only dive with MBARI and shared countless coffee trips to break up the frustrating moments in the day of a Ph.D. student. Sean bought me my first celebratory drink after passing my oral defense, and he did it coming straight from soccer. Kristoff helped me build a fish tank stand. Godwin showed me how to repack the bearings of a hub. There are also similar stories involving Prof Cannon, Jason, Daniel, Jack, Jinwhan, Shandor, Kiran, Andrew, Sarah, Nicolas, Eleanor, Roland, Daniel, Teresa, Sungmoon, Aaron, and Gabe. While Gabe was not a part of the ARL he was only across the hall so it is close enough.

In the GPS lab, I had the honor of working with Grace, Di, Tom, Todd, Sam, Dave, Youngshin, Shankar, Jiwon, Lee, Doug, Tsung-Yu, Dennis, and many others. I remember making a huge helical antenna with Grace and spending time on the roof debugging the VSA with Di. Dave was instrumental in getting me into cycling. Being a part of this lab allowed me to see how world experts in a specific field operate and how they bring about real change in the world. It was an enlightening experience.

I am grateful to the Stanford Center for Position Navigation and Time, SCPNT, for funding my research through the Lockheed Martin SCPNT Graduate Student Fellowship. I would also like to thank Geonics Limited and Geometrics for loaning me an EM61-MK2 and a G-858 respectively. It was extremely eye-opening getting hands on experience with the sensors UXO technicians are using in the field. At Ford Ord, Melissa Broadstom, Stan Cook, and Linda Temple were very generous with their time and showed me around the base as well as answered my numerous questions. This gave me a first hand view of actual UXO clearance work and a chance to talk to UXO workers in the field.

None of the above would have been possible without Sherann, Dana, Jay, Robin, Lynn, and Ralph. I have yet to find a question about how to do something or find something at Stanford that Sherann and Dana cannot answer. In one of the few cases where the grass is not greener on the other side, we know how lucky we are to have Sherann and Dana.

I have also been blessed with a lot of friends who have kept me sane though my entire

graduate experience. I would like to thank the crew that began with Yves and developed into Janet, Serena, Alex, Gloria, Eehern, Dave, PJ, and Eric. We have shared many ups and downs that have forever bound us together. I have learned to bike a hundred miles, to survive rails in the terrain park, to play Australian Rules football, and to correctly run a white elephant gift exchange. I have also learned the meaning of true friendship, dedicating your life to others, and fighting to the end. We will miss you Alex.

With my other friends, we have been lucky to have shared many many happy experiences as a group. My MIT friends, there are way too many of you to name, and I have made many trips to Yuma, Vegas, San Diego, Chicago, LA, New York, and Hawaii. All have stories that will be told as long as we are around to tell them. My basketball friends, thank you for allowing me the opportunity to try out my 3-pt shot: Fob Five, Alliance, Schwab Court Legends, and Tues night ball. Last, my roommates Will, Jocelyn, Steve, and Dave. How you put up with me, I'll never know. Thank you.

Last, but definitely not least. My family has supported me through my entire life and I am lucky to be loved by them. My parents have spent their entire adult life making sure that I have no worry outside of school. There is no way I can repay what they have done for me, but I will spend the rest of my life trying. My brother has been a great sounding board anytime I have needed it. I know he is always there for me, and that is a great security blanket to have. Thank you mom, dad, and Howard.

Contents

List of Tables

List of Figures

Chapter 1

Introduction

UNEXPLODED ORDNANCES, UXOs, are a significant safety and economic problem in the US and worldwide. This dissertation investigates two innovative strategies that improve UXO discrimination with existing technologies. The current discrimination approach uses multiple traverses to cover a field with various geophysical sensors and then post processes the GPS tagged data. The first strategy is to replace the GPS system with an odometry based positioning system and perform a localized lawnmower pattern around any potential objects. The second strategy continues the use of an odometer, but adds an adaptive sensing algorithm to determine where to move and how to orient the geophysical sensor. Both changes improve the discrimination ability of UXOs over the current standard.

1.1 Motivation

UXOs, also known as munitions and explosives of concern, consist of armaments such as missiles, mortars, bombs, and rockets [64]. They form when munitions do not detonate upon impact or are part of a forgotten weapons cache. These UXOs are buried in unknown locations and must be excavated because of their explosive nature and their ability to contaminate the local environment. In the US, there are over 15 million acres of land potentially containing UXOs. This area encompasses nearly 2,300 sites which are mainly composed of troop training areas, bombing ranges, and artillery ranges. Around the world, the UXO infested land area skyrockets as old and new battlefields are included. The Department

Figure 1.1: UXO examples

UXOs consist of any type of munition such as missiles, bombs, and artillery rounds. They are commonly characterized as being long, metallic, and axially symmetric. The pictures above show UXOs excavated from Fort Ord in Monterey, CA.

of Defense estimated in 2003 that the total cost of clearing the US of UXOs with current technologies is around $35 billion [27, 58].

The UXO challenge differs from the more commonly known land mine and improvised explosive device, IED, problems. All are obviously important issues, but land mines and IEDs are not found in American military bases being reclaimed for civilian use. UXOs, pictured in Figure 1.1, are also typically long, metallic, and axially symmetric. Mines and IEDs can be of any shape and size, and can be made of many different materials. These key differences make tackling the UXO problem a worthwhile pursuit and a more tractable challenge.

(a) UXO clearance activities

(b) Warning sign

Figure 1.2: Fort Ord

Ford Ord is an active UXO *clearance site in Monterey, CA. (a) The top image shows technicians using a Geonics* EM61HH *metal detector. The flags in the ground mark potential* UXO *locations. (b) The bottom image shows the boundary of a section at Ford Ord that may contain* UXOs*.*

Fort Ord and Pinecastle Jeep Range are two examples of active UXO clearance sites. Ford Ord is a former military base in Monterey, CA that was used from 1917 to 1994 as a training site for Army units. In 1994, the base was closed and its 28,000 acres of land was earmarked for civilian uses such as golf courses, buildings, and nature preserves [39, 72, 81]. Figure 1.2 shows areas in Ford Ord where UXO work is ongoing.

Figure 1.3 shows Odyssey Middle School where in 2008, CNN reported that workers were injured when they accidentally uncovered munitions during renovations of the middle school track. Luckily, no students were harmed. An investigation showed that this school and the surrounding neighborhood had been built on the former Pinecastle Jeep Range. This 12,000 acre base was used during WWII as a bombing range. The Army Corp of Engineers has since excavated over 100 UXOs at the school site alone, and more have been found in the neighboring houses like the ones seen in Figure 1.4 [77].

UXO mitigation at both sites is based on variations of the traditional "MAG and Flag" clearance technique. This decade old strategy uses trained technicians to walk across a field with a metal detector which is typically a magnetometer, MAG . Every time their sensor measures a strong return, the technicians plant a flag at that location. After surveying the entire field, the technicians dig around all the flags. This process finds most of the buried UXOs, but is extremely inefficient. A report by the Defense Science Board Task Force estimates that one percent of the excavations from "MAG and Flag" produced an UXO. Because of the cost and time required for each dig, the government and industry has focused research on trying to reduce the number of false positives [27].

This reduction requires improved discrimination which is different than detection. The goal of detection is to determine if there is something buried in the ground and where is it located. The goal of discrimination is either to identify the "something" or to determine how likely the item is an UXO. This information will help reduce the number of false positives by focusing the dig efforts on sites more likely to contain munitions. Also, discrimination will allow engineers to factor in what type of munition is likely buried here. Camp Sibert is a great example why identifying the munitions is important. The base was formerly used for chemical warfare training and thus contains chemical munitions. Determining which targets are chemical munitions can help prioritize the dig order and assess the risk for each excavation [66].

(a) Odyssey Middle School

(b) Middle school track

Figure 1.3: Pinecastle Jeep Range

These images are from the school where they first discovered UXOs *in an Orlando neighborhood. (a) The top image has flags planted in the ground in front of the school showing where* UXOs *might be buried. (b) The bottom image shows some of the remnants of the clearance work going on around the school* [a].

[a] Nancy J. Sticht. *The Importance of Communication at Pinecastle Jeep Range Formerly Used Defense Site*. US Army Corp of Engineers. March 2009.

(a) Front lawn

(b) Sidewalk

Figure 1.4: Orlando neighborhood

This is the neighborhood around Odyssey Middle School which is also located on the former Pinecastle Jeep Range. These images show clearance work going on in the front lawn of a house and along the sidewalk of the neighborhood [a].

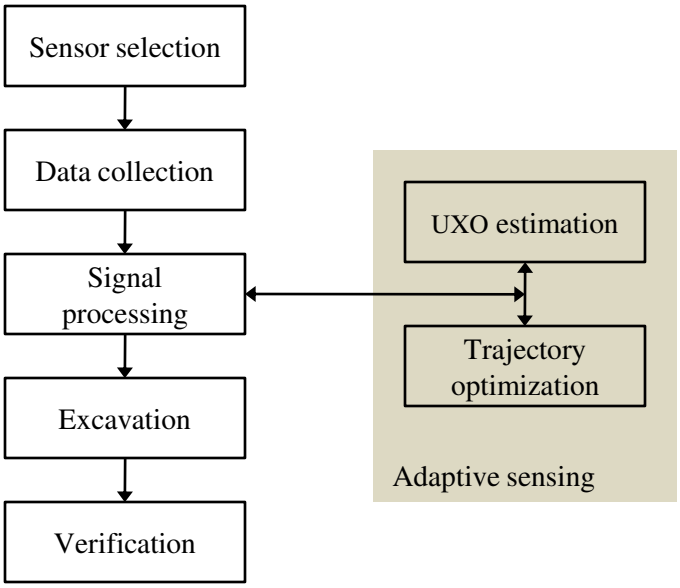

Figure 1.5: UXO clearance flow chart

The typical UXO clearance process can be dissected into the five steps shown on the left. After a suspected target location is found, a sensor can perform a more focused investigation of that area. The right side of the chart shows the new investigation using adaptive sensing. After the new measurements are taken, the data can be fed back into the previous signal processing techniques for improved discrimination.

1.2 UXO Discrimination

Clearing a site of UXOs can be broken down into five steps which are shown in Figure 1.5. The first step is to select the geophysical sensors based on the local environment. The second step is to collect geotagged data. The data is then post processed to create a list of possible UXO locations. Finally, likely UXO locations are excavated and the entire site is rechecked to verify clearance. The rest of this section will cover some of the related work for the first three steps and how they relate to this research. Many of the cited works actually span several steps, but for the sake of brevity only key concepts are extracted from each citation.

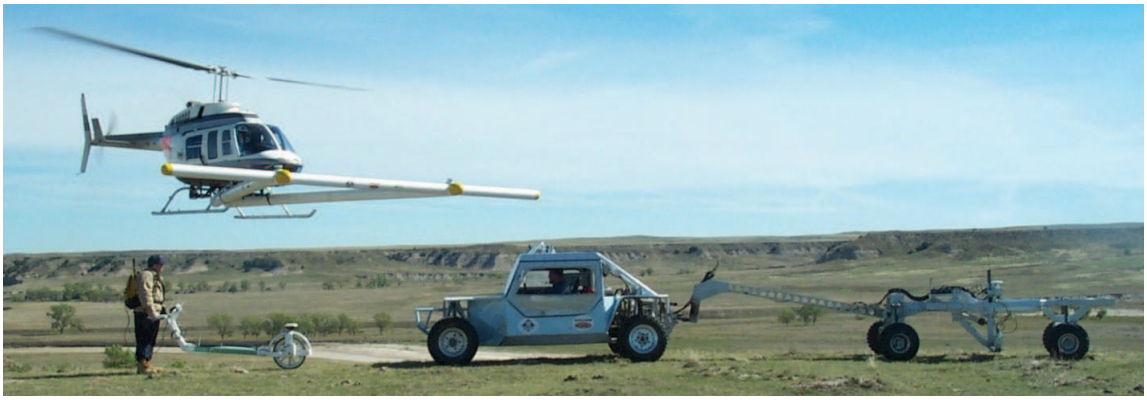

Figure 1.6: Multi-sensor towed array detection system, MTADS

Designed to improve and to speed up UXO *detection,* MTADS *can be towed by vehicle, pushed by man, or mounted onto an airborne vehicle. It is currently operated by the* US *Naval Research Laboratory. This image is courtesy of http://mtads.nrl.navy.mil/.*

Sensor selection is extremely important because it can fundamentally limit the information gathered for UXO clearance [90]. As such, there are several promising fields of research aimed at improving sensor technology. The first line of research is to improve the standard metal detectors: Magnetometers, MAGs, and electromagnetic induction, EMI, sensors [14, 30, 61, 92, 93]. Researchers are also using sensors that exploit non-metal related characteristics of UXOs. Ground penetrating radars, GPR, are the most popular of this class. Other technologies being developed include nuclear quadrupole resonance, x-rays, electra-optical, thermal, hyperspectral imaging, acousto-electromagnetic, and chemical sensors [2, 24, 27, 84]. There are even dogs and bees being used to find explosives [57].

Instead of just using individual sensors, several groups are trying to fuse combinations of MAGs, GPRs, and EMI sensors. This improves the aggregate discriminatory abilities of the systems by allowing the sensors to complement each other's weaknesses [21, 25, 65, 69, 85, 107, 108].

Two groups are also introducing optimality into configurations of EMI sensors and of MAGs. Billings and Wright look into optimal configurations of MAGs for use on a low-flying helicopter [13]. Morrison et al. investigates an optimal EMI sensor configuration by combining several transmitters and receivers. Their approach is to minimize the sum of squared errors when estimating certain UXO parameters. The system allows them to not

worry about the absolute position of the sensor because the parameters can be estimated with measurements taken at one location. Unfortunately, once the sensor model changes or the target is not directly under the sensor, the optimality breaks down [63].

The next step after sensor selection is to collect geotagged measurements. Lines are typically used to ensure that the entire field is traversed and no UXOs are left behind. The geophysical sensors can be hand held or mounted onto vehicles like a helicopter [8, 26, 67, 68, 81, 94]. The measurements are commonly geotagged with GPS, but other positioning options can be used, such as a laser or a vision based system.

Researchers have also focused on how and where to take the sensor measurements. Norton and Bell use a cued approach to gather data with high position fidelity. They propose putting a gridded pattern on top of a suspected location and taking manual measurements at each marker on the pattern [9, 70]. These manual strategies test the patience and capabilities of human operators in a stressful environment. This dissertation proposes methods that simplify and potentially automate this effort.

Finally, the geotagged data is post processed to form a dig list that marks locations of potential UXOs. The research into improving this process is focused on the sensor models and applying statistical methods. The models describe the way an object looks to the geophysical sensor and can account for some noise sources such as soil and sensor positioning. Researches studying EMI models have looked at the decay rates in the time domain and at the spectrum in the frequency domain [4, 5, 6, 7, 34, 73, 75, 86, 87, 88, 89, 96]. Billings uses a MAG to measure each target's magnetic field for discrimination. He theorizes that ordnances lose their remnant magnetization when they hit the ground. The remaining magnetic field is from an induced magnetization and is related to the Earth's magnetic field [12]. Collins et al. have taken the sensor models and used advanced statistical methods to determine if an object is an UXO [20, 22]. Beran and Zhang et al. are also applying machine learning algorithms to UXO data sets [11, 105].

This work improves discrimination by introducing a reinvestigation step integrated with the signal processing step. Figure 1.5 shows a block diagram of one potential reinvestigation strategy based on adaptive sensing.

1.3 New Approach

Two reinvestigating strategies that improve UXO discrimination are described here. They make four key assumptions.

- **An EMI sensor is used to discriminate UXOs.**
  Chapter 2 explains that an EMI sensor is chosen because of its discriminatory abilities. Other discrimination capable sensors can be used with these methods. Appendix B shows UXO localization with a MAG.

- **A target library exists.**
  The library allows the discrimination algorithm to incorporate knowledge about real objects in the area and has been used before by Norton and Pasion [70, 75]. This library can be obtained through examining the site history or by sampling a number of suspected UXO locations.

- **A target is in the local area**
  A localized search focuses on an area containing a suspected target. This suspected area can be determined through an initial wide area scan and a post processing step. Any potential target location would then be investigated. A second option is to perform a raster scan of the area and to switch into an investigation mode when something is detected.

- **Each target has no neighboring targets.**
  This eliminates potential ambiguities resulting from multiple targets each contributing to the measurement. Chapter 6 discusses ways to eliminate this assumption.

The first strategy, described herein, is a localized lawnmower investigation about each suspected UXO location using odometry based positioning. The localized search decreases the range between a target and a neighboring object at which the second object will influence the measurements. It also reduces the total distance the sensor must travel, thereby allowing the use of an odometry system for positioning. Chapter 3 shows that the lawnmower pattern is particularly suited for reducing relative sensor positioning error for an odometry system. It also describes why that reduction improves discrimination.

The second strategy, described herein, uses adaptive sensing to decide where to move and how to orient the sensors in order to maximize information about the UXO. Cargile mentions this possibility when she indicates "that there may be advantages to providing real-time feedback to the UXO survey crews so that they may collect additional sensor data (in orthogonal directions) over suspected anomalies, rather than blindly surveying lanes with fixed lane widths and sampling rates" [17]. This adaptive algorithm can be implemented on an autonomous sensor platform.

1.4 Adaptive Sensing

Adaptive sensing aims to optimize a set of future sensor actions to maximize some information metric about a target. It is also known as active sensing, and is strongly related to sensor management. Sensor management is used to decide which sensor to activate as opposed to where to move the sensor. In both cases, the final goal is to perform some set of actions to learn more about a target or a set of targets. The first half of this section gives some breadth to the adaptive sensing field. The second half contains algorithms that are closely or directly related to performing adaptive sensing for UXO work.

There are two main ways to distinguish each adaptive sensing algorithm. The first major distinction is the cost function that represents the information which can be based on entropy, uncertainty, or several other possibilities. Each option quantifies information in a slightly different format and requires a different way to calculate the cost. The second major identifier is the type of sensor and target being considered. This affects the number of states that the algorithm has to consider and the complexity of the sensor and target models.

Researchers often use a target estimate's covariance matrix to quantify the information known about a set of target parameters. This work will also use the covariance matrix, but will implement it in a different manner than the following researchers. Kim and Rock design an optimal controller that allows an autonomous underwater vehicle, AUV, using a bearings only sensor to minimize the uncertainty about a target's location while simultaneously trying to dock with the target. This optimal characteristic is very unique for adaptive

sensing algorithms [45]. Using monocular vision, Frew and Rock use a tree search approach to plan a path that estimates a target's current location and velocity vector. This trajectory can be based on minimizing uncertainty in a given time or minimizing the time it takes to reach some certainty level [28, 29]. Whitacre et al. use a camera and a receding horizon approach to optimize flight path parameters for two unmanned aerial vehicles, UAV, performing surveillance on a single target. The information metric is a function of the covariance matrix at the current horizon. Each aircrafts' flight path is constrained to be an orbit of constant radius and altitude [103]. Chung et al. propose an adaptive sensing algorithm that can be decentralized and can incorporate noisy inter-vehicle communications into the information metric. In its current form, the technique requires linearized models for the sensors and any state dynamics [19]. Gupta et al. attacks the sensor scheduling problem with an uncertainty based cost metric. This metric tells the algorithm what probability distributions to assign to each sensor so that they can be stochastically activated. The advantage of randomly choosing sensors allows the algorithm to be more numerically tractable and not rely on each sensor possessing extensive knowledge about the other sensors [36]. Kalandros et al. attempt to obtain a certain amount of knowledge about several targets. They determine which sensor to use based on which can contribute the most to getting each target's state uncertainty to a specific threshold level. Once the threshold is reached, the sensors concentrate on the other targets [42, 43]. Zhang and Leonard develop an accurate contour map by smartly shaping a formation of sensors. The adaptive technique tries to minimize the mean square error of the estimate of the scalar field and its gradient [106].

Instead of using the covariance matrix, another set of researchers use entropy or Shannon's information to produce an information metric. They are all intimately related, and their relationships are detailed in Section 4.2.

Ryan uses entropy to assist an UAV in tracking ground targets with cameras. She combines a particle filter with receding horizon control for the adaptive process. Because particle filters can be computationally expensive, she has developed a technique to approximate entropy from the particle distribution [83]. Amigoni and Caglioti use a greedy approach with a laser scanner for adaptive sensing. The entropy is combined with the effect of dead reckoning error to formulate a cost metric to create an efficient map building robot [3].

Zhao et al. uses entropy for sensor management. They determine which sensor in a static array to use in order to track a target moving through the system [110]. Grocholsky's thesis does an extensive job examining information-theoretic approaches to controlling multiple sensor platforms. He uses entropy combined with mutual information to help decentralize the adaptive sensing problem [35]. Rigby and Williams use adaptive sensing to plan the best trajectory for an AUV to fly to self localize given a digital elevation map. The entropy based method uses sonar as the localization sensor [82].

Shannon's information is another popular information metric. Klesh et al. uses it to help plan UAV trajectories to learn a base amount of information about multiple target as quickly as possible. An omnidirectional radar is the sensor of choice and its signal-to-noise ratio, which is dependent on the range to a target, is used to determine the rate at which information can be gained [46]. Sujan and Dubowsky use Shannon's information to fill out an occupancy grid based on geometric models. The adaptive sensing determines where a camera should go next to explore quickly an unknown environment [95].

Whereas uncertainty, entropy, and Shannon's information deal with the states representing a target's parameters, other researchers use an approach that requires a decision to be made or an approach that tries to maximize discriminators. Tisdale et al. uses a receding time horizon approach based on maximizing the probability of detecting a stationary target. This technique is applied to plan the paths of a team of UAVs equipped with cameras searching for a single target [99]. Kreucher et al. use Renyi divergence to find measurements that best separates two hypotheses. In simulation, the adaptive sensing algorithm is used to determine which processing action is used: a ground moving target indication mode or a synthetic aperture radar mode [52].

Most of the above applications are based on sensors such as radar, sonar, or vision. When more nonlinear sensor models are used, the approaches begin to fail. The following researchers have developed algorithms that are more closely related to the type of sensors used in UXO work or are directly used for UXO discrimination.

Hoffmann and Tomlin uses mutual information to plan the trajectory of their vehicles. The algorithm allows the system to be decentralized as it looks for avalanche beacons. Their sensor detects magnetic dipoles produced by the beacon in a similar manner to the way some sensors locate UXOs. The technique will be used as a point of comparison

in Section 4.4 because of how it handles the nonlinear equations describing the beacon [37, 38]. However, the algorithm they use to estimate the target's parameters scales poorly in terms of time as the number of parameters increase. Pinies et al. also look at these beacons, but their search algorithm is more deterministic. It searches along field lines and then approaches the estimated target location. [78, 79, 80]

Researchers at Duke University have begun applying adaptive sensing to the UXO and mine problem. Kolba and Collins use discrimination ability as their metric for mine detection. They are trying to solve the sensor management problem where their algorithm investigates a discretized field trying to decide if a mine is in a grid location or not. The information metric is dependent on the probability of detection and the false alarm rate for any sensor being considered. The management system uses a greedy search to help more efficiently use EMI and GPR sensors for mine detection [47, 48, 49, 50, 51]. By using discrimination ability as a metric, the discriminators are focused only on differentiating two hypothesis which means it ignores other possibilities and it does not try to maximize the information about the target parameters. Liao and Carin apply an adaptive sensing algorithm to an EMI sensor to perform UXO discrimination. They show that for the same number of measurements, adaptive sensing can improve on parameter estimation over a grid search. This comparison does not take into account that the target is centered in the search area and so the grid search will take more measurements to reach the target location. Also, Fisher's information matrix is used to quantify the information obtained in each new potential measurement, but the linearization step required does not handle large initial uncertainties well. Their approach takes the result from the adaptive sensing algorithm and uses it as an initial guess to feed into a partially observable Markov decision process to help classify the target. The Markov decision process grows exponentially with the number of states and requires a discretized list of possible actions [18, 55].

The adaptive sensing in this thesis addresses many of the previously mentioned problems. The contributions of which, are listed in this next section.

1.5 Contributions

Two new strategies are recommended to the UXO community to improve UXO discrimination. These suggestions are supported by the following contributions:

- **Designed and implemented a local odometry based search to compete with an existing GPS based search for UXO discrimination.**
  Existing UXO discrimination strategies require GPS tagged measurements that cover the entire field. A localized odometry based lawnmower trajectory is shown to have better relative positioning accuracy even when the absolute positioning accuracy is worse than the positioning accuracy provided by GPS. This translates into an improved ability to discriminate.

- **Developed an algorithm that adapts a sensor trajectory to seek information for geophysical sensors tuned for UXO investigations.**
  An adaptive sensing framework is developed that is fast and can handle highly nonlinear sensor functions with large state vectors. This approach uses the square root form of the eigenvector sigma-point Kalman filter. This particular estimator is rotationally invariant so it eliminates any bias that is not related to the sensor model but due to the sensor location relative to the target.

- **Adapted and validated adaptive sensing for UXO discrimination with an EMI sensor.**
  A library of targets is established with real data. An estimator is designed to integrate this library into the adaptive sensing framework. Simulations are run that show an adaptive sensing strategy using odometry can improve UXO discrimination.

1.6 Roadmap

Chapter 1: Introduction discusses the motivation and contributions of this research. It also presents related work from the UXO and the adaptive sensing communities.
Chapter 2: Discrimination with an Electromagnetic Induction Sensor introduces the sensor that is used to discriminate UXOs along with its measurement model and fit metric.

Real sensor data is used to develop a sample target library that is used for discrimination evaluations throughout the thesis.

Chapter 3: Local Search details the affects of a GPS error model as compared to an odometry error model on various localized searches. Simulation results with an EMI sensor running a localized lawnmower search are shown for both cases.

Chapter 4: Adaptive Sensing presents the estimator, cost function, and optimizer used to plan a trajectory that maximizes the information gathered about a target. This final selection is made after an analysis of alternative estimators and cost functions.

Chapter 5: Adaptive Sensing with an EMI Sensor develops an estimator for the adaptive sensing framework that accounts for a target library. Simulations are then used to show the adaptive sensing algorithm using an EMI sensor for UXO discrimination.

Chapter 6: Conclusion summarizes the contributions of this thesis and presents possible future directions of this work.

Chapter 2

Discrimination with an Electromagnetic Induction Sensor

THE ELECTROMAGNETIC INDUCTION, EMI, SENSOR is used throughout this thesis for the discrimination of unexploded ordnances, UXO. This chapter discusses why that sensor was chosen, the physics behind its operation, and how it is used for discrimination. Finally, a Geonics EM61-MK2 is used to gather data and to produce a target library used in future simulations.

The most commonly used UXO sensors are magnetometers, MAGs, ground penetrating radars, GPRs, and EMI sensors. Figure 2.1c shows an EMI sensor which is an active sensor that returns a measurement dependent on the metallic object's shape, size, and material. It is often used for discrimination [22]. Figure 2.1b shows a total-field MAG which is a passive sensor that measures a component of the local magnetic field. Unfortunately, discrimination is difficult because both an UXO and a random ferrous object can produce magnetic fields that look like they originate from a dipole. Billings theorizes that discrimination can still be done because the dipole's orientation is related to Earth's magnetic field. However, he admits that additional research still needs to be performed on this approach before it is applicable in the field [12]. Figure 2.1a shows a GPR which is an active sensor that transmits a radio wave into the ground. The sensor measures the time and strength of the reflected wave producing a map of the boundary between dielectric constant layers. This can detect buried objects, but is sensitive to clutter and to the soil type [85].

(a) Geophysical Survey Systems UtilityScan

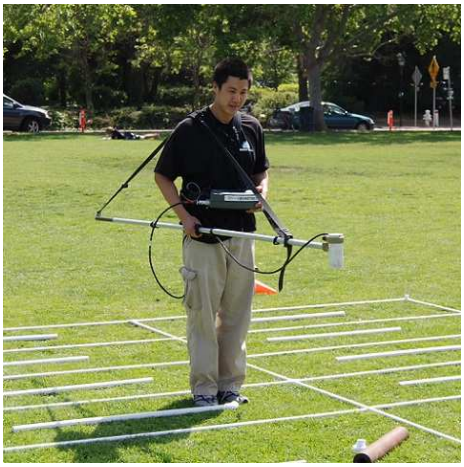

(b) Geometrics G-858 MagMapper

(c) Geonics EM61-MK2

Figure 2.1: Geophysical sensors used in UXO clearance

(a) The UtilityScan is a GPR *that maps the boundary between layers of equal dielectric constant* [a]. *(b) The* G-858 *is a total-field Cesium* MAG *that maps out the strength of the local magnetic field in the direction of Earth's magnetic field. (c) The* EM61-MK2 *is a time domain* EMI *sensor being used at the former Pinecastle jeep Range* [b].

[a] *UtilityScan Brochure*, Geophysical Survey Systems, Inc, July 2009, www.geophysics.com.

[b] Nancy J. Sticht. *The Importance of Communication at Pinecastle Jeep Range Formerly Used Defense Site*. US Army Corp of Engineers. March 2009.

2.1 Principles of Operation

This section summarizes several different sources to explain how an EMI sensor operates as an active metal detector. It is depicted as a loop in Figure 2.2a. This loop represents a coil of wire that allows the sensor to produce and detect magnetic fields. A current is forced through the coil to generate a magnetic field using Ampere's law. Figure 2.2b shows a magnetic dipole that resembles the actual field if it is observed at a distance much greater than the radius of the coil. Equations 2.1 and 2.2 are the cartesian and spherical dipole equations showing the magnetic field at the target location. The origin of both frames is the center of the coil and the spherical coordinate frame is defined with the dipole axis being the z-axis [44]. The strength of the magnetic field falls off with the distance cubed. $\vec{B}$ is the magnetic field and has units of T or nT. The permeability of free space, μ_0, is $4\pi \times 10^{-7} \frac{N}{A^2}$. The magnetic dipole moment, $\vec{m}$, has units of Am^2 and the location of the target relative to the origin, $\vec{r}$, is in m.

$$\vec{B}_{xyz} = \frac{\mu_0}{4\pi}\left(3(\vec{m}\cdot\vec{r})\frac{\vec{r}}{|\vec{r}|^5} - \frac{\vec{m}}{|\vec{r}|^3}\right) \tag{2.1}$$

$$\vec{B}_{r\theta\phi} = \frac{2\mu_0|\vec{m}|}{4\pi|\vec{r}|^3}\cos\theta\hat{r} + \frac{\mu_0|\vec{m}|}{4\pi|\vec{r}|^3}\sin\theta\hat{\theta} + 0\hat{\phi} \tag{2.2}$$

The loop current is cut off causing the primary dipole to disappear. Faraday's law states that the change in magnetic field will induce eddy currents inside the target which is shown in Figure 2.2c. In accord with Lenz's Law, these currents will try to produce a magnetic field that maintains the disappearing primary field [74]. The currents will decay as a function of the object's shape, size, and material and is represented by the equivalent dipole polarizability rates composed of three principal moments, with units of $\frac{Am^2}{Ts}$, aligned with a target centric coordinate frame [10, 63, 73]. UXOs are typically modeled with just an axial, L_a, and a transverse, L_t, component because they are long and axially symmetric.

Figure 2.2d shows the decaying secondary magnetic field originating from the eddy currents in the target and is described in Equation 2.3. The primary magnetic field at the target created by the sensor is $\vec{B}_0^p$. The rotation matrix, R, rotates the frame of the magnetic field to a target fixed coordinate frame. The first rotation, ϕ, is around the original z-axis followed by a rotation, θ, around the new y-axis. The magnetic field expressed in the target frame is then multiplied by the axial and transverse components to get the dipole

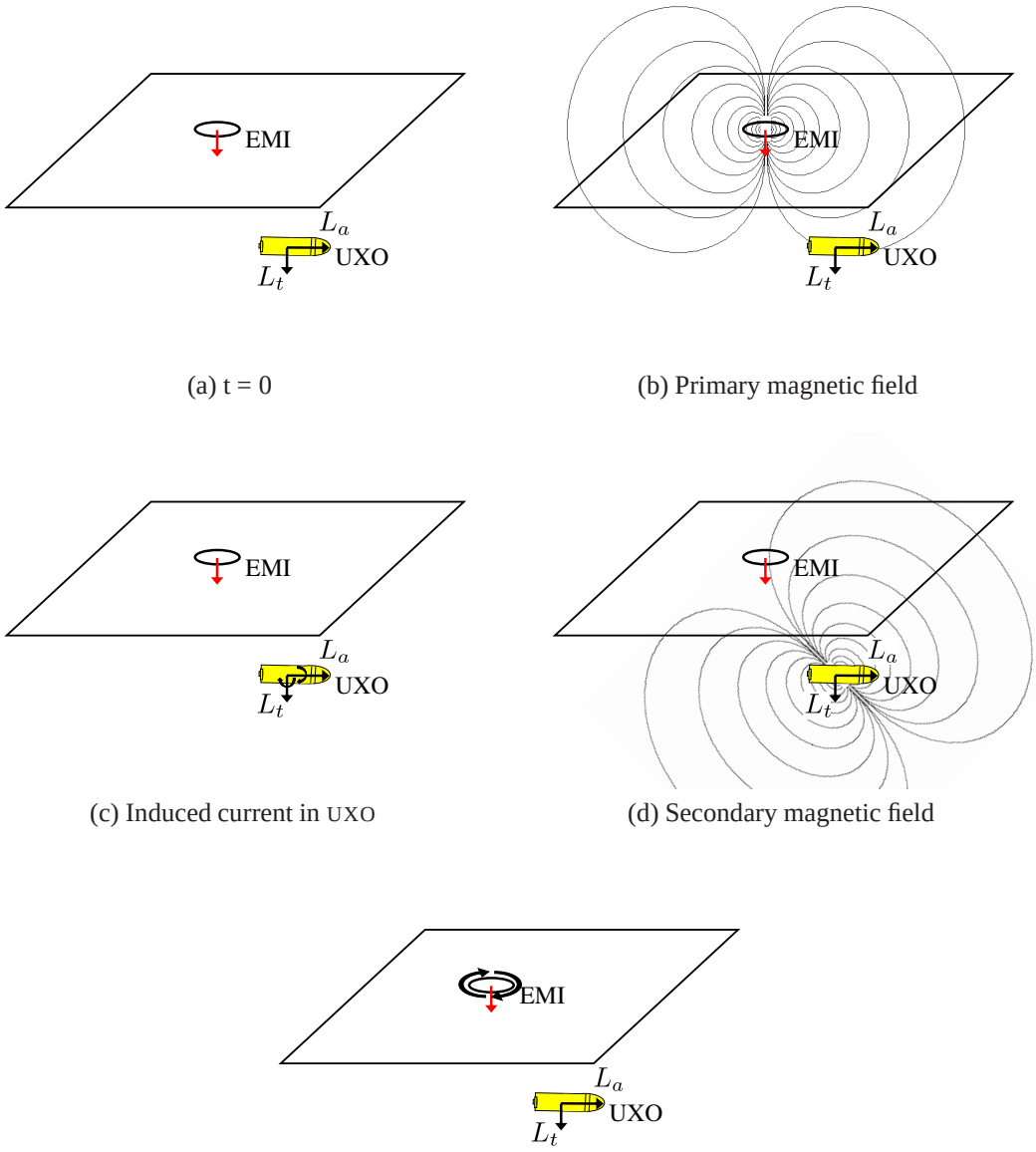

(a) t = 0

(b) Primary magnetic field

(c) Induced current in UXO

(d) Secondary magnetic field

(e) Measured response

Figure 2.2: Description of EMI physics

These cartoon images depict the interactions between an EMI *sensor and an* UXO. *Each successive figure corresponds with the order of events for taking a measurement. The total amount of time from beginning to end is in the order of milliseconds.*

moment response. This response is rotated back to a world frame. Finally, $\frac{d\vec{B}^s}{dt}$ is found by summing the magnetic field contributions from each component of the dipole response. $\vec{B}_i^d$ is the magnetic field at the sensor caused by a unit strength dipole in the i-axis at the target and has units of $\frac{T}{Am^2}$.

$$\frac{d\vec{B}^s}{dt} = \left(\begin{bmatrix} \vec{B}_x^d & \vec{B}_y^d & \vec{B}_z^d \end{bmatrix} R^T \begin{bmatrix} L_t & & \\ & L_t & \\ & & L_a \end{bmatrix} R\vec{B}_0^p \right) \tag{2.3}$$

$$R = \begin{bmatrix} \cos\theta\cos\phi & \cos\theta\sin\phi & -\sin\theta \\ -\sin\phi & \cos\phi & 0 \\ \sin\theta\cos\phi & \sin\theta\sin\phi & \cos\theta \end{bmatrix} \tag{2.4}$$

By Faraday's law, the decaying component of the magnetic field along the normal vector, $\hat{s}$, of the sensor is proportional, k, to the induced electromotive force. This proportionality constant is related to the physical makeup of the receiving coil and has units of $\frac{Vs}{T}$ which produces a scalar sensor measurement with units of V. This final measurement dies off at a rate of $\frac{1}{|\vec{r}|^6}$ which is the product of two $\frac{1}{|\vec{r}|^3}$ components. The first $\frac{1}{|\vec{r}|^3}$ is due to the strength of the primary magnetic field at the target and the second contribution results from the secondary magnetic field response.

$$z = k\hat{s} \cdot \frac{d\vec{B}^s}{dt} \tag{2.5}$$

The state vectors of the sensor and of the target are shown below. The target has five extrinsic parameters relating to the location and orientation of the UXO and two intrinsic parameters corresponding to the size, shape, and makeup of the target. The EMI sensor states relate to its position and orientation.

$$x_{\text{UXO}} = \begin{bmatrix} \vec{r} \\ \theta \\ \phi \\ L_a \\ L_t \end{bmatrix}_{7\times 1} \tag{2.6}$$

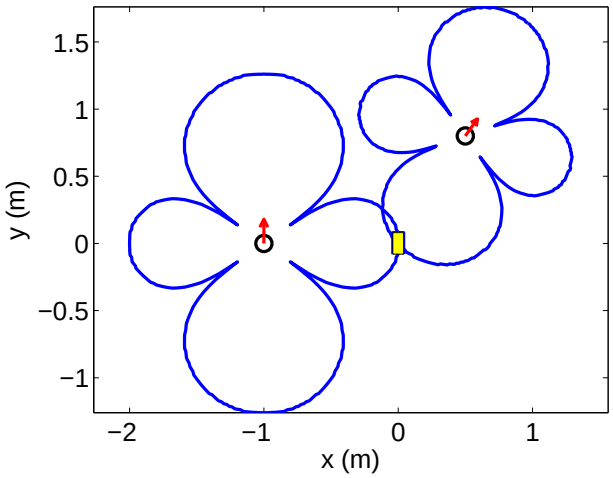

Figure 2.3: EMI sensor contour

This shows two 2D EMI sensor contours. These contours represent target locations where the sensor, centered inside each respective contour, would return the same measurement assuming the orientation of the UXO is fixed.

$$\theta_{\text{EMI}} = \begin{bmatrix} \vec{r} \\ \theta \\ \phi \end{bmatrix}_{5\times 1} \tag{2.7}$$

Figure 2.3 shows the sensor contours for a 2D scenario. If the relative orientation between the UXO and the sensor stays constant, then each sensor's contour represents target locations that will return the same measurement. The two sensors shown are in different orientations. This difference causes their respective contours to change. From a high level, the target's parameters are estimated by finding the intersection between contours drawn from knowing the relative locations and orientations of the sensors for each measurement.

In the worst case scenario, if the two measurements are taken from the same location and orientation, then the sensor contours would overlap. The UXO could reside anywhere along the sensor contour, and still fit the measurements extremely well. There is still some gain however. For each orientation and set of intrinsic UXO parameters, sensor noise manifests itself as a thickness in the sensor contour. As more readings are taken from the same location, the thickness of the sensor contour will shrink.

(a) Rear view (b) Side view

Figure 2.4: Geonics EM61-MK2

Geonics was kind enough to loan this instrument for this research. The transmit and receive coils are located in the bottom rectangular frame parallel to the ground. There is an additional receive coil in the top rectangle that is unused. The battery is located at the center of the coil. Near the handle on the right hand side is the electronic box used to operate the instrument. The device at the center is a portable field computer that allows the user to interface with the instrument to control the sensor settings and to record data.

2.2 Geonics EM61-MK2

Geonics EM61-MK2, shown in Figure 2.4, is a time domain EMI sensor commonly used in UXO clearance. The time domain sensor pulses a magnetic field and then measures the response while the transmitter is quiet. A frequency domain sensor produces a continuous time varying magnetic field and then subtracts out the transmitted signal from the measured response.

The EM61-MK2 produces a rectangular waveform with a 25% duty cycle. The transmit and receive coils are $1m \times 0.5m$. Measurements are taken at 216μs, 366μs, 660μs, and 1266μs after the transmit signal stops. Measurements up to 10,000mV are recorded with 18 bits and can be taken at 16Hz, every 20cm, or when manually triggered [32, 33].

The dipole in the previous section was modeled as a dipole emanating from a small circular coil. For the actual EM61-MK2 sensor, that assumption is not true. Equation 2.8

shows the magnetic field produced by a rectangular coil with dimensions $2b \times 2a$ [62]. The coordinate frame's origin is the center of the coil with the z-axis normal to the coil. The current in the coil, I, affects the strength of the magnetic field like a dipole moment oriented in the z-axis. This equation replaces Equation 2.1 when treating the sensor as a rectangular coil instead of a dipole.

$$\vec{r} = \begin{bmatrix} x \\ y \\ z \end{bmatrix}$$

$$\begin{aligned} C_1 = -C_4 = a + x \qquad & d_1 = d_2 = y + b \\ C_2 = -C_3 = a - x \qquad & d_3 = d_4 = y - b \end{aligned}$$

$$\begin{aligned} r_1 &= \sqrt{(a+x)^2 + (y+b)^2 + z^2} \\ r_2 &= \sqrt{(a-x)^2 + (y+b)^2 + z^2} \\ r_3 &= \sqrt{(a-x)^2 + (y-b)^2 + z^2} \\ r_4 &= \sqrt{(a+x)^2 + (y-b)^2 + z^2} \end{aligned}$$

$$\vec{B} = \frac{\mu_0 I}{4\pi} \begin{bmatrix} \sum_{\alpha=0}^{4} \left[\frac{(-1)^{\alpha+1} z}{r_\alpha (r_\alpha + d_\alpha)} \right] \\ \sum_{\alpha=0}^{4} \left[\frac{(-1)^{\alpha+1} z}{r_\alpha (r_\alpha + (-1)^{\alpha+1} C_\alpha)} \right] \\ \sum_{\alpha=0}^{4} \left[\frac{(-1)^{\alpha} d_\alpha}{r_\alpha (r_\alpha + (-1)^{\alpha+1} C_\alpha)} - \frac{C_\alpha}{r_\alpha (r_\alpha + d_\alpha)} \right] \end{bmatrix} \tag{2.8}$$

2.2.1 Field Tests

The sensor was taken outdoors in Figure 2.5 for field tests to verify the sensor models. A rectangular grid was setup at two sites on Stanford's campus with the dimensions $4.5m$ $\times$ $2.7m$. In most of the trials, the objects were placed on the ground. Some data was taken to see if burying the object had any effect on the sensor models. No differences were

Figure 2.5: Field tests

Test areas were setup in open fields on the Stanford campus. The measurements were used to identify L_a and L_t for a set of objects to create a target library. In the bottom image, the target was buried to see if it affected the sensor model.

(a) Rod

(b) UXO

(c) Plate

Figure 2.6: Test objects

These are the objects used during testing. The rod and the UXO *are similarly axial symmetric. The plate is an object of similar size but different shape. All the objects are steel.*

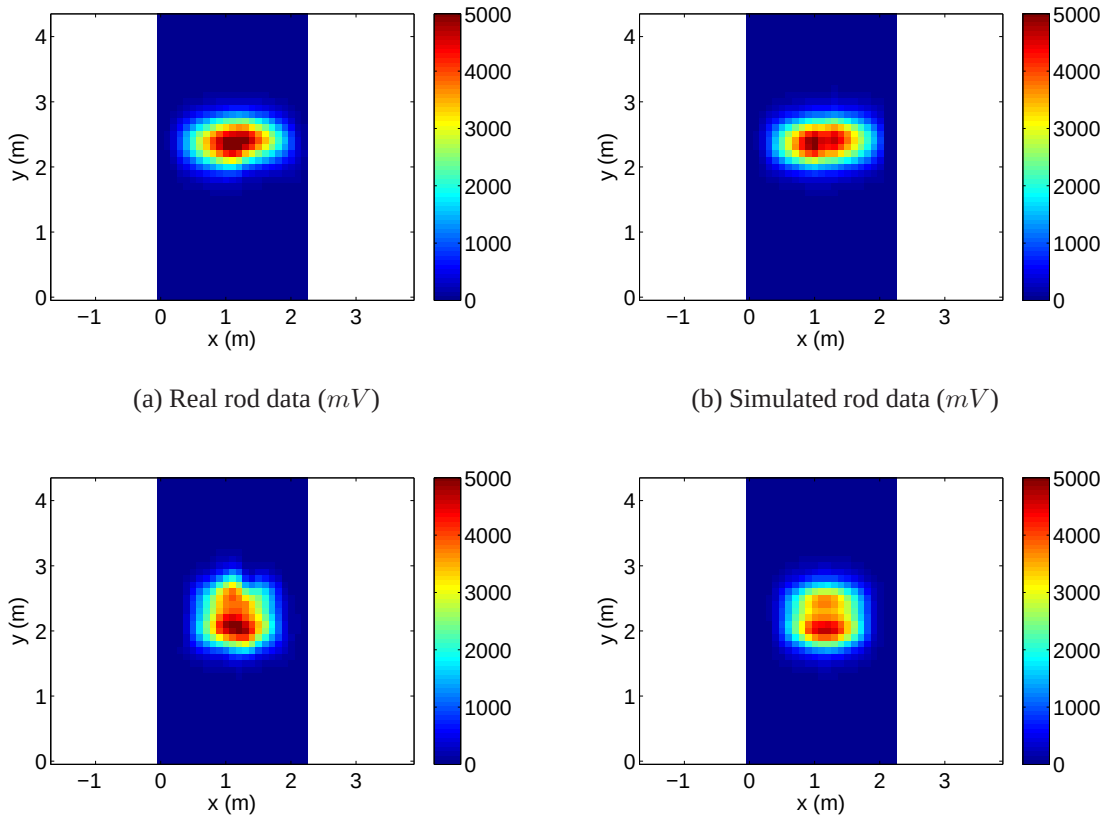

(a) Real rod data (mV)

(b) Simulated rod data (mV)

(c) Real UXO data (mV)

(d) Simulated UXO data (mV)

Figure 2.7: Real vs. simulated measurements

Several sets of data were gathered with each object. The measurements were taken at discrete locations and a contour map was generated. The left column shows a single set of measurements for a rod and an UXO*. The right column shows corresponding simulated data based on the models. The parameters of each target were obtained by fitting the sensor model to the data.*

found. Each data set consisted of several lines of measurements taken along the length of the grid. The sensor was pushed at a constant rate while data was collected at $16Hz$. The objects used are shown in Figure 2.6. They were chosen to be roughly the same size so the magnitudes of the responses would not be drastically different. A plate was added for geometric diversity in the objects. The rod is $54cm$ long, the UXO is $58cm$ long, and the plate is $24cm \times 20cm$. Measurement contour maps of real and simulated data are shown for two of the objects in Figure 2.7. Each cell in the figures represents the EMI measurement taken from that location. The simulated data is based on a set of parameters that best fit the sensor models to the real data.

2.2.2 Target Library

Each data set was fit to the sensor models to calculate L_a and L_t for that object. Knowing the strength of the transmit signal and the measured response of the received signal at several different locations allows the algorithm to map out the magnetic field and thereby estimate the target's location and response strength. If only the shape of the magnetic field is known, the location of the target can still be estimated but only the ratio of the dipole response parameters can be found. The resulting parameters are plotted in Figure 2.8. The fit was done by minimizing the goodness of fit metric which is a least squares fit weighted by the expected noise levels and normalized by the degrees of freedom [1, 22]. It produces similar results as the fit metrics used by Morrison et al. and Pasion [63, 75]. Goodness of fit will be used in future sections to compare algorithms. Note that the name goodness of fit is misleading because the better the fit, the lower its value.

Fitting is done with the constrained optimization routine in Equation 2.9 to estimate x_{UXO} which has n states. It is simultaneously trying to find the best position, orientation, and dipole response parameters of the target that fit a set of M measurements. The sensor function used is the EMI sensor model in Equation 2.5. The minimization used was MATLAB's `lsqnonlin` function which defaults to a trust region method based on the interior reflective Newton method [59]. Levenberg-Marquardt could also be used for minimization in this situation.

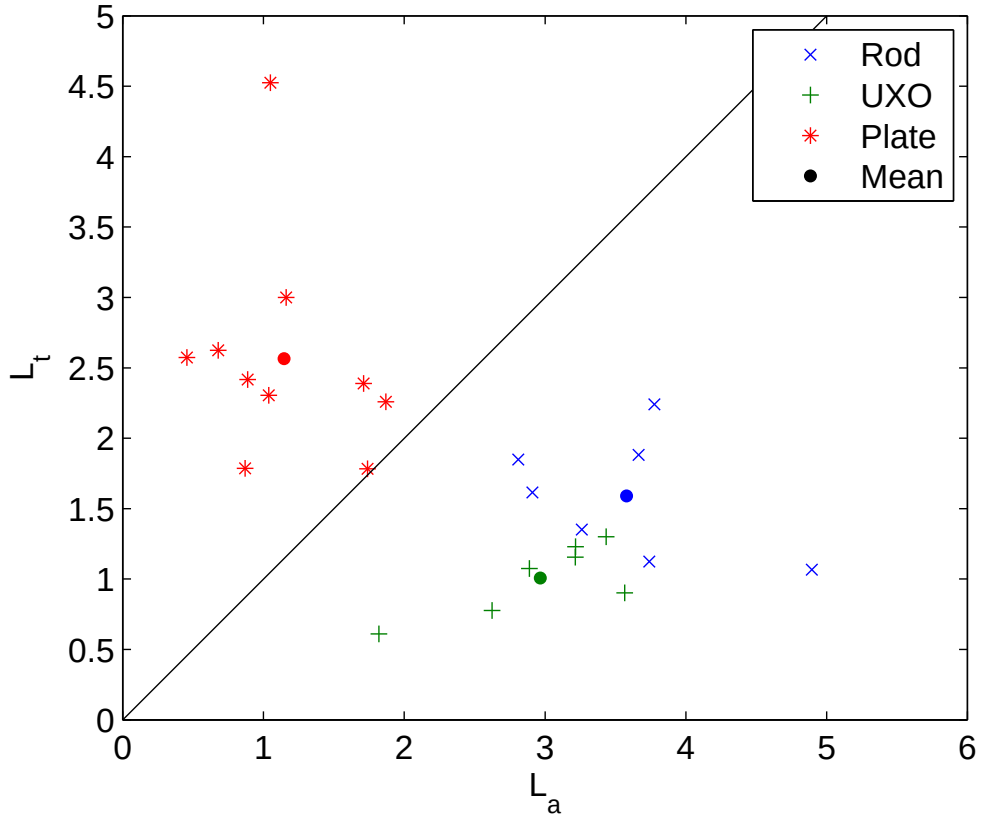

Figure 2.8: Dipole parameters

These dipole response parameters were extracted from real data. The mean of each cluster was chosen as the best guess for the object's true parameter set. The top left "" cluster is from plate data sets, the "x" cluster on the right is from rod data sets, and the "+" cluster on the bottom is from* UXO *data sets. The line down the middle indicates when the axial response is equivalent to the transverse response. This situation occurs when the target is a sphere.*

Table 2.1: Library of equivalent dipole polarizability rates

Object	$L_a[\frac{Am^2}{Ts}]$	$L_t[\frac{Am^2}{Ts}]$
Rod	3.58	1.59
UXO	2.97	1.0
Plate	1.15	2.57

$$
\begin{aligned}
\underset{x_{\text{UXO}}}{\text{minimize}} \quad & \frac{1}{M-n-1}\sum_{m}\left(\frac{z_m-\hat{z_m}}{\sigma_{z,m}}\right)^2 \\
\text{subject to} \quad & \hat{z_m} = h(x_{\text{UXO}},\theta_{\text{EMI},m}),\ m=1,\ldots,M \\
& \begin{bmatrix} -2 \\ -2 \\ 0 \\ 0 \\ 0 \\ 0 \\ 0 \end{bmatrix}_{n\times 1} \leq x_{\text{UXO}} \leq \begin{bmatrix} 2 \\ 2 \\ 2 \\ 2\pi \\ 2\pi \\ 100 \\ 100 \end{bmatrix}_{n\times 1}
\end{aligned}
\tag{2.9}
$$

The constraints were based on physical limitations of the real world where the UXO is close to the sensor and underground which is modeled as a rectangular prism of dimensions $4m \times 4m \times 2m$. The z-axis is positive when pointed into the ground. The L_a and L_t are defined as positive and constrained to be less than 100 based on observations of the data. Figure 2.8 shows the extracted dipole response parameters for each of the data sets taken. The resulting dipole parameters are clustered in groups with the same target. The mean of each cluster is used as the best guess at the object's parameters and are written in Table 2.1.

Ideally, each set of data for a target would result in identical polarization parameters. Position uncertainty of the sensor is one possible source for the spread. The data was taken at $16Hz$ as the sensor was pushed along lines. The sensor position was estimated assuming the lines were spaced perfectly while the sensor is being pushed in a straight line at a constant velocity.

Figure 2.9 uses simulations to show the effect of 2D sensor position noise on parameter extraction. These simulations use the response parameters in Table 2.1 to model three targets. In each run, one of the objects is assumed to be buried in the center of the search area. A sensor is moved in lines above the target to simulate the way real measurements were taken previously. In each run, various levels of noise were added to the sensor positions simulating an inaccurate positioning sensor. The standard deviation of the noise is labeled for each of the plots. On top of that noise, measurement noise was also added to the sensor readings. Finally, each data set was then run through Equation 2.9 to extract the dipole parameters which are then plotted in Figure 2.9. As the position uncertainty increases, the resulting dipole response parameters also spread.

2.2.3 Discrimination

UXO discrimination can be done by comparing the actual measurements with the predicted measurements. A true likelihood cannot be calculated without known prior probabilities. In this thesis, discrimination will be done again using goodness of fit. The predicted measurements will be based on the objects in the library. The actual goodness of fit optimization is rewritten in Equation 2.10.

$$
\begin{aligned}
\underset{l,x_{\text{UXO}}}{\text{minimize}} \quad & c_l = \frac{1}{M-n-1}\sum_m \left(\frac{z_m - \hat{z_m}}{\sigma_{z,m}}\right)^2 \\
\text{subject to} \quad & \hat{z_m} = h(x_{\text{UXO}}, \theta_{\text{EMI},m}),\ m = 1,\ldots,M \\
& \begin{bmatrix} -2 \\ -2 \\ 0 \\ 0 \\ 0 \end{bmatrix}_{5\times1} \leq x_{\text{UXO}} \leq \begin{bmatrix} 2 \\ 2 \\ 2 \\ 2\pi \\ 2\pi \end{bmatrix}_{5\times1} \\
& \begin{bmatrix} L_{a,l} \\ L_{t,l} \end{bmatrix}, l = 1,\ldots,L
\end{aligned}
\tag{2.10}
$$

There is a subtle difference between estimating all seven x_{UXO} parameters, what was

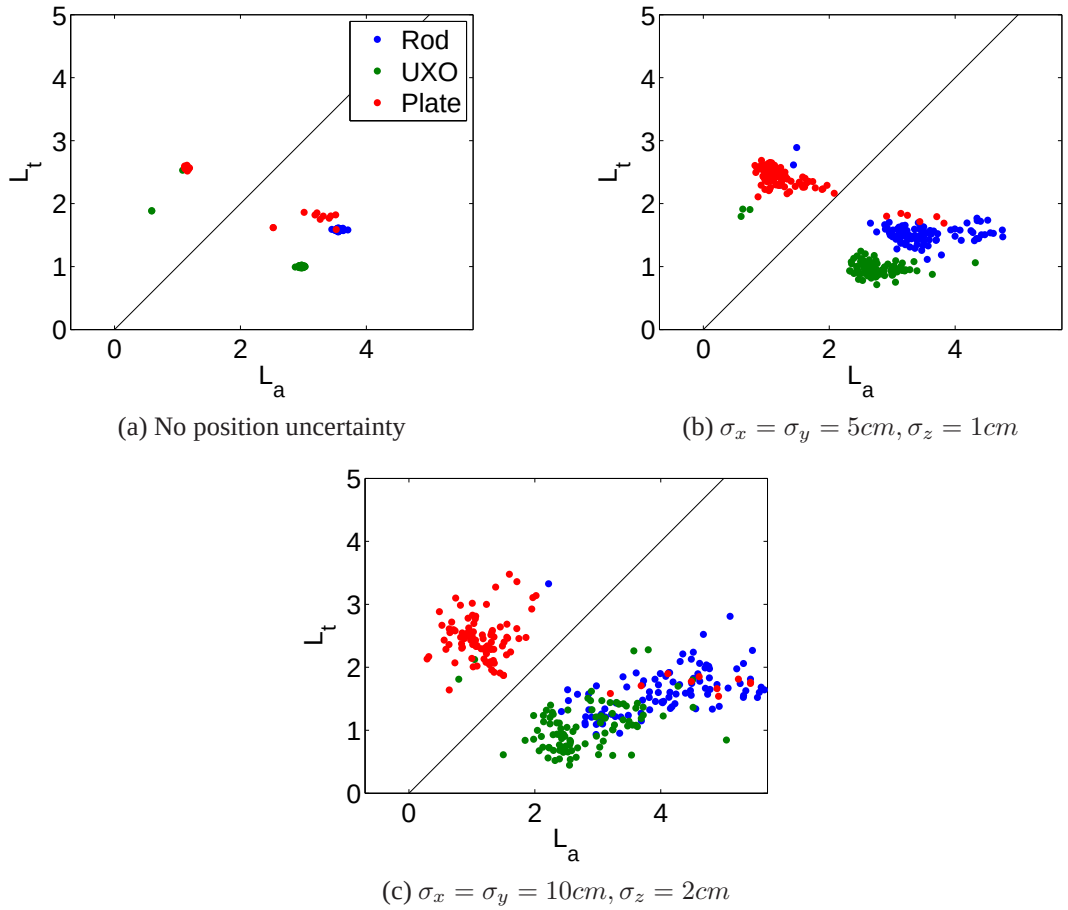

(a) No position uncertainty

(b) $\sigma_x = \sigma_y = 5cm, \sigma_z = 1cm$

(c) $\sigma_x = \sigma_y = 10cm, \sigma_z = 2cm$

Figure 2.9: Parameter estimation in the presence of sensor position uncertainty

Simulated data was generated using the target library. The sensor position was shifted with random noise before estimating the dipole response parameters. As the position uncertainty increases, the spread of the dipole response parameters also increases.

done in the previous section, and using the target library to help discriminate. In the latter situation, the dipole response parameters are known, so x_{UXO} only contains the location and orientation of the target. The L targets in the library are each tried during the minimization process.

$$x_{\text{UXO}} = \begin{bmatrix} \vec{r} \\ \theta \\ \phi \end{bmatrix}_{5\times 1} \tag{2.11}$$

Figure 2.10a shows measurements from each line during one real data run with an UXO as the target. Figure 2.10b focuses on the sixth line from the right. Assuming the target was a rod, the blue line shows the predicted measurements that best fit the real measurements. The red line corresponds with the best fitting plate parameters. The green line follows the best fitting UXO parameters. For a library of these targets, the UXO model would fit the data best and have the lowest goodness of fit.

This chapter explains why and how the EMI sensor is used in this thesis. It also uses the Geonics EM61-MK2 to show UXO discrimination by extracting the dipole response parameters from real measurements. In the following chapters, different strategies to determine where to move and orient the sensor are presented which improve the information contained in the measurements used by this discrimination algorithm.

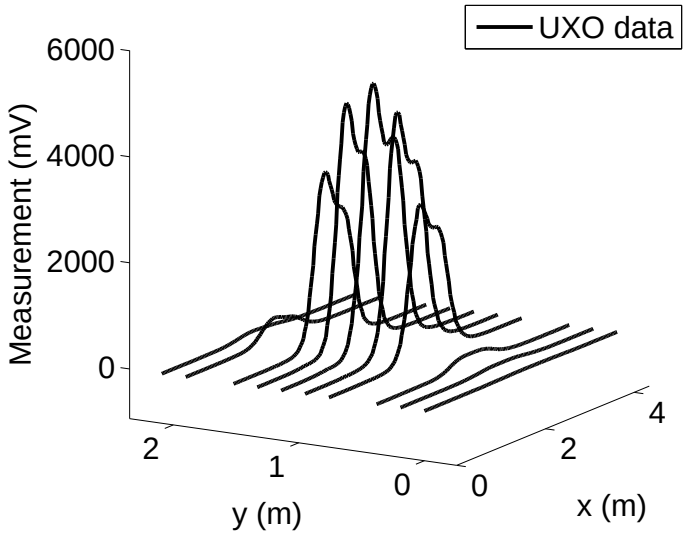

(a) Real UXO data

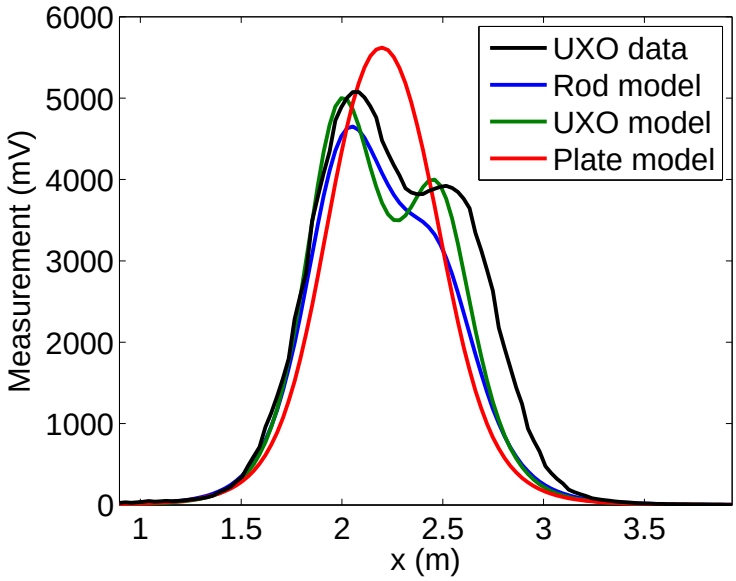

(b) One line of data

Figure 2.10: The discrimination process

(a) A 3D plot showing the measurements from real field data of an UXO. (b) The data from the sixth line is shown along with predicted sensor measurements from each x_{UXO} option. The UXO model produced the measurements that best fit the data from all the lines.

Chapter 3

Local Search

THIS CHAPTER shows how to improve discrimination using a non-adaptive focused search. Traditionally, a field wide GPS based search is used to find unexploded ordnances, UXOs. Focusing the search on a suspected UXO location and using an odometry positioning system in a lawnmower pattern is shown to improve discrimination when assuming a $5cm$ error in GPS positioning and a 5% distance traveled error in odometry. These numbers are explained in Section 3.1.1.

3.1 Odometry vs. GPS

Section 2.2.3 discusses the affect sensor position accuracy has on estimating an UXO's parameters. Traditionally, sensor measurements are geotagged with GPS measurements of the vehicle's location. In a large scale traverse, GPS is the preferred option because the error from location to location can be assumed to be uncorrelated and bounded. The error is modeled by the true position corrupted by Gaussian noise with a known standard deviation. Another option for geotagging measurements is using an odometry based system. This system would use odometry sensors to report the distance traveled from the last measurement and a compass to measure the heading of the vehicle. Unfortunately, this setup would have an unbounded error relative to any absolute frame of reference. The actual error is modeled as an error in the relative position from the current position to the previous position. The error distribution is Gaussian with a standard deviation as a percentage of the distance

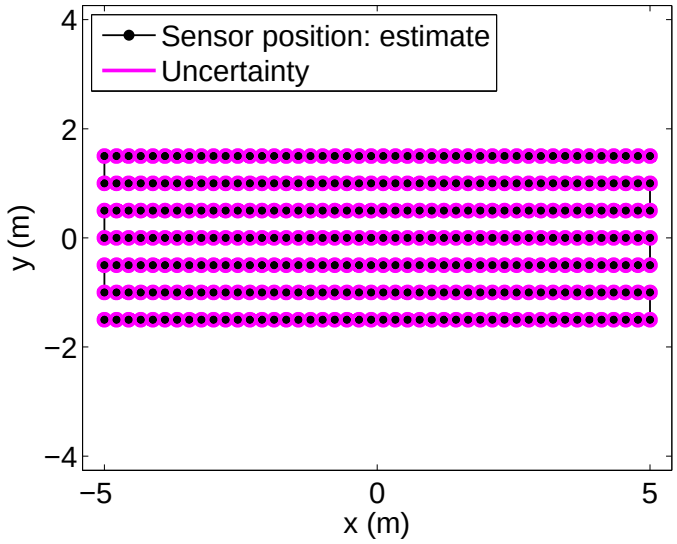

(a) GPS error

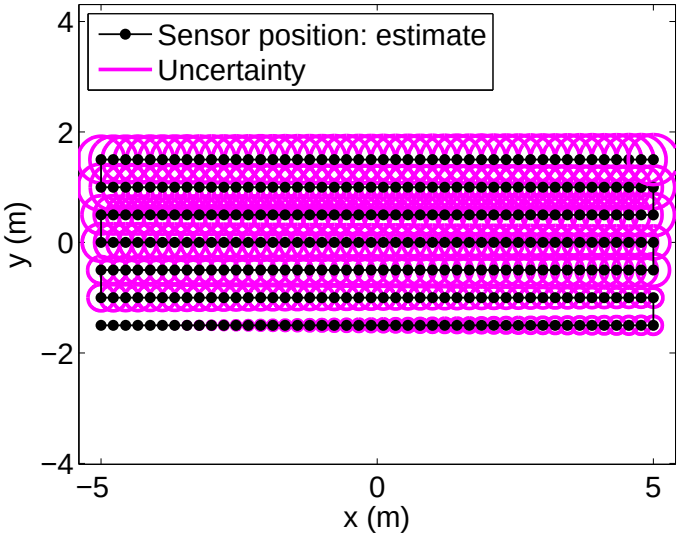

(b) Odometry error

Figure 3.1: Comparison of position error propagation in a field wide traverse

Two types of positioning systems are compared for a traverse over roughly $75m$. The start location of the lawnmower traverse is the bottom left hand side of the plots. The GPS*'s positioning error does not change from measurement to measurement. The odometry based system's error increases the further the vehicle moves.*

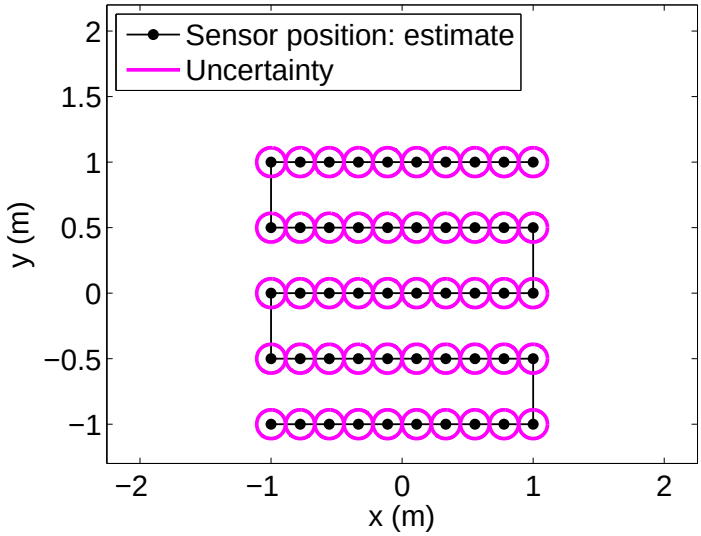

(a) GPS error

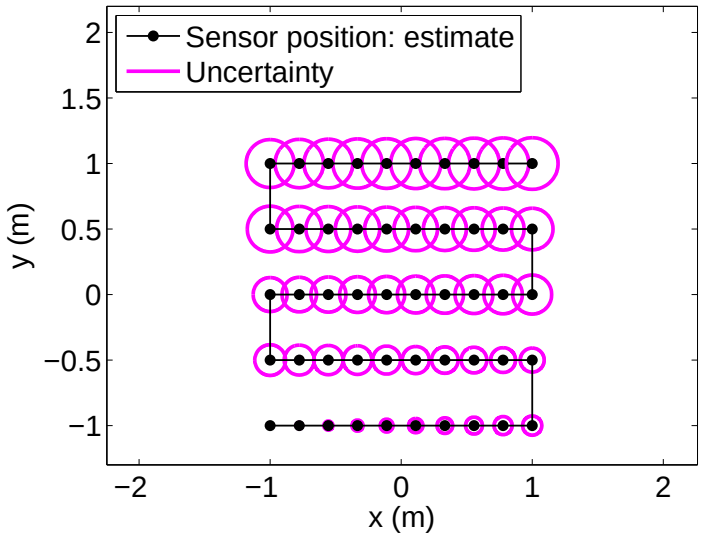

(b) Odometry error

Figure 3.2: Comparison of position error propagation in a small scale traverse

The positioning systems are now used for short lawnmower searches that traverse 14m. There is no affect on GPS *induced errors because they are independent of the distance traveled. The final odometry induced error is reduced because the traverse has been significantly shortened.*

traveled. Figure 3.1 shows a sensor traveling $75m$ in a lawnmower pattern. A position error ellipse is drawn around the estimated location of where each sensor measurement was taken. The error ellipse in the GPS case maintains its size, but in the odometry case continuously increases. By the third line, the uncertainty ellipse encompasses the previous and next estimated location of the vehicle. Further along, the ellipse begins to include other lines. These errors can have a large impact when trying to incorporate measurements for discrimination.

For the reinvestigation scenario, a sensor sweep is performed again over a specific location where an UXO is believed to be buried. The original investigation can be a previous search and post processing iteration or it can be a field wide traverse with a sensor reporting that an object is nearby. A $2m \times 2m$ lawnmower pattern centered at the suspected target location is used for the focused search. The small size was chosen because the signal strength decays at $\frac{1}{|\vec{r}|^6}$. Section 3.1.2 explains why a lawnmower pattern was picked after examining other trajectories. Figure 3.2 shows these simulated lawnmower traverses. The smaller trajectory has no effect on the GPS error ellipses, but it does reduce the final position uncertainty for the odometry case. Despite that, the position uncertainty at the end of the traverse is still greater than the GPS case.

3.1.1 Absolute Error vs. Relative Error

Section 2.1 states that relative sensor positions and orientations are used for parameter estimation. The important word here is relative as opposed to absolute. Imagine a situation where every measurement in a pattern is shifted $1m$ north. The measurements would still match an UXO model quite well, however the estimated location of the UXO would be wrong, also shifted north by $1m$. An odometry based system is ideally suited for getting relative information for a small scale traverse.

Figure 3.3 shows a single simulated traverse with a GPS and an odometry error. Both the true location and the estimated location of the sensor are plotted. The estimated location follows the desired lawnmower pattern exactly. A discrimination algorithm would assume that each sensor measurement was taken exactly at the estimated location. Figure 3.4 stacks 200 simulated traverse on top of each other. The absolute positioning error is defined as

the distance each true sensor location is from its predicted location along the lawnmower pattern. These runs assume the sensor platform has perfect control and can go to any destination with no error. Therefore, the error in the plots are entirely due to sensor error.

Figure 3.5 shows a shifted and rotated lawnmower pattern that does a better job matching with the true locations than the original estimated locations did. This indicates that the relative positioning error is less than the absolute positioning error. The new trajectory is labeled as an estimate in a local frame because Figure 3.6 aligns 200 simulated traverses through each respective local frame.

For the GPS situation, there is little movement for the new trajectory. The position noise from each measurement is uncorrelated and so the best fit is nearly identical as the predicted trajectory. The GPS case for both Figures 3.4 and 3.6 have similarly sized clusters of true locations surrounding the estimated location. This indicates that the relative position error is very similar to the absolute position error.

In the odometry situation, there is a shift in the new relative trajectory indicating the relative error is reduced from the absolute error. The cluster of true locations for this situation also shrinks from Figure 3.4 to Figure 3.6. This results from the relative nature of the odometry sensor and the trajectory. The trajectory impact will be discussed in the next section.

Taking a closer look at the positioning errors, Figure 3.7a plots the average error per sensor measurement. The first ten sensor positions correspond with the bottom line of the trajectory. For GPS the absolute and relative error stays constant throughout the traverse because the noise is assumed to be uncorrelated. For odometry, the absolute error increases the further the sensor moves. The overall average absolute error is actually higher for the odometry case when compared to the GPS case. However, the average relative error is reduced below the GPS line with a large improvement at the center of the pattern. This also happens to be where the sensor return is strongest because the sensor is close to the target.

Figure 3.7b compares the impact of various odometry errors in terms of percent traveled vs. a $5cm$ GPS error [67]. The $5cm$ error corresponds with about a 7% distance traveled odometry error. In papers by Olson and Matthies, odometry error rates were less than 5% [60, 71]. This thesis will assume a 5% distance traveled error for an odometry system.

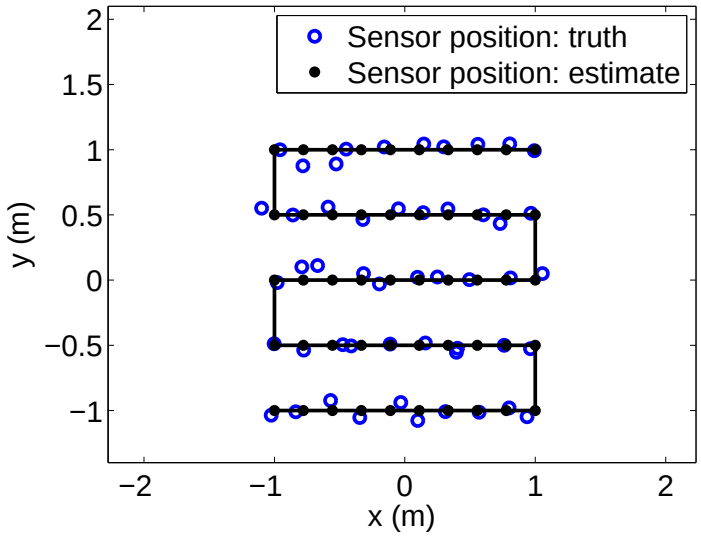

(a) GPS error

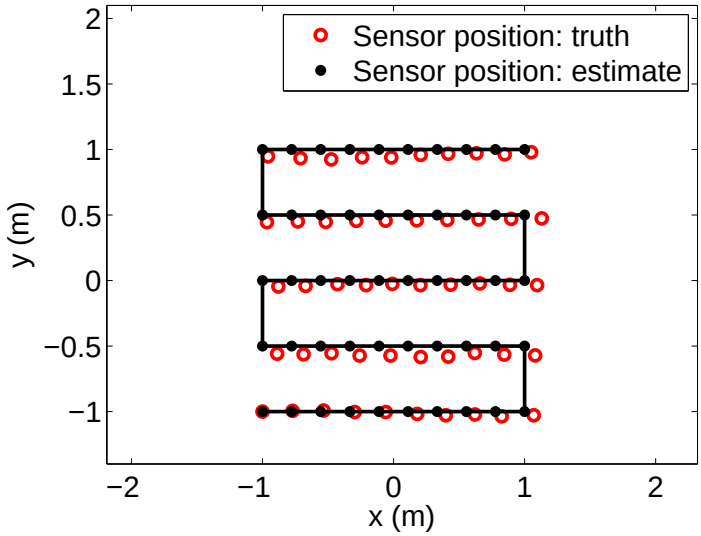

(b) Odometry error

Figure 3.3: Single simulated traverse

A single traverse is shown here. The black line shows the intended route of the sensor while the circle markers show the true location of the vehicle.

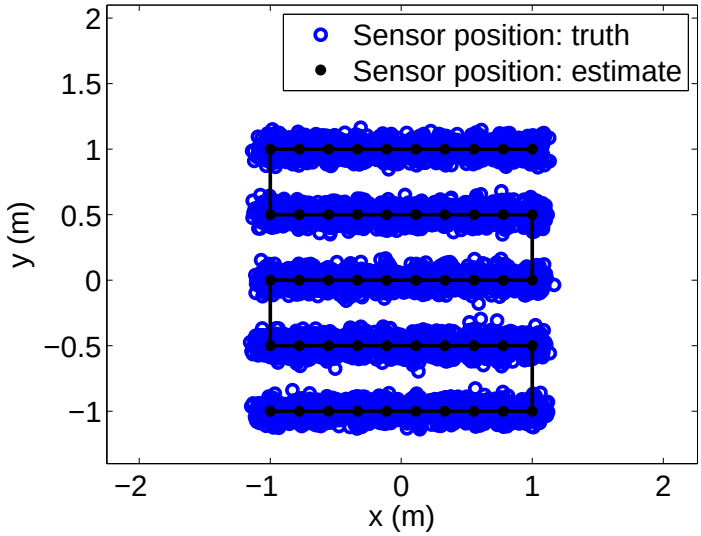

(a) GPS error

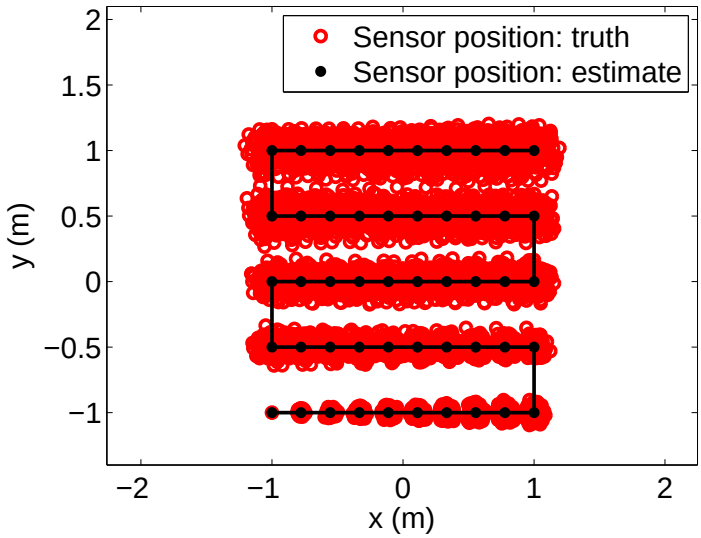

(b) Odometry error

Figure 3.4: Multiple simulated traverses aligned to a world frame

Two hundred traverses are displayed for each sensor type. The spread of the true locations mimic the uncertainty ellipses shown in Figure 3.2.

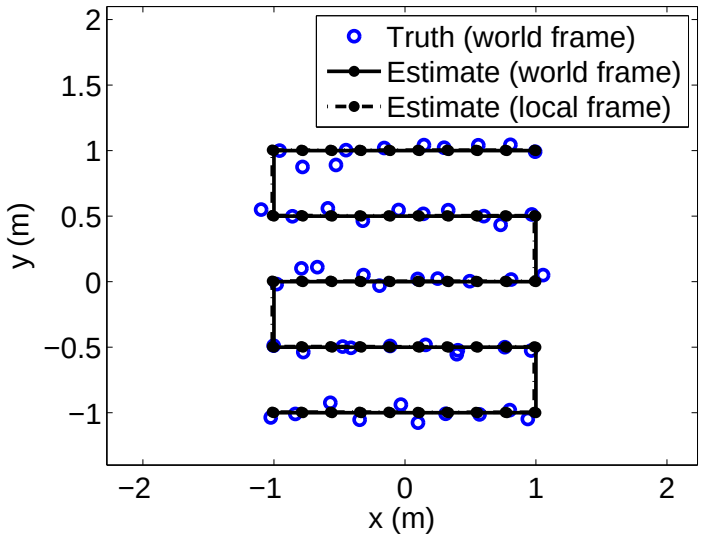

(a) GPS error

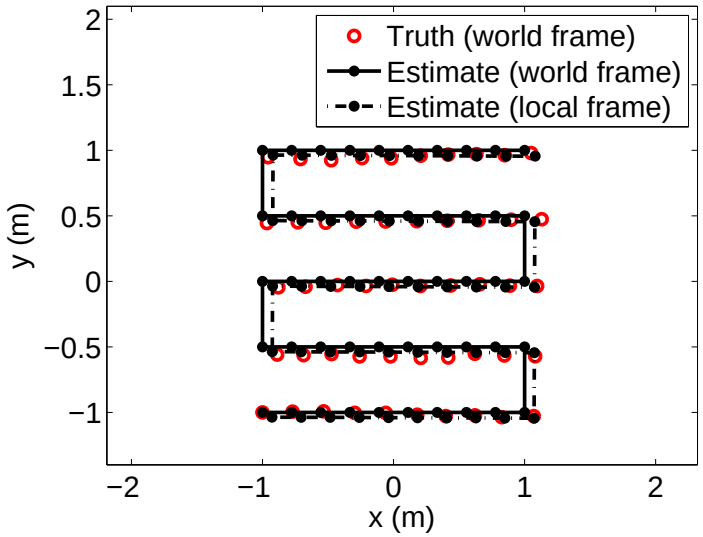

(b) Odometry error

Figure 3.5: Relative trajectory

The same traverse from Figure 3.3 is shown here. This time, a shifted and rotated lawnmower pattern is fit to the true locations. There is little movement in the new pattern for the GPS *traverse. The odometry traverse shows more movement in the new pattern indicating that the relative error is less than the absolute error.*

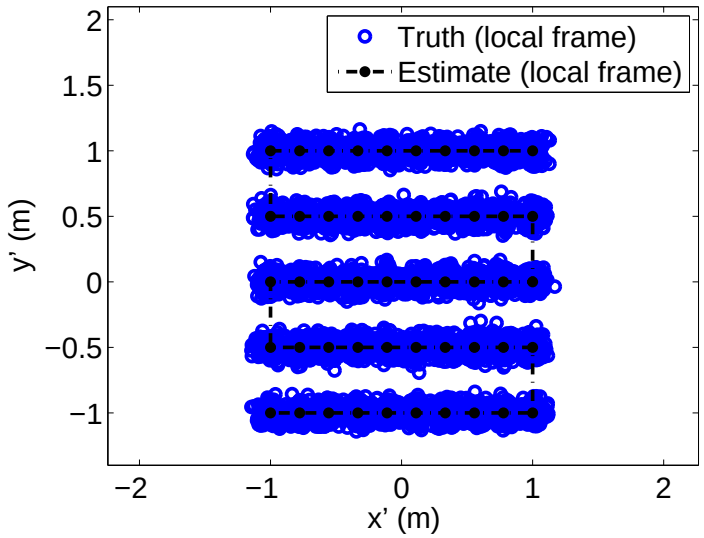

(a) GPS error

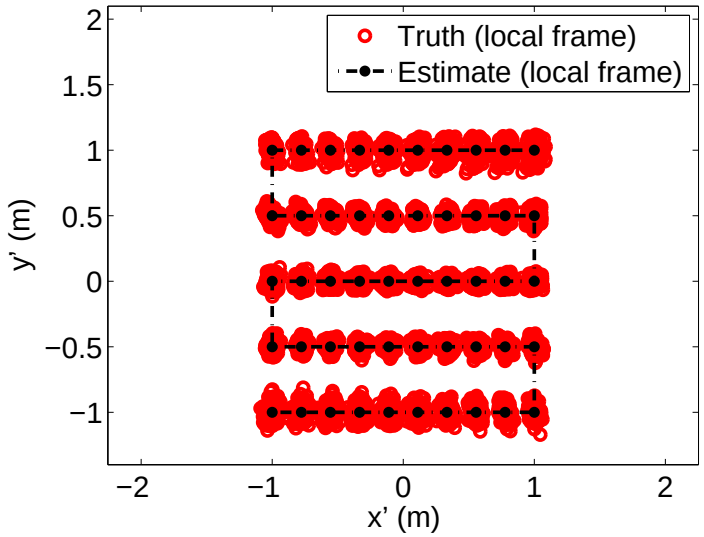

(b) Odometry error

Figure 3.6: Multiple simulated traverses aligned by relative trajectory

New shifted and rotated patterns are found for each of the simulated sensor runs used in Figure 3.4. The are stacked and aligned by the new trajectory. There is a decrease in the spread of sensor positions for the odometry setup, but not for the GPS *case. Note that the best relative odometry error measurements occur at the center of the lawnmower pattern where the measurements are likely to be the strongest.*

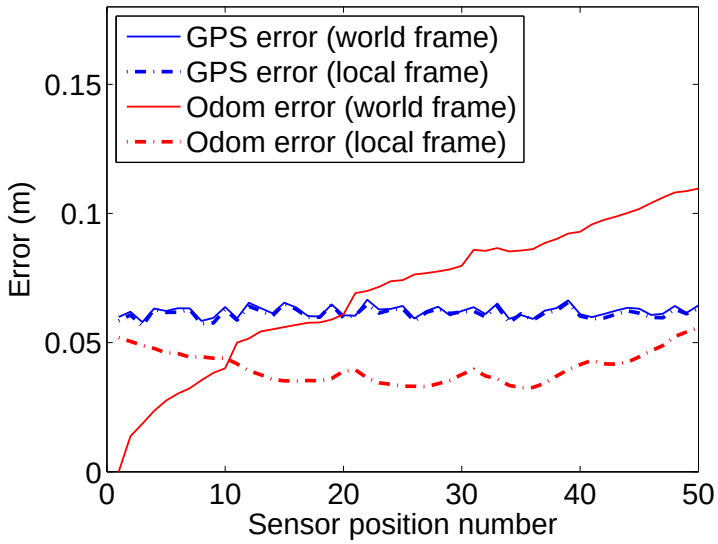

(a) Sensor position error

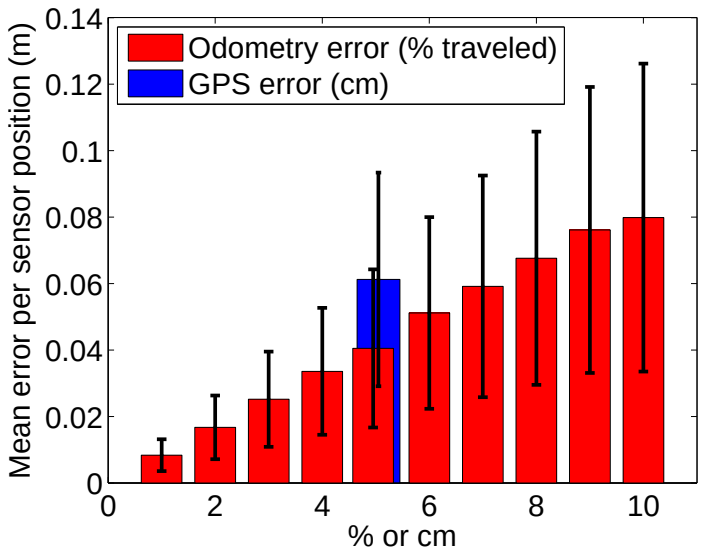

(b) GPS vs. Odometry

Figure 3.7: GPS vs. odometry comparison for small scale lawnmower trajectory

(a) The average relative and absolute error per sensor location is shown for both the GPS *setup and the odometry setup. (b) The mean relative error over an entire traverse is shown for a* $5cm$ GPS *error and several levels of odometry error. The* GPS *error compares with an odometry error of 7% over the distance traveled.*

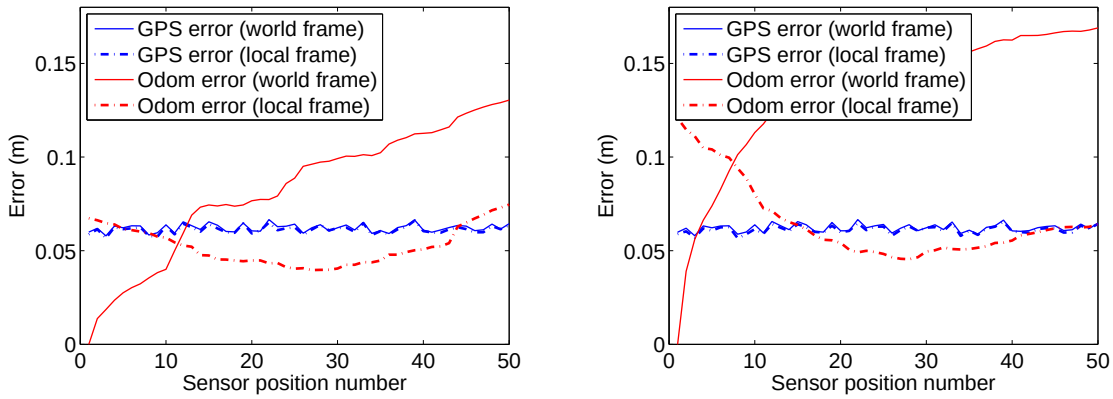

(a) Rectangular spiral (b) Circular spiral

Figure 3.8: Alternative trajectories: Relative vs. absolute position error

This figure shows the average relative and absolute sensor position errors for the two new traverses. The error in the GPS *case is the same as the lawnmower pattern shown in Figure 3.7a. The relative odometry error for these trajectories do not perform as well as the lawnmower pattern.*

3.1.2 Alternate Trajectories

Two other trajectories were also studied. The first one places the sensors at the same locations as the lawnmower pattern, but uses a pattern that spirals inwards. The second one rounds the edges of the box shape and makes the spiraling more circular. These trajectory change have minimal impact on the GPS sensor, but do affect the odometry error. Figures 3.9 shows the stacked sensor positions aligned by the absolute trajectory and then the best relative trajectory.

Figures 3.8 plots the average absolute and relative position error per sensor measurement for the alternate trajectories. The GPS induced positioning error is the same between all three trajectories because the error is independent of the trajectory taken. The odometry errors do not show the same improvement as seen in the lawnmower patterns.

This is not an exhaustive search on all possible trajectories, but it does indicate that the lawnmower pattern is a good choice. It has improved relative position accuracy because it loops back and does not enclose other lines. An interesting direction for future work would be to explore other trajectories that explicitly account for the relative accuracy of each measurement.

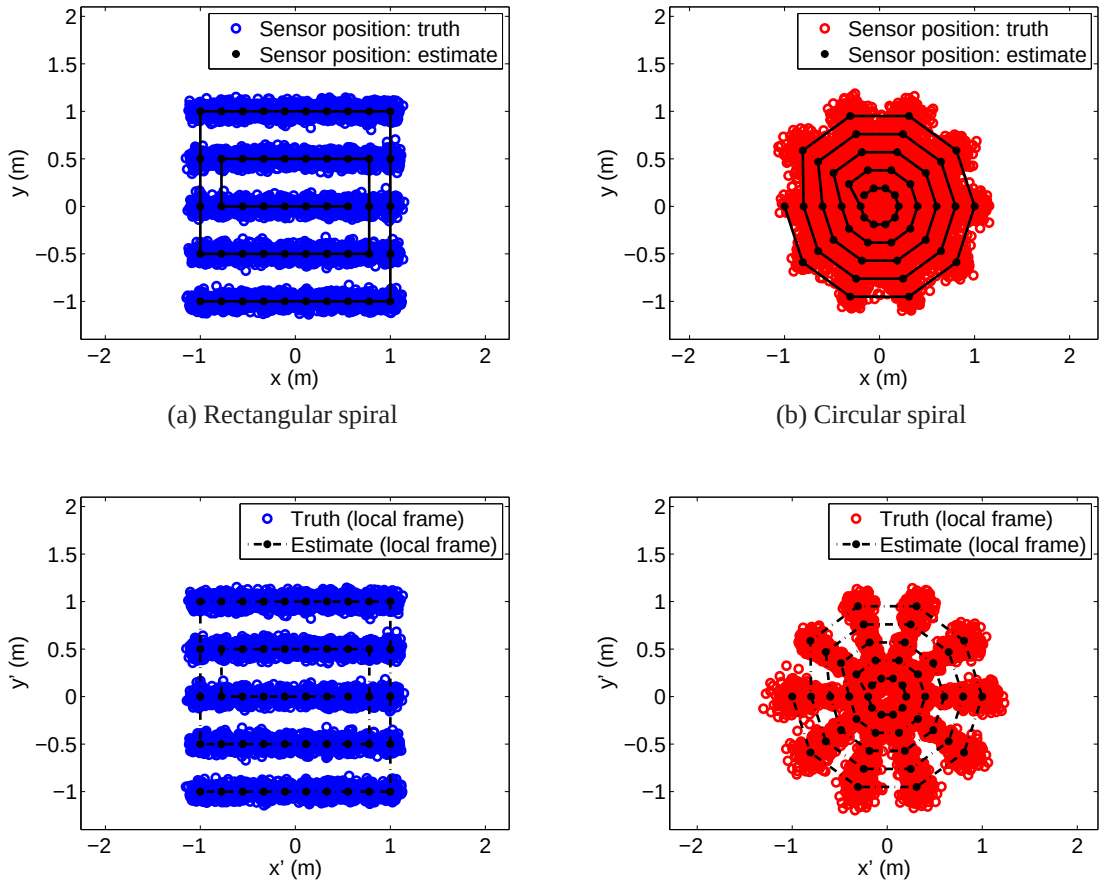

(a) Rectangular spiral

(b) Circular spiral

(c) Rectangular spiral

(d) Circular spiral

Figure 3.9: Alternate trajectories

Two additional trajectories were explored along with the lawnmower pattern. The rectangular spiral starts on the bottom left hand side of the plot and then traverses in a counter-clockwise direction as it spirals inwards. The circular spiral starts on the left hand side of the plot and then spirals inwards in the counter-clockwise direction. The top row have simulations that are stacked by the world fixed coordinate frame. The bottom row have simulations that are stacked by a local coordinate frame fixed to the best fit relative trajectory.

3.2 Simulations

3.2.1 UXO Discrimination

Several hundred runs were simulated to show how relative sensor positioning affects discrimination. In each run, there is a single target in the ground that was taken from the target library developed in Section 2.2.2. The vehicle does a focused search with an orientation fixed sensor performing a $2m \times 2m$ lawnmower pattern above the estimated UXO location. Measurement noise amounting to 5% of the signal value with a minimum noise setting is included in each sensor reading [75]. The noise in sensor position is the aforementioned 5% distance traveled error for odometry and $5cm$ error for GPS. The target's location and orientation is randomly changed for each run so the algorithm does not know the object's true location, orientation, or type.

The goodness of fit histograms in Figure 3.10 summarize the results from the simulations. For each run, a goodness of fit was calculated assuming the target was each of the objects in the target library. The histogram's bins are based on those goodness of fit values. Figure 3.10c shows 200 simulated runs where the object buried is actually an UXO and the positioning system is GPS. In ideal circumstances, the UXO fit would have a minimal goodness of fit value and the fits from the rod and plate would have a large goodness of fit value. This plot indicates the sensor data fits the UXO model better than the rod and plate model. Figure 3.10d performs the same set of simulations, but with an odometry based positioning system. The UXO model's fit for the odometry scenario is better than the GPS scenario. The rod model's fit also improves significantly. Because the rod and UXO are very similarly shaped, the algorithm has a difficult time differentiating between the two. The plate fit is improved also, but is noticeably weaker than the other two objects. This trend highlights the improvement when using odometry as opposed to GPS. The reduction in relative sensor positioning error has had a significant impact on how well the sensor models are fitted to the data. The same trends are seen in the first row where the object is a rod and in the last row where the object is a plate.

A receiver operating curve, ROC, shows how these histograms affect discrimination. A UXO technician can look at a data set and dig up anything that has a goodness of fit for an UXO model less than 5. Keep in mind that the actual buried object is unknown, so the

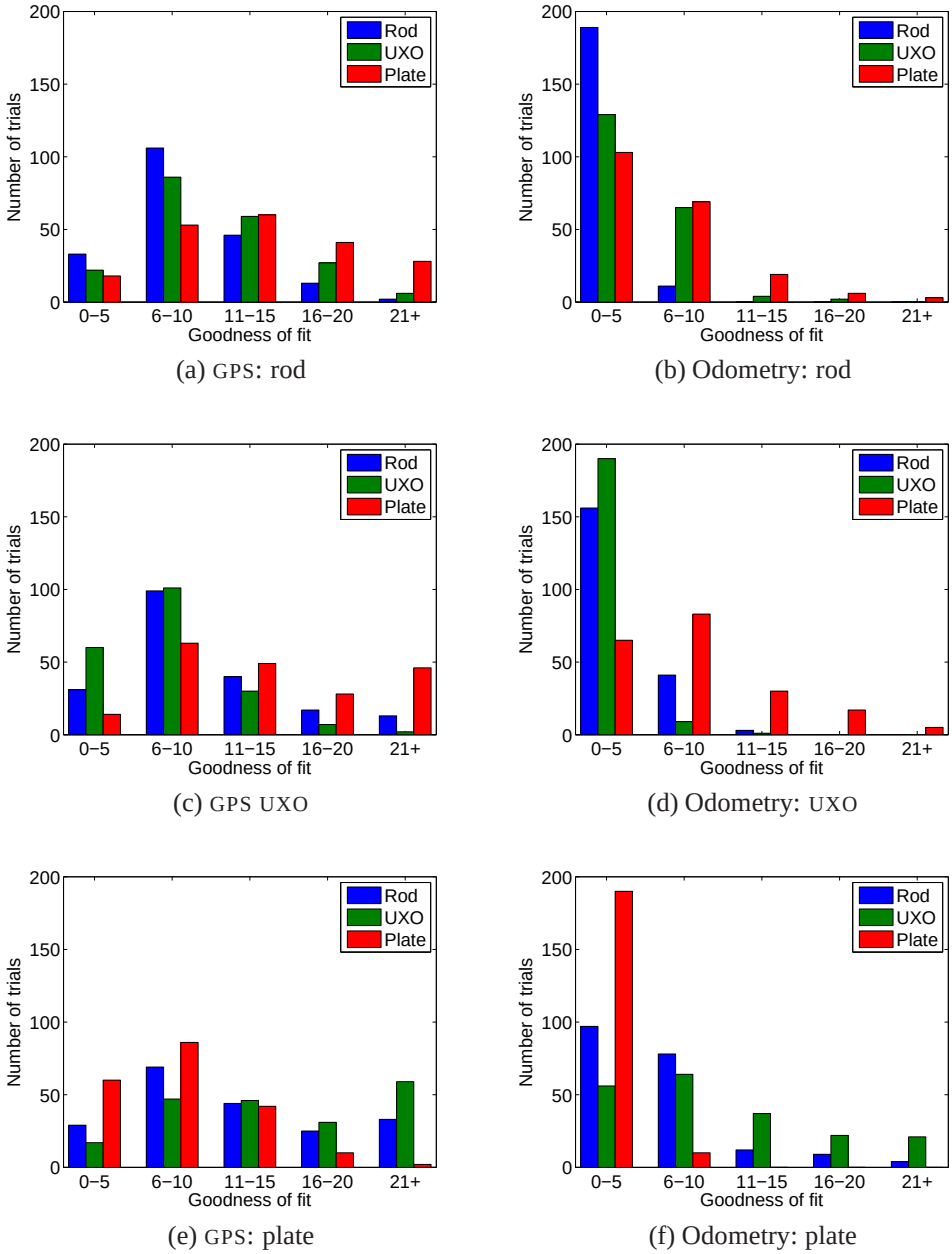

(a) GPS: rod (b) Odometry: rod

(c) GPS UXO (d) Odometry: UXO

(e) GPS: plate (f) Odometry: plate

Figure 3.10: Goodness of fit histograms

Each figure represents 200 simulated runs with sensor noise and position noise. Each row consolidates runs where the buried objects are identical. The left column shows runs using GPS *to determine position and the right column uses odometry. The plots indicate a* GPS *error increases the model fit error more than the odometry error.*

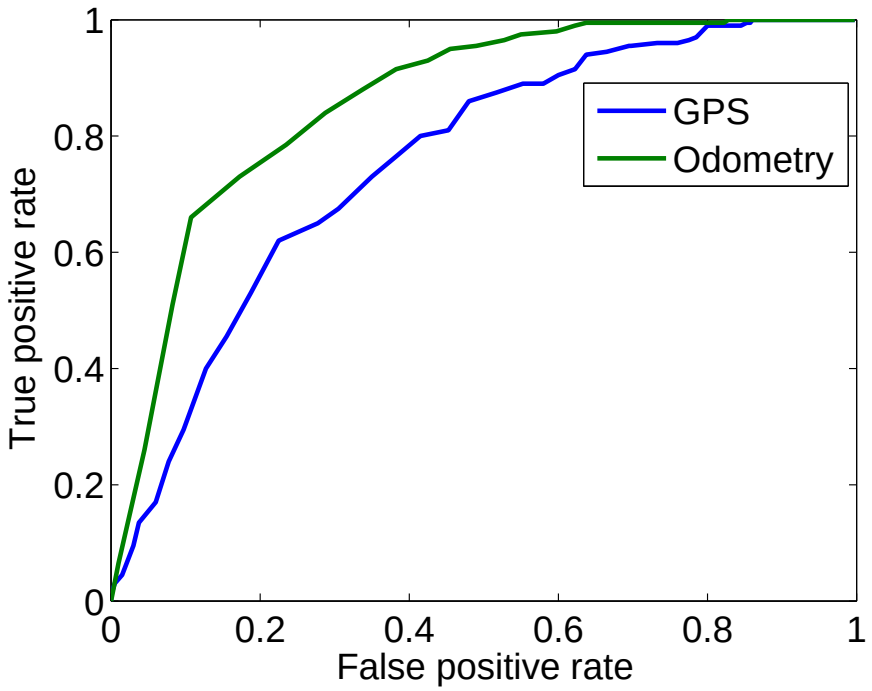

Figure 3.11: Receiver operating curve

*The x-axis shows the percentage of non-*UXO *targets declared as* UXO*. The y-axis shows the percentage of* UXO *targets declared as* UXO*. The desired movement of the line is to push it into the top left hand corner. This represents digging every* UXO *item up and leaving every non-*UXO *object in the ground.*

technician may ignore the other fits and just consider the UXO fit. These simulations for each positioning sensor type has 200 UXOs, 200 rods, and 200 plates. If the GPS data set is used, 60 UXOs will be uncovered, true positives, along with 22 rods and 17 plates, false positives. With odometry, 190 UXOs will be uncovered along with 129 rods and 56 plates. By changing the fit threshold, the false positive rate and true positive rate also changes forming a ROC that is plotted in Figure 3.11. The missed detection rate can also be seen in the figure because it is the difference between one and the true positive rate.

3.2.2 Perfect Knowledge: Sensor vs. UXO Position

In the previous simulations, the trade space was which positioning sensor should be used. This section looks at which uncertainties affect the discrimination the most: uncertainty in the target position or uncertainty in the sensor locations.

Figures 3.12a and 3.12b are goodness of fit histograms of 200 runs with a buried UXO. One assumes perfect knowledge in target position and the other assumes perfect knowledge in the sensor position. In both cases, there is a clear improvement on differentiating the plate from the other two axially symmetric objects. Figure 3.12c plots a ROC generated with a combination of the above two data set and other runs where the object buried is a plate and a rod.

With perfect sensor positioning knowledge, the true target location and orientation is normally distributed around the initial prediction. The overall UXO goodness of fit improves because there is less error on estimates of distance between the sensor and target thereby reducing overall measurement noise.

In the situation with perfect knowledge about the target's location, the orientation is still assumed to be unknown. GPS is used for positioning so the world frame is used for both target and sensor position. This also produces a good divergence between the UXO fit and the other model fits.

This analysis reinforces two lines of research that can improve UXO discrimination. The first is improving the relative accuracy in the sensor positioning system over the search region. The second is improving the knowledge of the target's location. A potential strategy is to incorporate MAGs and GPRs to accomplish this [85, 107, 108].

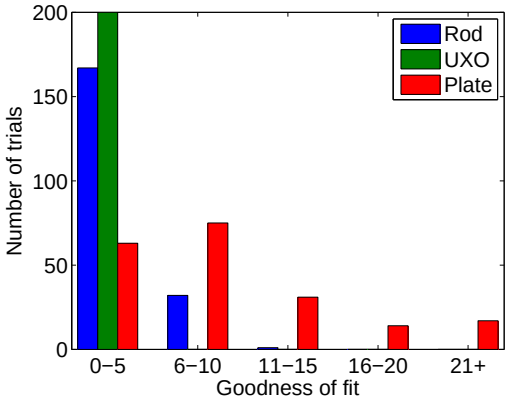

(a) Known sensor location

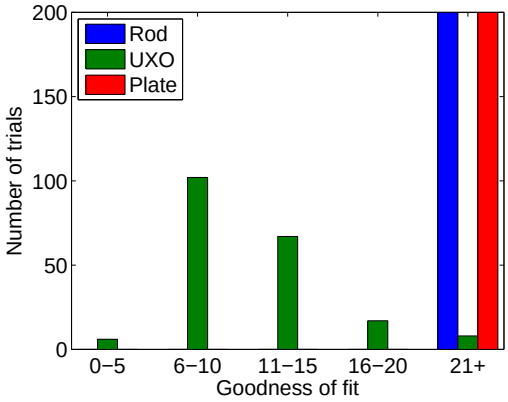

(b) Known target location

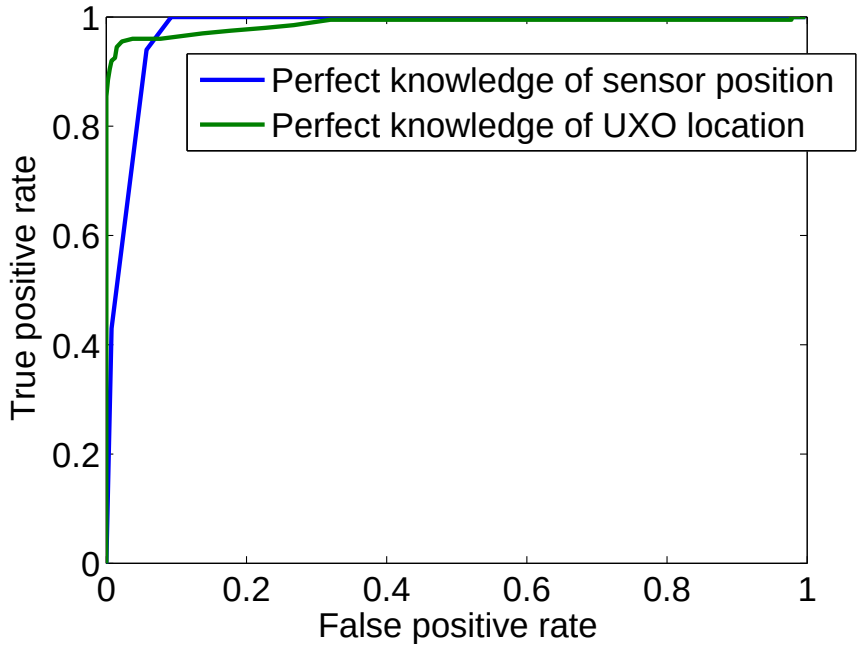

(c) ROC

Figure 3.12: Comparison between knowing the location of the sensor vs. the target

The top row, (a) and (b), shows histograms of 200 runs with a buried UXO. *When the sensor locations are known perfectly, the target location is normally distributed around the initial estimate. In the second situation where the target location is known perfectly, the sensor position is normally distributed around its goal location. In both cases, the additional knowledge assists in discrimination, but it affects the goodness of fit in different ways. (c) This* ROC *incorporates the* UXO *histograms with similar runs over buried plates and rods.*

Chapter 4

Adaptive Sensing

PREVIOUSLY, a sensor equipped vehicle was moved in a predetermined trajectory over a suspected target. Adaptive sensing improves discrimination by using the most recent measurements to optimize the trajectory. This chapter shows why the determinant of the predicted uncertainty is used to quantify the effectiveness of a trajectory, why the eigenvector form of the sigma-point Kalman filter, eSPKF , is ideally suited to estimate that uncertainty, and how to optimize a trajectory.

Figure 4.1 shows two high level block diagrams on how the algorithm adapts a trajectory to maximize the information gathered about a suspected target. Adaptive sensing has three main steps. Given some initial estimate of the unexploded ordnance's, UXO's, state and uncertainty, x_{UXO} and $\Sigma_{x_{\text{UXO}}}$, the trajectory generation block outputs a trajectory that attempts to maximize the information gathered. The sensor is moved and reoriented to achieve the desired state and then a measurement is taken. The estimator block takes both the measurement and the sensor state and updates the estimate of the target's parameters and uncertainty.

The trajectory generation block has been expanded in the same figure. A predicted sensor measurement, z', is calculated from the sensor model using the current target estimate and a given trajectory, Θ_M. An estimator then updates the estimates based on the predicted measurement. This is a recursive process that repeats until the entire trajectory has been completed. A cost function converts the estimate uncertainty into a scalar cost value, J. Finally, a minimization algorithm is run to find a trajectory that minimizes the cost.

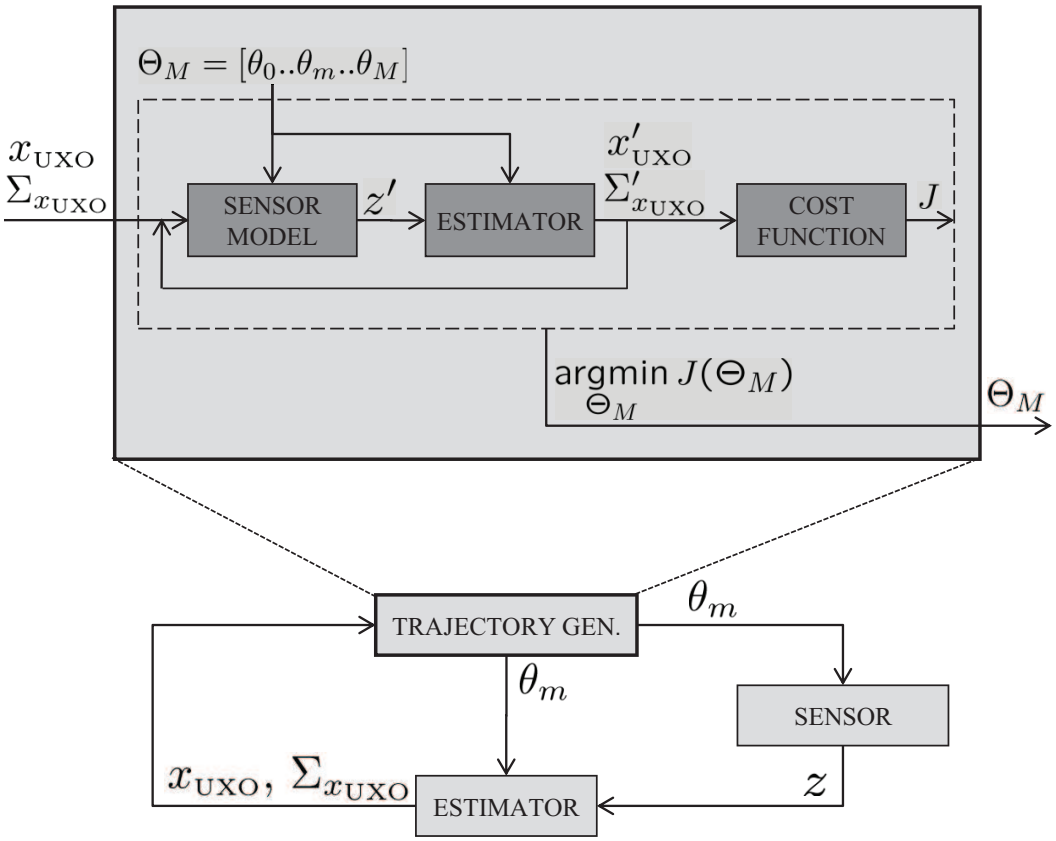

Figure 4.1: Adaptive sensing block diagram

The bottom block diagram represents the adaptive sensing algorithm. It adjusts the trajectory to maximize the amount of information gathered by the sensor. The top block diagram depicts the inner blocks of the trajectory generation block.

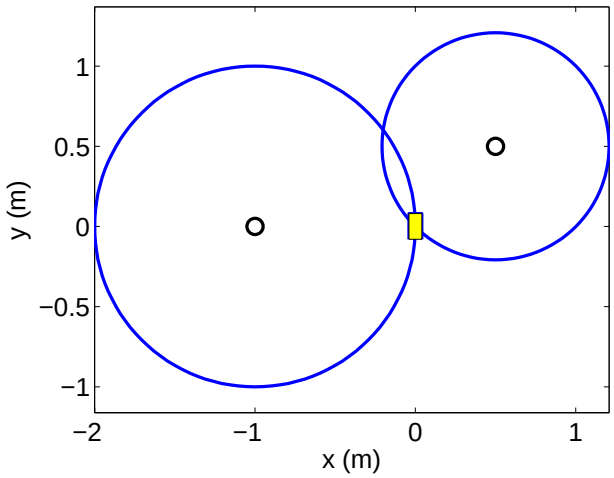

Figure 4.2: Range sensor contour

This shows two 2D range sensor contours. The blue circle represents target locations where the sensor, centered within the contour, would return the same measurement.

The rest of this chapter goes into depth about each of the blocks in the adaptive sensing framework and how they interact. A simple range sensor is used throughout this chapter to give insight into the algorithm. Chapter 5 will show how adaptive sensing can use electromagnetic induction, EMI, for UXO discrimination and how it is modified to include a target library.

4.1 Sensor Model: Range Sensor

A 2D range sensor was chosen as a simple sensor model that could be used to test the algorithm. The vectors $\theta_r \in \Re^{2\times 1}$ and $x_{\text{UXO}} \in \Re^{2\times 1}$ represent the 2D Cartesian coordinates of the range sensor and the target respectively. Figure 4.2 shows two range sensors detecting a target. The blue circle that surrounds each sensor shows a contour where a target along that line would cause that sensor to have the same measurement, z.

$$z = \| \, x_{\text{UXO}} - \theta_r \, \|_2 \tag{4.1}$$

4.2 Cost Function: Information Metrics

There are many metrics that can capture the amount of information that is known about a target. The state vector x represents the n parameters of interest that describe the target. A posterior probability distribution, $P(x)$, is placed around that state vector quantifying the potential possibilities. If the distribution is Gaussian, many of these metrics will be directly related. The following sections will mathematically describe these metrics, consider their utility, and examine the Gaussian assumption.

4.2.1 Covariance Matrix

The covariance matrix, Σ_x, is the most common measure of the spread of a probability distribution. It is by definition positive semidefinite and symmetric. The diagonals of the matrix are variances for each of the state's parameters while the off diagonal terms are covariances between one parameter and another. The ith parameter in the vector is represented by $x[i]$. The matrix is diagonal if all the parameters are independent of each other and the elements are small if the uncertainty in the corresponding states are small.

$$\Sigma_x = E\left[x - \bar{x}\right]^2 \tag{4.2}$$

$$= \begin{bmatrix} E\left[x[1] - \bar{x}[1]\right]^2 & \dots & E\left[x[1] - \bar{x}[1]\right] E\left[x[n] - \bar{x}[n]\right] \\ \vdots & \ddots & \vdots \\ E\left[x[n] - \bar{x}[n]\right] E\left[x[1] - \bar{x}[1]\right] & \dots & E\left[x[n] - \bar{x}[n]\right]^2 \end{bmatrix} \tag{4.3}$$

If the distribution is Gaussian, then the entire estimate can be described by its mean, $\bar{x}$, and covariance, Σ_x [28, 98].

$$x \sim N(\bar{x}, \Sigma_x) \tag{4.4}$$

4.2.2 Fisher's Information Matrix

Fisher's information matrix, I_x^F, is defined in Equation 4.5. It quantifies the sensitivity of a continuous distribution to changes in the state. As the sensitivity increases, the information matrix will become larger representing the fact that the parameters should be easier to

estimate. If the probability distribution is fairly flat, then the second derivatives would be close to zero signifying little information can be gained.

$$I_x^F = \frac{d^2}{dx^2} \log(P(x)) \tag{4.5}$$

Fisher's information matrix reduces to the inverse of the covariance matrix if x has a normal distribution [28, 35].

$$I_x^F = \Sigma_x^{-1} \tag{4.6}$$

4.2.3 Shannon's Information

Shannon's information, I_x^S, is also known as entropic information. It relates to the differential entropy, H_x, of a system by Equation 4.8. Differential entropy is a scalar value representing the average uncertainty. Shannon's information is maximized in the discrete case for a compact distribution such as a Dirac delta distribution. In this case, H_x is 0. For all other discrete distributions, H_x is positive and Shannon's information is negative. Those constraints are not held for continuous distributions.

$$\begin{aligned} H_x &= -E[\log P(x)] \\ &= -\int_{-\infty}^{\infty} P(x) \log P(x) dx \end{aligned} \tag{4.7}$$

$$I_x^S = -H_x \tag{4.8}$$

Again, is has been shown that Shannon's information is related to $|\Sigma_x|$ if the underlying distribution is normal. This determinant is proportional to the area of a 2D uncertainty ellipse or to the volume of a 3D uncertainty ellipsoid [23, 35].

$$I_x^S = -\frac{1}{2} \log \left[(2\pi e)^n |\Sigma_x| \right] \tag{4.9}$$

4.2.4 Mutual Information

Mutual information, $I^M_{x,z}$, represents the average reduction of uncertainty in the target state, x, due to a potential sensor measurement z. If the random variables are independent, the $\log$ term in Equation 4.11 will go to zero as no information is gained with these measurements.

$$\begin{aligned} \bar{H}_{x|z} &= -E[\log P(x)] \\ &= -\int_{-\infty}^{\infty}\int_{-\infty}^{\infty} P(x,z)\log P(x|z)dxdz \end{aligned} \tag{4.10}$$

$$\begin{aligned} I^M_{x,z} &= -E\left[\log \frac{P(x,z)}{P(x)P(z)}\right] \\ &= -\int_{-\infty}^{\infty}\int_{-\infty}^{\infty} P(x,z)\log \frac{P(x,z)}{P(x)P(z)}dxdz \\ &= H_x - \bar{H}_{x|z} \end{aligned} \tag{4.11}$$

Mutual information can also be related to relative entropy or Kullback Leibler distance, $D()$, which measures the distance between two probability densities.

$$D(f \parallel g) = \int f \log \frac{f}{g} \tag{4.12}$$

$$I^M_{x,z} = D(P(x,z) \parallel P(x)P(z))$$

Given linear functions and a Gaussian distribution, Logothetis determined that mutual information between a state and a set of measurements is a relationship between prior uncertainty,$\widetilde{\Sigma}_x$, and the posterior uncertainty, $\Sigma_{x|Z}$ given the entire measurement sequence. [23, 28, 37, 56].

$$I^M_{x,z} = -\frac{1}{2}\log \frac{|\widetilde{\Sigma}_x|}{|\Sigma_{x|Z}|} \tag{4.13}$$

4.2.5 Summary

All of these information metrics require a posterior distribution to be calculated given previous measurements. The estimators presented in the next section are specifically devoted

to that task. Frew makes an argument that the covariance matrix should be used to represent information because that is what estimators typically propagate. The covariance matrix will therefore include the nonlinear effects of whichever estimator is chosen [28]. As a bit of foreshadowing, the best estimator for the adaptive sensing constraints of this thesis is a nonlinear form of the Kalman filter. The estimator works best with Gaussian distributions and propagates Σ_x. Recall that given the Gaussian assumption, Fisher's, Shannon's and mutual information are all tied directly to the same uncertainty matrix and therefore $|\Sigma_x|$ will be used to measure information.

Kullback Leibler distance is an interesting way of measuring the separation of distributions. It could be used to find the measurements that would distinguish one hypothesis over another hypothesis. However, this requires a good understanding of the probability function for each hypothesis and is conditioned on the two hypotheses covering all possibilities. $|\Sigma_x|$ avoids that by only considering the parameters of the target.

4.3 Estimator: Parameter Estimation

The adaptive sensing framework uses a recursive Bayesian estimator to incorporate new measurements into the current estimate of the target parameters and its uncertainty. Because the target parameters are static, this estimation procedure is known as parameter estimation [100]. The following section discusses the parameter estimation version of the particle filter and various forms of the Kalman filter.

Parameter estimation is used to estimate the state x given a set of z measurements. The state, x_t, represents the estimate of the target's parameters at time t. The sensor states are defined by θ_t and can include the sensor's location and orientation. The state update function, $g()$, for parameter estimation is an identity function, Equation 4.15, affected by noise ε_t. The noise in the state update function should be zero because the state is not changing, however in some of the estimators the value must be non-zero to allow the state estimate to change. The measurement function, $h()$, is also corrupted by some noise δ_t.

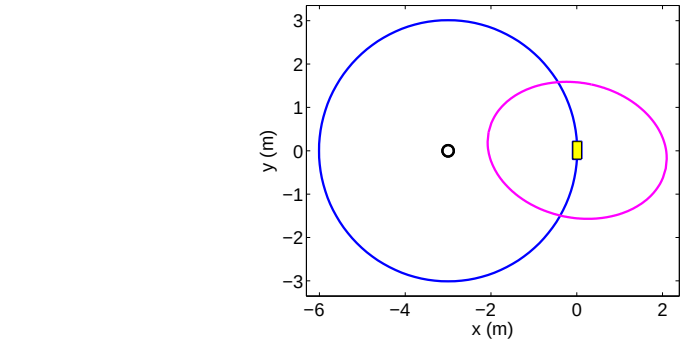

(a) Scene setup

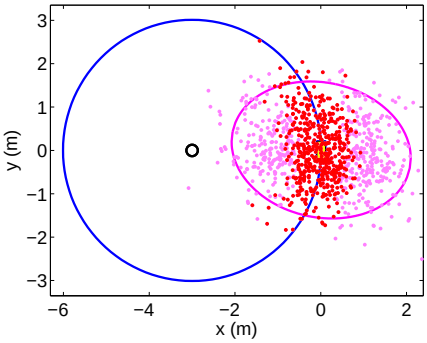

(b) Particle filter

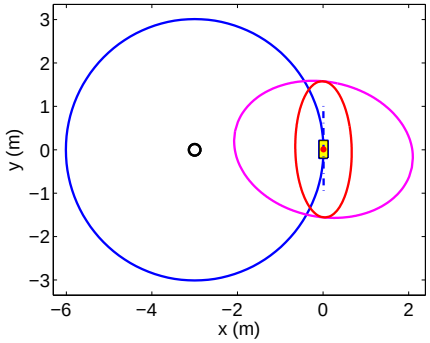

(c) Extended Kalman filter

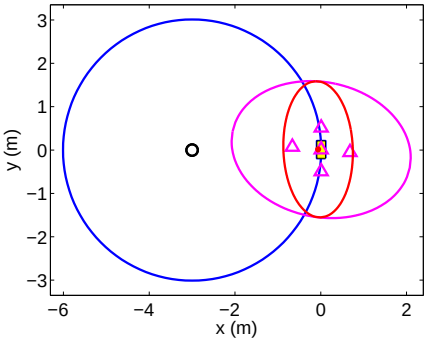

(d) Sigma-Point Kalman filter

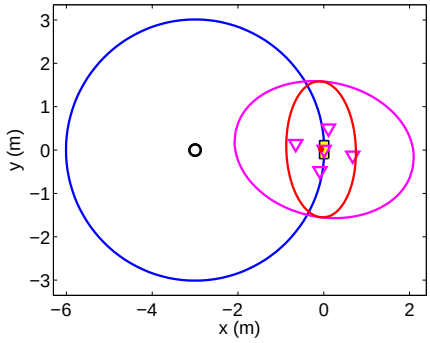

(e) Eigenvector sigma-point Kalman filter

Figure 4.3: Comparison of estimators with a range sensor

(a) The blue line is the sensor contour for a range sensor. The target estimate is the yellow rectangle with a magenta uncertainty ellipse. The estimated location of the target is correct for this comparison. (b)-(e) show the posterior estimate and uncertainty of the target in red after a perfect sensor measurement is taken. The triangles are where the sigma-points are located in the sigma-point filters.

$$x_t = g(x_{t-1}, u_t) + \varepsilon_t \tag{4.14}$$
$$= x_{t-1} + \varepsilon_t \tag{4.15}$$

$$z_t = h(x_t, \theta_t) + \delta_t \tag{4.16}$$

Figure 4.3 compares the different estimators using a range sensor in an artificial situation. The blue line shows possible target locations where a sensor located at the black circle will return the same signal. The prior estimate is correct in that the mean is directly located on the actual location of the target shown as the yellow rectangle. The prior uncertainty is shown for each estimator in magenta. A measurement is taken for each estimator with no noise and the red posterior estimate is plotted. The posterior estimate is still large because the estimator is still incorporating the possibility of noise into its estimates.

4.3.1 Particle Filter

The particle filter, PF, is a Monte Carlo based estimator that can handle nonlinear functions along with non-Gaussian and multi-modal distributions. In Figure 4.3b, the initial uncertainty is represented by a magenta cloud of particles that are randomly distributed according to the prior distribution. After the measurement is taken, the particles are resampled to represent the posterior distribution which is roughly a subset of the initial particles that are closest to the sensor contour because they are the most likely to be correct.

The full PF algorithm is presented in detail in many sources such as [98] and [100]. This estimator uses a nonzero value for the noise in the state function to allow the state estimates to move around searching for the solution. The PF is compared in Section 4.4.1 with other estimators to generate an information metric. The PF is used as the most accurate estimator because it does not suffer from the Gaussian assumption. However, the section will also show the scaling issues that make the PF a poor choice for this research.

Table 4.1: Extended Kalman filter

Standard	Parameter estimation
$\bar{x}_t = g(x_{t-1})$	$\bar{x}_t = x_{t-1}$
$\bar{\Sigma}_{x_t} = G_t \Sigma_{x_{t-1}} G_t^T + \Sigma_\varepsilon$	$\bar{\Sigma}_{x_t} = \Sigma_{x_{t-1}}$
$K_t = \bar{\Sigma}_{x_t} H_t^T (H_t \bar{\Sigma}_{x_t} H_t^T + \Sigma_\delta)^{-1}$	$K_t = \bar{\Sigma}_{x_t} H_t^T (H_t \bar{\Sigma}_{x_t} H_t^T + \Sigma_\delta)^{-1}$
$x_t = \bar{x}_t + K_t(z_t - h(\bar{x}_t))$	$x_t = \bar{x}_t + K_t(z_t - h(\bar{x}_t))$
$\Sigma_{x_t} = (I - K_t H_t)\bar{\Sigma}_{x_t}$	$\Sigma_{x_t} = (I - K_t H_t)\bar{\Sigma}_{x_t}$

Table 4.2: Extended information filter

Standard	Parameter estimation
$x_{t-1} = \Omega_{x_{t-1}}^{-1} \xi_{t-1}$	$x_{t-1} = \Omega_{x_{t-1}}^{-1} \xi_{t-1}$
$\bar{\Omega}_{x_t} = (G_t \Omega_{x_{t-1}}^{-1} G_t^T + \Sigma_\varepsilon)^{-1}$	$\bar{\Omega}_{x_t} = \Omega_{x_{t-1}}$
$\bar{\xi}_t = \bar{\Omega}_{x_t} g(x_{t-1})$	$\bar{\xi}_t = \bar{\Omega}_{x_t} x_{t-1}$
$\bar{x}_t = g(x_{t-1})$	$\bar{x}_t = x_{t-1}$
$\Omega_{x_t} = \bar{\Omega}_{x_t} + H_t^T \Sigma_\delta^{-1} H_t$	$\Omega_{x_t} = \bar{\Omega}_{x_t} + H_t^T \Sigma_\delta^{-1} H_t$
$\xi_t = \bar{\xi}_t + H_t^T \Sigma_\delta^{-1}(z_t - h(\bar{x}_t, \theta_t) + H_t \bar{x}_t)$	$\xi_t = \bar{\xi}_t + H_t^T \Sigma_\delta^{-1}(z_t - h(\bar{x}_t, \theta_t) + H_t \bar{x}_t)$

4.3.2 Extended Kalman Filter & Extended Information Filter

The extended Kalman filter, EKF, and the extended information filter, EIF, are nonlinear variations of the Kalman filter which is an optimal filter for linear Gaussian systems. While the Kalman filter itself does not require Gaussian distributions, it is sub optimal when those conditions are not met because it only propagates the first and second order moments of the distribution. The EKF and EIF use a first order Taylor series to linearize the functions around the target estimate. The blue vertical line in Figure 4.3c shows the linearized version of the sensor function. The posterior estimate remains Gaussian and the mean does not change. Comparing it with the PF the ellipse captures most of the actual distribution, but it leaves out the top and bottom section of the distribution that follows the sensor contour.

Both algorithms are presented in Tables 4.1 and 4.2. The linearization is done with two Jacobian matrices, G_t and H_t. The EIF stores the estimate in an information vector, ξ_t, and an information matrix, Ω_{x_t} [98, 100].

$$\Omega_{x_t} = \Sigma_{x_t}^{-1} \tag{4.17}$$

$$\xi_t = \Omega_{x_t} x_t \tag{4.18}$$

$$G_t = \frac{\partial g(x)}{\partial x}|_{x=x_t} \tag{4.19}$$

$$H_t = \frac{\partial h(x, \theta_t)}{\partial x}|_{x=x_t} \tag{4.20}$$

The EKF and the EIF update the estimates in different manners, but the results are mathematically equivalent. The EIF is computationally favorable when the estimator is incorporating new information without immediately calculating an estimate. The EKF has to run through the entire algorithm to update Σ_{x_t}. The EIF updates the uncertainty using Equation 4.21 without worrying about updating the state. This simplification is what researchers take advantage of for decentralized estimation and sensor fusion.

$$\Omega_{x_t} = \Omega_{x_{t-1}} + H_t^T \Sigma_\delta^{-1} H_t \tag{4.21}$$

There are two subtleties to notice from these algorithms. First, if the measurement taken matches with the predicted measurement, then the estimate mean does not change. This can be seen in line 4 of the EKF algorithm. It can also be seen in Figure 4.4a where the posterior mean is at the same location as the prior. The second thing to notice is that the update in the posterior uncertainty is independent of the prior uncertainty. Equation 4.21 shows the amount of change in the information matrix is entirely due to the sensor function and independent of the prior information matrix.

4.3.3 Sigma-Point Kalman Filter & Sigma-Point Information Filter

The sigma-point Kalman filter, SPKF, is a more recent nonlinear variation of the Kalman filter [41]. Instead of linearizing the functions, SPKF models the estimate as a set of $2n + 1$ specially chosen points. These points cover the same parameter space as the target estimate, but are spaced in such a way that they capture the uncertainty distribution. Figure 4.3d shows the sigma-points for the prior distribution as a set of triangles. These sigma-points are run through the estimator with the new measurement to come up with a second set of sigma-points that represent the posterior distribution. This new uncertainty ellipse captures more of the top and bottom sections of the PF distribution.

Table 4.3: Sigma-Point Kalman filter

<table>
<tr><th colspan="2">Variables</th></tr>
<tr><td colspan="2">$\lambda = \alpha^2(n+\kappa) - n$
$\gamma = \sqrt{n+\lambda}$
$w_m^0 = \frac{\lambda}{n+\lambda}$
$w_c^0 = \frac{\lambda}{n+\lambda} + 1 - \alpha^2 + \beta$
$w_m^i = w_c^i = \frac{1}{2(n+\lambda)}$ for $i = 1, \ldots, 2n$</td></tr>
<tr><th>Standard</th><th>Parameter estimation</th></tr>
<tr><td>$X_{t-1} = x_{t-1} + \ldots$
$\begin{bmatrix} 0 & \gamma\sqrt{\Sigma_{x_{t-1}}} & -\gamma\sqrt{\Sigma_{x_{t-1}}} \end{bmatrix}$
$\bar{X}_t^* = g(X_{t-1})$
$\bar{x}_t = \sum_{i=0}^{2n} w_m^i \bar{X}_t^{*i}$
$\bar{\Sigma}_{x_t} = \sum_{i=0}^{2n} w_c^i (\bar{X}_t^{*i} - \bar{x}_t)(\bar{X}_t^{*i} - \bar{x}_t)^T + \Sigma_\varepsilon$
$\bar{X}_t = \bar{x}_t + \begin{bmatrix} 0 & \gamma\sqrt{\bar{\Sigma}_{x_t}} & -\gamma\sqrt{\bar{\Sigma}_{x_t}} \end{bmatrix}$</td><td>$X_{t-1} = x_{t-1} + \ldots$
$\begin{bmatrix} 0 & \gamma\sqrt{\Sigma_{x_{t-1}}} & -\gamma\sqrt{\Sigma_{x_{t-1}}} \end{bmatrix}$
$\bar{x}_t = x_{t-1}$
$\bar{\Sigma}_{x_t} = \Sigma_{x_{t-1}}$
$\bar{X}_t = X_{t-1}$</td></tr>
<tr><td colspan="2">$\bar{Z}_t = h(X_t, \theta_t)$
$\hat{z}_t = \sum_{i=0}^{2n} w_m^i \bar{Z}_t^i$
$\bar{\Sigma}_{z_t} = \sum_{i=0}^{2n} w_c^i (\bar{Z}_t^i - \hat{z}_t)(\bar{Z}_t^i - \hat{z}_t)^T + \Sigma_\delta$
$\bar{\Sigma}_{x_t,z_t} = \sum_{i=0}^{2n} w_c^i (\bar{X}_t^i - \bar{x}_t)(\bar{Z}_t^i - \hat{z}_t)^T$
$K_t = \bar{\Sigma}_{x_t,z_t} \bar{\Sigma}_{z_t}^{-1}$
$x_t = \bar{x}_t + K_t(z_t - \hat{z}_t)$
$\Sigma_{x_t} = \bar{\Sigma}_{x_t} - K_t \bar{\Sigma}_{z_t} K_t^T$</td></tr>
</table>

The SPKF enjoys some distinct advantages over the EIF and the EKF. Empirical evidence has shown that the SPKF handles nonlinear equations better and is less likely to diverge when compared to EKF [40, 53]. Perea et al. observed the SPKF handles large uncertainties better than the EKF [76]. One reason is the SPKF is accurate to the second order of the Taylor series. SPKF also takes into account initial uncertainty when propagating both the mean and covariance. From an implementation perspective, SPKF offers a significant advantage in that no Jacobian is ever calculated because the sigma-points are propagated directly through the state and measurement functions [100].

The standard SPKF algorithm and its parameter estimation version are written out in Table 4.3. The first part of the table details out some of the SPKF specific variables. The second portion describes the prediction step of the standard version and the parameter estimation version of the SPKF. The third section contains the equations for the measurement

Table 4.4: Sigma-Point information filter

Standard	Parameter estimation
$X_{t-1} = x_{t-1} + \dots$ $\begin{bmatrix} 0 & \gamma\sqrt{\Sigma_{x_{t-1}}} & -\gamma\sqrt{\Sigma_{x_{t-1}}} \end{bmatrix}$ $\bar{X}_t^* = g(X_{t-1})$ $\bar{x}_t = \sum_{i=0}^{2n} w_m^i \bar{X}_t^{*i}$ $\bar{\Sigma}_{x_t} = \sum_{i=0}^{2n} w_c^i (\bar{X}_t^{*i} - \bar{x}_t)(\bar{X}_t^{*i} - \bar{x}_t)^T + \Sigma_\varepsilon$ $\bar{X}_t = \bar{x}_t + \begin{bmatrix} 0 & \gamma\sqrt{\bar{\Sigma}_{x_t}} & -\gamma\sqrt{\bar{\Sigma}_{x_t}} \end{bmatrix}$	$X_{t-1} = x_{t-1} + \dots$ $\begin{bmatrix} 0 & \gamma\sqrt{\Sigma_{x_{t-1}}} & -\gamma\sqrt{\Sigma_{x_{t-1}}} \end{bmatrix}$ $\bar{x}_t = x_{t-1}$ $\bar{\Sigma}_{x_t} = \Sigma_{x_{t-1}}$ $\bar{X}_t = X_{t-1}$
$\bar{\Omega}_{x_t} = \bar{\Sigma}_{x_t}^{-1}$ $\bar{\xi}_t = \bar{\Omega}_{x_t} \bar{x}_t$ $\bar{Z}_t = h(\bar{X}_t, \theta_t)$ $\hat{z}_t = \sum_{i=0}^{2n} w_m^i \bar{Z}_t^i$ $\bar{\Sigma}_{z_t} = \sum_{i=0}^{2n} w_c^i (\bar{Z}_t^i - \hat{z}_t)(\bar{Z}_t^i - \hat{z}_t)^T + \Sigma_\delta$ $\bar{\Sigma}_{x_t,z_t} = \sum_{i=0}^{2n} w_c^i (\bar{X}_t^i - \bar{x}_t)(\bar{Z}_t^i - \hat{z}_t)^T$ $L_t = \bar{\Omega}_{x_t}^T \bar{\Sigma}_{x_t,z_t} (\bar{\Sigma}_{z_t} - \bar{\Sigma}_{x_t,z_t}^T \bar{\Omega}_{x_t}^T \bar{\Sigma}_{x_t,z_t})^{-1}$ $\Omega_{x_t} = \bar{\Omega}_{x_t} + L_t \bar{\Sigma}_{x_t,z_t}^T \bar{\Omega}_{x_t}$ $\xi_t = \bar{\xi}_t + L_t (z_t - \hat{z}_t + \bar{\Sigma}_{x_t,z_t}^T \bar{\Omega}_{x_t} \bar{x}_t)$	

update section of the filter which is the same for both uses of the SPKF [98].

Vercauteren and Wang develop the information form of this filter shown in Table 4.4 [97, 102]. Unlike the EIF , there is not a significant computational savings by using this form because each uncertainty update requires the entire algorithm to be run.

There is also a square root form of the sigma-point Kalman filter written in Table 4.5 that is both computationally cheaper and numerically stable. This is the version of the SPKF implemented in this thesis with $g()$ as an identity function and $\Sigma_\varepsilon = 0$ when used for parameter estimation. Merwe and Wan also have a parameter estimation version of this algorithm that is computationally simpler [101].

Figure 4.4 enlarges the posterior estimate from the EKF and SPKF comparisons in Figure 4.3. The EKF mean does not change from its original estimate because the measurement is exactly what the filter expects. The SPKF mean moves slightly off from the original estimate despite the correct initial estimate and a perfect measurement. From a high level perspective, the filter is trying to capture the tails of the distribution that curves along with the sensor contour. By shifting the mean, the uncertainty ellipse is able to capture more of

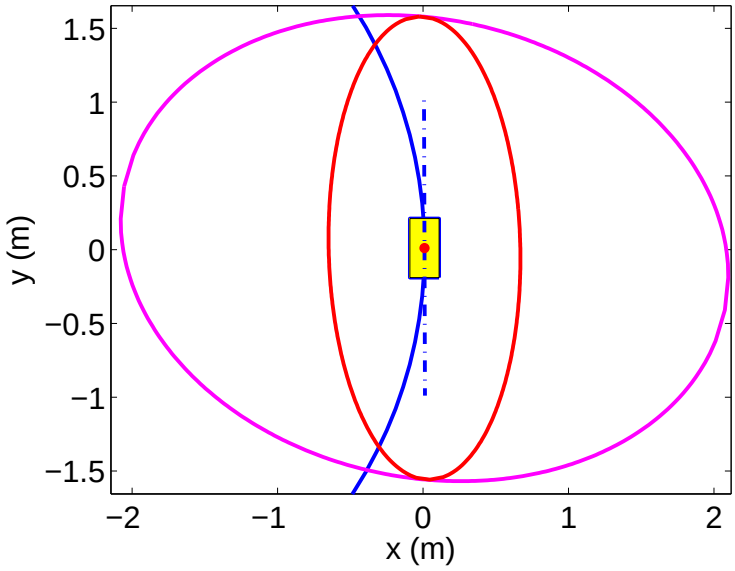

(a) EKF

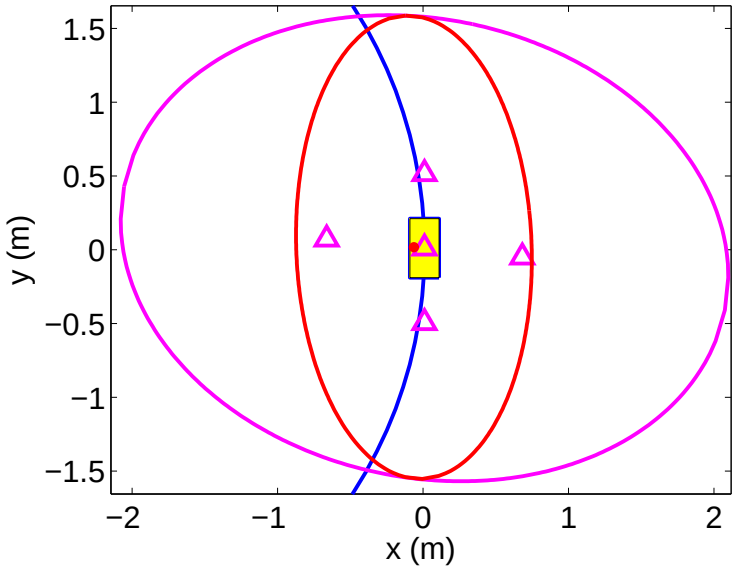

(b) SPKF

Figure 4.4: Zooming in on posterior estimate

This figure takes a closer look at the posterior distributions in Figures 4.3c and 4.3d. The EKF*'s posterior estimate does not move from its original location, but the* SPKF*'s estimate does. This is caused by the* SPKF *algorithm trying to follow the leftwards curve of the sensor contour.*

Table 4.5: Square root sigma-point Kalman filter [101]

$$
\begin{array}{c}
S_{x_{t-1}} = \text{chol}(\Sigma_{x_{t-1}}) \\
X_{t-1} = x_{t-1} + \begin{bmatrix} 0 & \gamma S_{x_{t-1}} & -\gamma S_{x_{t-1}} \end{bmatrix} \\
\bar{X}^*_t = g(X_{t-1}) \\
\bar{x}_t = \sum_{i=0}^{2n} w_m^i \bar{X}_t^{*i} \\
\bar{S}_{x_t} = \text{qr}\left(\begin{bmatrix} \sqrt{w_c^1}(\bar{X}^*_{t,1:2n} - \bar{x}_t) & \sqrt{\Sigma_\varepsilon} \end{bmatrix}\right) \\
\bar{S}_{x_t} = \text{cholupdate}\left(\bar{S}_{x_t}, \quad \bar{X}^*_{t,0} - \bar{x}_t, \quad w_c^0 \right) \\
\bar{X}_t = \bar{x}_t + \begin{bmatrix} 0 & \gamma \bar{S}_{x_t} & -\gamma \bar{S}_{x_t} \end{bmatrix} \\
\hline
\bar{Z}_t = h(\bar{X}_t, \theta_t) \\
\hat{z}_t = \sum_{i=0}^{2n} w_m^i \bar{Z}_t^i \\
\bar{S}_{z_t} = \text{qr}\left(\begin{bmatrix} \sqrt{w_c^1}(\bar{Z}_{t,1:2n} - \hat{z}_t) & \sqrt{\Sigma_\delta} \end{bmatrix}\right) \\
\bar{S}_{z_t} = \text{cholupdate}\left(\bar{S}_{z_t}, \quad \bar{Z}_{t,0} - \hat{z}_t, \quad w_c^0 \right) \\
\bar{\Sigma}_{x_t,z_t} = \sum_{i=0}^{2n} w_c^i (\bar{X}_t^i - \bar{x}_t)(\bar{Z}_t^i - \hat{z}_t)^T \\
K_t = (\bar{\Sigma}_{x_t,z_t} / \bar{S}_{z_t}^T) / \bar{S}_{z_t} \\
x_t = \bar{x}_t + K_t(z_t - \hat{z}_t) \\
U = K_t \bar{S}_{z_t} \\
S_{x_t} = \text{cholupdate}\left(\bar{S}_{x_t}, \quad U, \quad -1 \right)
\end{array}
$$

those possibilities. Examining the filter will reveal the cause of this.

$$x_t = \bar{x}_t + \Sigma_{x_t,z_t} \Sigma_{x_t}^{-1} (z_t - \hat{z}) \tag{4.22}$$

Equation 4.22 updates state uncertainty for the SPKF and is reproduced from Table 4.3. If it is given the correct initial state, then Equation 4.23 needs to be true for x_t to not change. Keep in mind that $\hat{z}$ is not just the predicted sensor measurement of the mean estimate, but a combination of the predicted measurements from each sigma-point. This can also be seen in the calculation of $\hat{z}$ in Table 4.3 and rewritten in Equation 4.25. The matrix, $\Sigma_{z_t}^{-1}$, must be positive definite because, Σ_{z_t} must be positive semi-definite and invertible. One option for the mean to not change is for Σ_{x_t,z_t} to be equal to a zero matrix. A second option would be for $z = \hat{z}$.

$$\Sigma_{x_t,z_t} \Sigma_{x_t}^{-1} (z_t - \hat{z}) = [0, ..., 0]^T \tag{4.23}$$

$$\bar{\Sigma}_{x_t,z_t} = \sum_{i=0}^{2n} w_c^i (\bar{X}_t^i - \bar{x}_t)(\bar{Z}_t^i - \hat{z}_t)^T \tag{4.24}$$

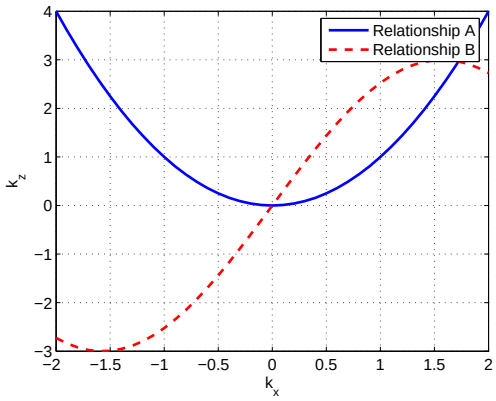

Figure 4.5: Relationships that eliminate SPKF bias

This plot show some simple relationships between sample 1D nonlinear sensor models which will not lead to a biased SPKF estimate. The axes are the x and z variables shifted so that the plots are centered at the origin.

$$\hat{z}_t = \sum_{i=0}^{2n} w_m^i (h(\bar{X}_t^i, \theta_t)) \tag{4.25}$$

Figure 4.5 shows examples of symmetry between x and z that can occur which will eliminate bias. Using Equation 4.24, if the measurement function is symmetric like relationship A from Figure 4.5, then $\bar{\Sigma}_{x_t,z_t}$ will be a zero matrix. Using Equation 4.25, if the measurement function is antisymmetric like relationship B, then $z_t = \hat{z}_t$.

$$k_x = x - \hat{x} \tag{4.26}$$

$$k_z = h(x,\theta) - h(\hat{x},\theta) \tag{4.27}$$

$$= h(x,\theta) - \hat{z} \tag{4.28}$$

4.3.4 Square Root Eigenvector Sigma-Point Kalman Filter

Julier and Ulhman's original paper on sigma-point filters states that any matrix square root can be used to calculate the $2n+1$ sigma-points with the following equation from Table 4.3 [41].

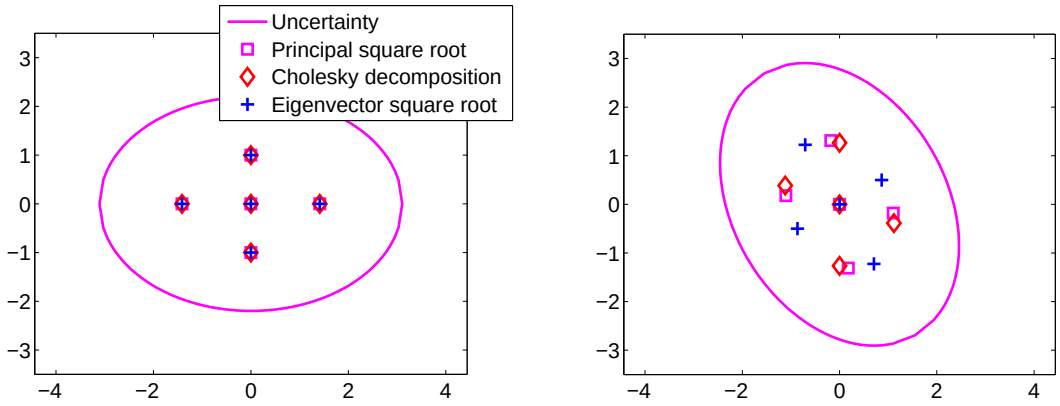

(a) Original uncertainty ellipse

(b) Rotated uncertainty ellipse

Figure 4.6: Various matrix square roots to calculate sigma-points

This plots several sets of sigma-points that describe an uncertainty ellipse. Each set is calculated with a different type of matrix square root. Only the eigenvector square root rotates with the ellipse.

$$X = x + \begin{bmatrix} 0 & \gamma\sqrt{\Sigma_x} & -\gamma\sqrt{\Sigma_x} \end{bmatrix} \tag{4.29}$$

The square root filter in the previous section uses the Cholesky decomposition to calculate the sigma-points. Any symmetric positive definite matrix can be broken down into a lower triangular real matrix, L, and its conjugate transpose. Note that the `MATLAB chol` function actually produces the upper triangular matrix unless specified.

$$\Sigma_x = LL^* \tag{4.30}$$

Another option is the principal square root which returns two identical roots. This is also the `MATLAB sqrtm` function.

$$\Sigma_x = SS \tag{4.31}$$

Figure 4.6 shows these sigma-points plotted on two uncertainty ellipses that are rotated relative to each other. The sigma-points from the Cholesky decomposition and the principal square root do not stay fixed to the ellipse. The effect this has on adaptive sensing is

discussed in Section 4.4.3.

There are three ways to mask the rotational effect of sigma-points. The first method is to rotate the entire coordinate frame of the system so that when the sigma-points are calculated, the axes are aligned with the major and minor axis of the ellipse. After they are calculated, rotate everything back into the world frame. This is a difficult strategy especially as the number of states increase. Another technique is to force the sigma-points to be close to the state estimate by reducing α or κ in Table 4.3. This method forces the SPKF to capture less of the nonlinearities in the measurement function, but improves its rotational consistency.

The last technique is something originally mentioned by Julier and Ulhman. Fix the sigma-points to the eigenvectors [41]. A singular value decomposition is done on the result of the Cholesky decomposition to get the eigenvectors. The square root form can also be used for this adaptation of the SPKF, and it will be referred to as the eigenvector sigma-point Kalman filter, eSPKF.

$$
\begin{aligned}
L &= U\Sigma_s V^T && (4.32)\\
\Sigma_x &= U\Sigma_L V^T V \Sigma_L^T U^T && (4.33)\\
&= U\Sigma_L \Sigma_L^T U^T && (4.34)\\
&= L'L'^T && (4.35)\\
L' &= U\Sigma_L && (4.36)
\end{aligned}
$$

4.4 Cost Maps

The estimators are now used to calculate a cost for where to place a range sensor in a 2D scenario. Higher cost means less information is obtained from that location. In Figures 4.7 and 4.8, the magenta ellipse is the initial uncertainty ellipse about the original estimate centered at the origin. The contour plots are the cost of placing a sensor at that location. The following sections explain why the eSPKF is preferred when propagating estimates to determine a cost.

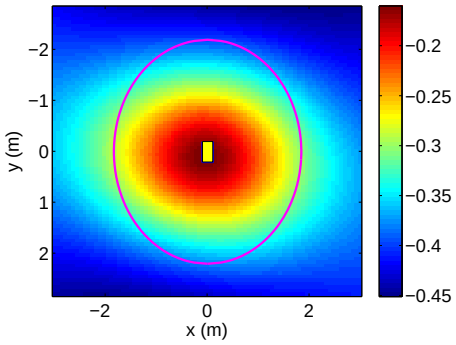

(a) PF cost map

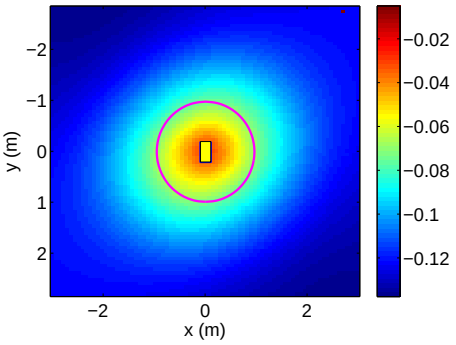

(b) PF cost map with reduced prior uncertainty

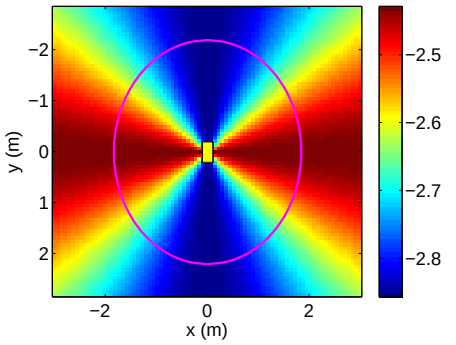

(c) EIF cost map

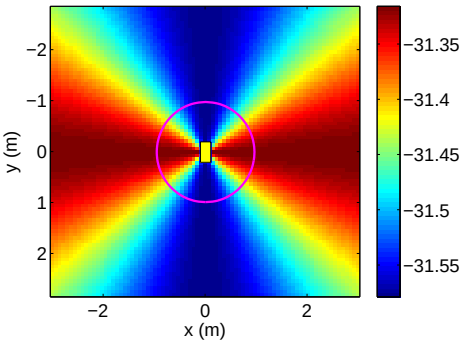

(d) EIF cost map with reduced prior uncertainty

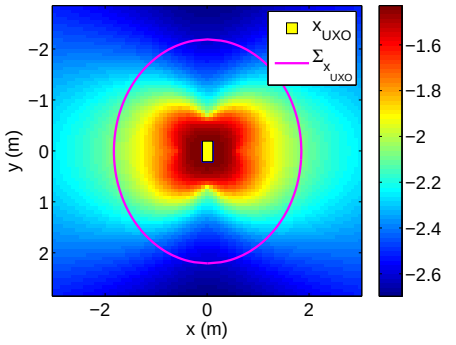

(e) eSPKF cost map

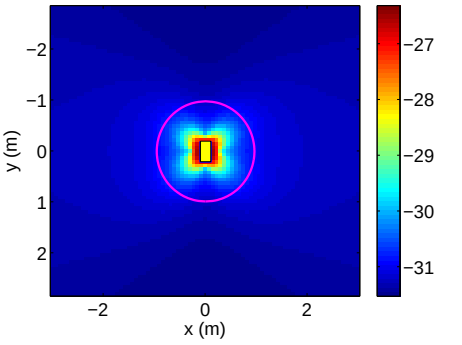

(f) eSPKF cost map with reduced prior uncertainty

Figure 4.7: Estimator cost maps with reduced priors

These cost maps are generated to determine where to place a range sensor to maximize information. The initial estimate is centered at the origin and the magenta ellipse shows the prior uncertainty.

4.4.1 Particle Filter Cost Map

The PF approach calculates mutual information with the technique developed by Hoffmann, [37]. Figures 4.7a and 4.7b plot the negative of the mutual information so that information is maximized when cost is minimized. For the first figure, the map suggests placing the sensor far away from the center. If the sensor is right next to the target, then the sensor signal might get washed out in the noise because the signal is weak. Remember, in this artificial situation, the signal is simply a distance value so the closer the sensor is to the target the weaker the signal. Moreover, the real sensor used in the next chapter returns a stronger value as it nears the target. The map also says that there is a preference to be somewhere along the vertical axis. The initial ellipse is longer along the vertical axis, so the sensor needs to be placed on that axis to reduce that uncertainty the quickest. Imagine a sensor placed on the vertical axis, the circular sensor contour would cross the target with its tangent along the horizontal axis. That reading will provide information along the vertical axis, and less information along the horizontal.

The initial uncertainty is reduced to nearly circular in Figure 4.7b. This causes the cost map to change shape. The preference to move the sensor further away from the center is still present. The contour is shifted a little bit, and this is due to randomness inherent to the particle filter.

The weakness in this approach is the computational complexity. An inherent problem with the PF is that the larger number of states that are being estimated, the more particles are needed to accurately capture the distribution. One hundred cost calculations took a Pentium 4 1.8 GHz computer 30.8 seconds for 500 particles and 58.3 seconds for 1000 particles.

4.4.2 Extended Information Filter Cost Map

The EIF and EKF costs use $|\Sigma_x|$ as the information metric which was explained in Section 4.2.5. They produce identical results so only the EIF plots are presented here in Figures 4.7c and 4.7d. The trend of putting the sensor on the vertical axis agrees with the PF approach. However, the EIF form does not care how far the sensor is from the target. Recall Equation 4.21, the only dependence of updating state uncertainty is on the expected noise levels,

Σ_δ, and the Jacobian of the measurement function, H. There is no dependence on the signal-to-noise ratio.

The initial uncertainty is reduced to nearly circular again in Figure 4.7d. The recommendation of this approach does not change. It still says to place the sensor on the vertical axis, and ignores everything else. The estimator is showing that it ignores any uncertainty in the state when it determines how much the new measurement will affect uncertainty, the second portion of Equation 4.21.

While the linearization affects that cause the issues above weaken the estimator's ability to capture information, it does allow an analytical solution to be found to calculate cost for T number of sensor readings. As shown in Table 4.2, the update for uncertainty is Equation 4.21. The state is not updated because the predicted sensor measurement uses the same sensor model and there will be no innovation in the update step. The measurement function's Jacobian, H_t, can be shown to be dependent only on the sensor's orientation, ϕ_t, relative to the target fixed coordinate frame and independent of distance.

$$H_t^T = \frac{\Theta_t^r - x_t^r}{\| \Theta_t^r - x_t^r \|_2} \tag{4.37}$$

$$= \begin{bmatrix} \cos\phi_t \\ \sin\phi_t \end{bmatrix} \tag{4.38}$$

The information matrix, Ω_{x_0}, is constant because it represents the prior knowledge about the target and does not change with regards to each trajectory being considered. The noise, Σ_δ, is assumed to be equal and uncorrelated. Equation 4.45 represents an equivalent cost metric that when minimized will also minimize the original cost metric. For an analytical trajectory solution, the best and worst case scenario exist when Equation 4.46 is true.

$$\underset{\Theta_T}{\operatorname{argmin}} J_t = \underset{\Theta_T}{\operatorname{argmin}} - \left| (\Omega_{x_0} + \sum_{t=1..T} H_t^T \Sigma_{\delta_t}^{-1} H_t) \right| \tag{4.39}$$

$$= \underset{\Theta_T}{\operatorname{argmin}} - \left| \sum_{t=1..T} H_t^T \Sigma_{\delta_t}^{-1} H_t \right| \tag{4.40}$$

$$= \underset{\Theta_T}{\operatorname{argmin}} - \left| \sum_{t=1..T} H_t^T H_t \right| \tag{4.41}$$

$$= \underset{\Theta_T}{\operatorname{argmin}} - \left| \begin{bmatrix} \sum_{t=0..T} \cos^2 \phi_t & \sum_{t=0..T} (\cos \phi_t \sin \phi_t) \\ \sum_{t=0..T} (\cos \phi_t \sin \phi_t) & \sum_{t=0..T} \sin^2 \phi_t \end{bmatrix} \right| \tag{4.42}$$

$$= \underset{\Theta_T}{\operatorname{argmin}} J'_T \tag{4.43}$$

$$J'_T = - \left| \begin{bmatrix} \sum_{t=0..T} \cos^2 \phi_t & \sum_{t=0..T} (\cos \phi_t \sin \phi_t) \\ \sum_{t=0..T} (\cos \phi_t \sin \phi_t) & \sum_{t=0..T} \sin^2 \phi_t \end{bmatrix} \right| \tag{4.44}$$

$$J'_T = \sum_{t=0}^{T} \sum_{\tau=0, \tau \neq t}^{T} - \sin^2(\phi_\tau - \phi_t) \tag{4.45}$$

$$\begin{bmatrix} 0 & .. & 0 \end{bmatrix} = \nabla_\phi J'_T \tag{4.46}$$

4.4.3 Regular and Eigenvector Sigma-Point Kalman Filter Cost Map

In this subsection, the SPKF and the eSPKF based cost metrics are applied to the range sensor case. Figures 4.7e and 4.7f show the eSPKF cost maps which are identical to the SPKF cost maps when the ellipses major and minor axes are aligned with the coordinate frame's axes. Both cost maps mimic the corresponding PF cost maps in terms of the preference of putting the sensor far from the target and to place it along the vertical axis. There are cusps in the eSPKF implementation that are due to using sigma-points to linearize the process. In the reduced uncertainty case, the cost map strongly encourages the sensor to be placed away from the target but it does not care about where in orientation. This shows the algorithm accounting for initial uncertainty unlike the EIF approach. The drawback with the PF was the computation time. For the same computer system, 100 cost calculations with the eSPKF

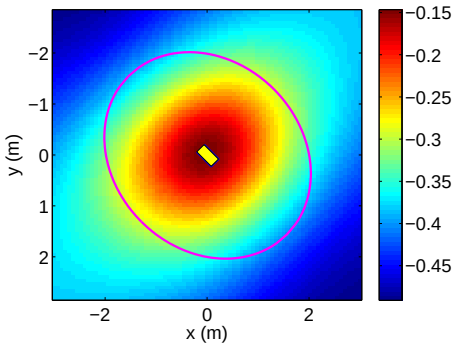

(a) PF cost map with rotated prior uncertainty

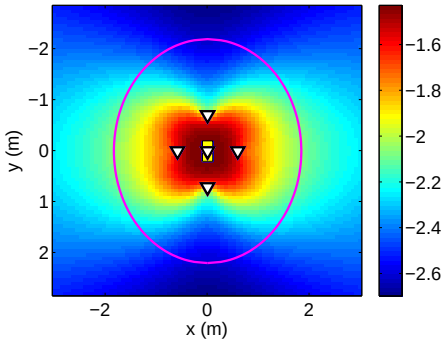

(b) eSPKF cost map

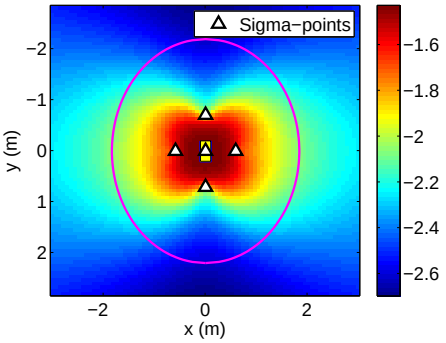

(c) SPKF cost map

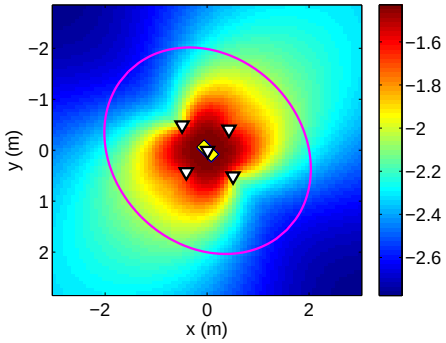

(d) eSPKF cost map with rotated prior uncertainty

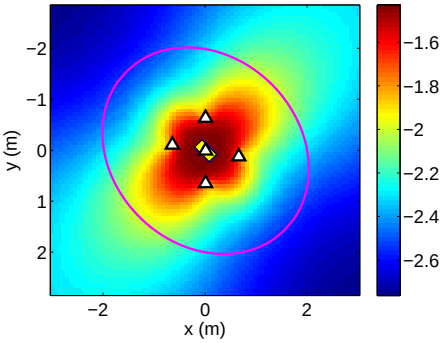

(e) SPKF cost map with rotated prior uncertainty

Figure 4.8: Estimator cost maps with rotated uncertainty ellipses

These cost maps are very similar to the ones displaced in Figure 4.7. They are showing the affect on the estimators caused by a rotated initial uncertainty. The sigma-points are plotted for the figures that use sigma-points.

estimator took 0.75 seconds compared to the PF 30.8 seconds with 500 particles. The eSPKF estimator manages to account for signal-to-noise issues, geometry, and initial uncertainty without the cost calculation penalty. It however, does suffer the effect from doing some linearization as seen by the cusps.

Figure 4.8 looks at what happens when the initial uncertainty is rotated. The expectation is the cost map will rotate with the initial uncertainty because the sensor measurement is only influenced by the distance to the target. The PF plot shows the cost map rotating with the uncertainty ellipse. The SPKF cost map does not rotate with the uncertainty ellipse. It actually changes shape. This means the cost is now dependent on something unrelated to the sensor model. By making the estimator rotationally invariant, that dependence will be eliminated and adaptive sensing can more accurately compare costs from two different sensor locations. The eSPKF cost map exhibits this trait due to its sigma-points moving accordingly.

Aside from geometry and signal-to-noise ratio, the eSPKF cost metric also has a preference for areas that are more linear, or follow relationship B in Figure 4.5, because in those areas the filter can be more aggressive in reducing uncertainty. One of the inherent advantages of the SPKF is that it does not try to over estimate in situations where the sensor function is extremely nonlinear. This can be seen when taking a closer look at the SPKF covariance update step which is rewritten in Equation 4.47.

$$\Sigma_{x_t} = \bar{\Sigma}_{x_t} - \bar{\Sigma}_{x_t,z_t}\bar{\Sigma}_{z_t}^{-1}\bar{\Sigma}_{x_t,z_t}^{T} \tag{4.47}$$

Using the proposition detailed in Table 4.6, by maximizing $|\bar{\Sigma}_{x_t,z_t}\bar{\Sigma}_{z_t}^{-1}\bar{\Sigma}_{x_t,z_t}^{T}|$ the cost metric $|\Sigma_{x_t}|$ is minimized. The assumptions required by the proposition are upheld because the matrices involved are covariance matrices that have some knowledge and some uncertainty relating to all the states. What follows is not an irrefutable proof because it assumes $\bar{\Sigma}_{x_t,z_t}$ is constant, but it does indicate a trend.

Observing $|\bar{\Sigma}_{z_t}|$ will give insight to how linearity in the sensor equation will affect the cost function. Because only one sensor is used, $\bar{\Sigma}_{z_t}$ is a 1×1 matrix. As $\bar{\Sigma}_{z_t}$ is reduced, $|\bar{\Sigma}_{x_t,z_t}\bar{\Sigma}_{z_t}^{-1}\bar{\Sigma}_{x_t,z_t}^{T}|$ will increase if $\bar{\Sigma}_{x_t,z_t}$ is constant. To simplify the analysis, some of the sigma-point filter variables are redefined below. Equation 4.51 is from the measurement

Table 4.6: Minimization proposition

Proposition: Assuming $A \geq 0$, $B \geq 0$, $A - B \geq 0$, A is invertible and constant, and B is $n \times n$, the following is true.

$$\underset{B}{\operatorname{argmin}} |A - B| = \underset{B}{\operatorname{argmax}} |B|$$

Proof: Define λ_i as the ith eigenvalue of the matrix $A^{-\frac{1}{2}} B A^{-\frac{1}{2}}$.

$$\begin{aligned}
& \underset{B}{\operatorname{argmin}} |A - B| \\
= \; & \underset{B}{\operatorname{argmin}} \log |A - B| \\
= \; & \underset{B}{\operatorname{argmin}} \log |A^{\frac{1}{2}} (I - A^{-\frac{1}{2}} B A^{-\frac{1}{2}}) A^{\frac{1}{2}}| \\
= \; & \underset{B}{\operatorname{argmin}} (\log |A| + \log |(I - A^{-\frac{1}{2}} B A^{-\frac{1}{2}})|) \\
= \; & \underset{B}{\operatorname{argmin}} \log |(I - A^{-\frac{1}{2}} B A^{-\frac{1}{2}})| \\
= \; & \underset{B}{\operatorname{argmin}} \log \prod_{i=1}^{n} (1 - \lambda_i) \\
= \; & \underset{B}{\operatorname{argmin}} \sum_{i=1}^{n} (1 - \lambda_i) \\
= \; & \underset{B}{\operatorname{argmax}} \sum_{i=1}^{n} \lambda_i \\
= \; & \underset{B}{\operatorname{argmax}} \log |A^{-\frac{1}{2}} B A^{-\frac{1}{2}}| \\
= \; & \underset{B}{\operatorname{argmax}} (\log |A^{-1}| + \log |B|) \\
= \; & \underset{B}{\operatorname{argmax}} |B|
\end{aligned}$$

update step in the SPKF.

$$\begin{pmatrix} \Sigma_{sc}^1 & \Sigma_{sc}^i & \dots & \Sigma_{sc}^n \end{pmatrix} = \gamma\sqrt{\bar{\Sigma}_{x_t}} \tag{4.48}$$

$$h_+^i = h(\bar{x}_t + \Sigma_{sc}^i, \theta_t) \tag{4.49}$$

$$h_-^i = h(\bar{x}_t - \Sigma_{sc}^i, \theta_t) \tag{4.50}$$

$$\begin{aligned} \bar{\Sigma}_{z_t} &= \omega_c^0(\hat{z}_t - h(\bar{x}_t, \theta_t))^2 + \sum_{i=1}^{n} \omega_c^i(\hat{z}_t - h_+^i)^2 \dots \\ &\quad + \sum_{i=1}^{n} \omega_c^i(\hat{z}_t - h_-^i)^2 + \Sigma_{\delta_t} \end{aligned} \tag{4.51}$$

The first term of Equation 4.51 is zero if the measurement function is linear or follows relationship B from 4.5 because $\hat{z}_t$ will become $h(\bar{x}_t, \theta_t)$. The last term is always constant. Separating out corresponding $\pm i$ terms, the equations below will show that the two summation terms are minimized with a linear measurement function.

$$\begin{aligned} 0 &= \frac{d}{d\hat{z}_t}((\hat{z}_t - h_+^i)^2 + (\hat{z}_t - h_-^i)^2) \\ &= \frac{d}{d\hat{z}_t}(2\hat{z}_t^2 + (h_+^i)^2 + (h_-^i)^2 - 2\hat{z}_t h_+^i - 2\hat{z}_t h_-^i) \\ &= 4\hat{z}_t - 2h_+^i - 2h_-^i \\ \hat{z}_t &= 0.5(h_+^i + h_-^i) \end{aligned} \tag{4.52}$$

$$\frac{d^2}{d\hat{z}_t^2}((\hat{z}_t - h_+^i)^2 + (\hat{z}_t - h_-^i)^2) = 4 > 0 \tag{4.53}$$

This analysis has shown that the SPKF cost metric is influenced by the linearity or anti-symmetry of the measurement equation through $\bar{\Sigma}_{z_t}$. When the sensor equation meets those conditions and $\bar{\Sigma}_{x_t,z_t}$ is constant, $\bar{\Sigma}_{z_t}$ is minimized and therefore $|\Sigma_{x_t}|$ is also minimized.

4.5 Trajectory Generation

Equation 4.54 summarizes the optimization that incorporates the above sections and produces a locally optimal trajectory. The trajectory is suboptimal because the function is non-convex and so global optimality is not guaranteed. In order to constrain the trajectory of the vehicle, the optimization is actually performed over all the commands, U_m, which moves the sensor from θ_{m-1} to θ_m through an update function, $f()$. The m is used instead of t only to indicate that each measurement does not have to be taken at equal time intervals. The estimator function, $e()$, propagates the estimates given the predicted measurement. It is there because the mean changes when using a SPKF based estimator due to the bias issues discussed in Section 4.3.3. MATLAB's `fmincon` function was used to solve the optimization with a sequential quadratic programming [59].

$$
\begin{aligned}
\underset{u_1,\ldots,u_M}{\text{minimize}} \quad & J(\theta_{r,0}, x_{\text{UXO},0}, \Sigma_{x_{\text{UXO},0}}) \\
\text{subject to} \quad & \theta_{r,m} = f(\theta_{r,m-1}, u_m) \\
& \{x'_{\text{UXO},0}, \Sigma'_{x_{\text{UXO},0}}\} = \{x_{\text{UXO},0}, \Sigma_{x_{\text{UXO},0}}\} \\
& z'_m = h(x_{\text{UXO},m}, \theta_{r,m}) \\
& \{x'_{\text{UXO},m}, \Sigma'_{x_{\text{UXO},m}}\} = e(z'_m, x'_{\text{UXO},m-1}, \Sigma'_{x_{\text{UXO},m-1}}) \\
& J = |\Sigma'_{x_{\text{UXO},M}}| \\
& u_{\text{min}} \leq u_m \leq u_{\text{max}}
\end{aligned}
\tag{4.54}
$$

Chapter 5

Adaptive Sensing with an Electromagnetic Induction Sensor

THE LAST CHAPTER presented the general adaptive sensing framework. This chapter adapts the method for unexploded ordnance, UXO, discrimination using an electromagnetic induction, EMI, sensor. An eigenvector sigma-point Kalman filter, eSPKF, is used to formulate the cost of every sensor action. Simulation results will show that adaptive sensing, which determines where to move and orient the sensor, has improved discrimination ability over the previously mentioned lawnmower search. They will also show that the ability to orient the sensor is important for adaptive sensing. An odometry based positioning system is assumed here.

5.1 New Framework

Figure 5.1 shows the adaptive sensing block diagram for UXO discrimination. It incorporates the EMI sensor into the sensor block, the eSPKF for estimation, and $|\Sigma_x|$ as the cost function. The two differences for the new framework are the look ahead window and the estimator block incorporating a target library.

The look ahead window is reduced to one which is a greedy search, $M = 1$. This means the adaptive sensing algorithm will only consider the next time step when trying to to move and orient the sensor. The drawback for this strategy is that the search cannot go through

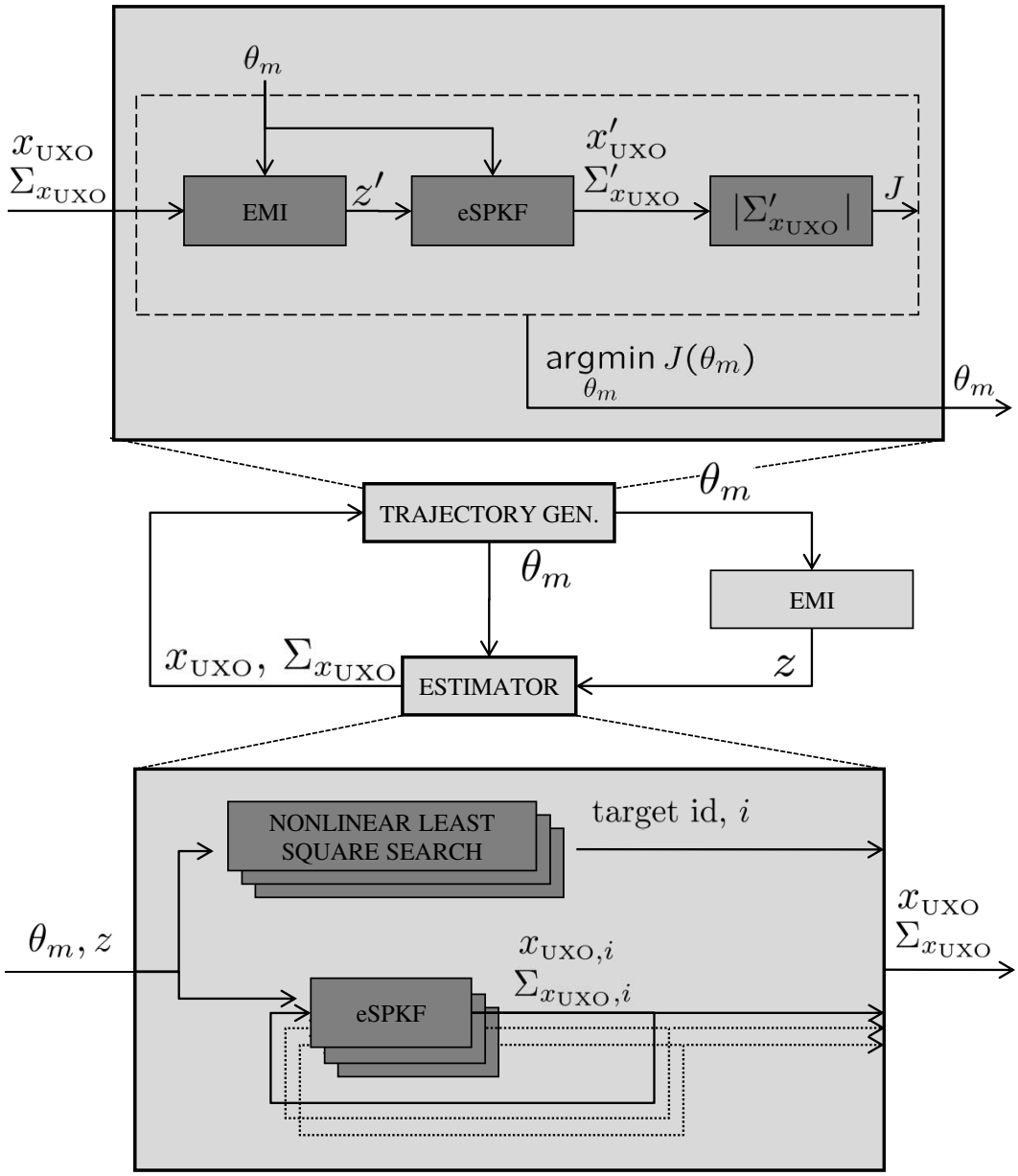

Figure 5.1: EMI adaptive sensing block diagram

This block diagram incorporates the estimator and cost function results from Chapter 4 into the general adaptive sensing framework. The bottom portion shows how the estimator handles a target library.

areas of low information to reach an area of high information [28]. This search space is also not convex so the solution found is not guaranteed to be optimal. Section 4.5 discusses the optimization routine used. To increase the chance of minimizing cost, the search routine is initialized with several different potential sensor locations and orientations. The resulting sensor action that has the minimum cost over the set of searches is used to decide what the sensor will do next.

The second change allows the estimator to handle a library of targets. This approach was originally taken from the fault detection field where a bank of filters is used to detect faults. All are run simultaneously, with each filter examining a different possible fault [104, 109]. In this case, a separate filter is run for each target in the library. This incorporates the knowledge represented in the library by using the target's dipole parameters. Mathematically, it reduces the state space being estimated in each filter and allows the filter to concentrate on estimating the target's location and orientation.

$$x_{\text{UXO}} = \begin{bmatrix} \vec{r} \\ \theta \\ \phi \end{bmatrix}_{5\times 1} \tag{5.1}$$

The trajectory generation block currently requires a single estimate to be passed to it. The possible estimates range from the best fit target to a combination of all possible target estimates. The best fit target is used because as more measurements are gathered and the estimate uncertainty decreases, the adaptive sensing will focus on that specific target. The nonlinear least squares optimization from Equation 2.10 is used to determine which target estimate is chosen. The minimization is seeded with the estimate mean. The estimate mean is not used directly to calculate goodness of fit because Section 4.3.3 says the mean will be biased especially when the uncertainty is large. A minimization search will force the result to be the best possible fit given the current measurements. The estimator's mean and uncertainty of the best fit object is then used to generate a new trajectory. That estimate does a better job of representing the distribution of the estimate despite the mean being biased.

There are two possible outputs of the trajectory generation block. For most of this

chapter, the output will be a 4×1 vector representing the location and orientation of the sensor. The height of the sensor is assumed to be fixed by its location on the vehicle. At the end of the chapter, the adaptive sensing algorithm will produce a 2×1 vector that is only the sensor location. This later investigation looks at the affect on the discrimination process from fixing sensor orientation.

$$\theta_{\text{EMI}} = \begin{bmatrix} \vec{r} \\ \theta \\ \phi \end{bmatrix}_{4\times 1} \quad \text{or} \quad \theta_{\text{EMI}} = \begin{bmatrix} \vec{r} \end{bmatrix}_{2\times 1} \tag{5.2}$$

Figures 5.2 and 5.3 show plots at different times for a grid traverse and an adaptive sensing trajectory. In the beginning, both estimators start off thinking the target is a rod located at the origin. As they take more measurements, each estimator will change what it thinks the target is. This strength of the bank of filters is that even though the target identification is wrong, the information is not lost. The filter for each target is continuously running and incorporating new measurements. When the estimator switches suspected targets, the mean and estimate used to determine the new trajectory contains all the information from previous measurements. In Figure 5.2, the estimator initially thinks the target is a rod and then switches between an UXO and a plate before finally deciding on an UXO.

The adaptive sensing algorithm shown in Figure 5.3 uses the simple motion constraints implemented in Equation 4.54. More complicated constraints can be used.

After the last sensor reading, the same minimization routine is run again to determine which target fits the set of measurements better. The search is initialized with each potential object's posterior estimate. This is done for two reasons. First, as mentioned before there is a bias in the estimator so this search routine will eliminate that bias. Second, the estimate was based on a Kalman estimator with a Gaussian assumption. There is no guarantee that the states being propagated follow the Gaussian assumption. This last search allows the final discriminatory metric not to be biased by that assumption.

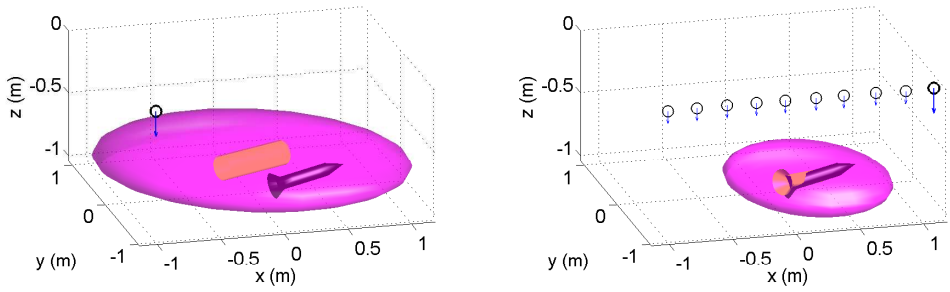

(a) $m = 1$ (b) $m = 10$

(c) $m = 20$ (d) $m = 30$

(e) $m = 40$ (f) $m = 50$

Figure 5.2: Grid trajectory

The vehicle is driven in a small lawnmower pattern centered at the initial estimate of the target's location. Several time steps are plotted along with the estimate of the target type, location, orientation, and uncertainty. The initial guess of the target is that it is a rod and located at the origin. At the 20th measurement, the estimator briefly thought the target was a plate.

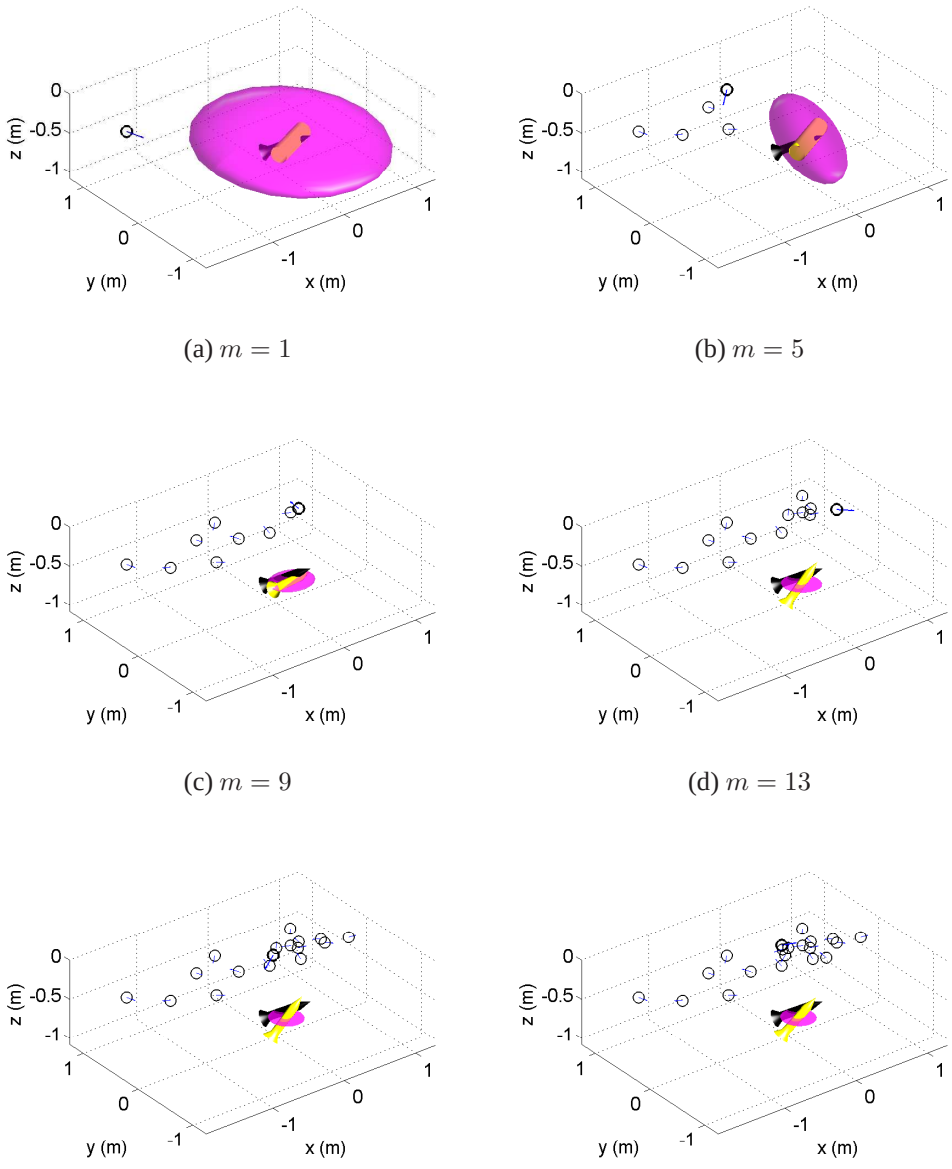

(a) $m = 1$ (b) $m = 5$

(c) $m = 9$ (d) $m = 13$

(e) $m = 17$ (f) $m = 20$

Figure 5.3: Adaptive sensing trajectory

The sensor is moved and oriented according to the adaptive sensing algorithm. Initially, the target was thought to be a rod located at the origin. After about 9 measurements, the target is thought to be an UXO.*The sensor positions are clustered around the actual target reducing the chance of picking up stray sensor readings from another target.*

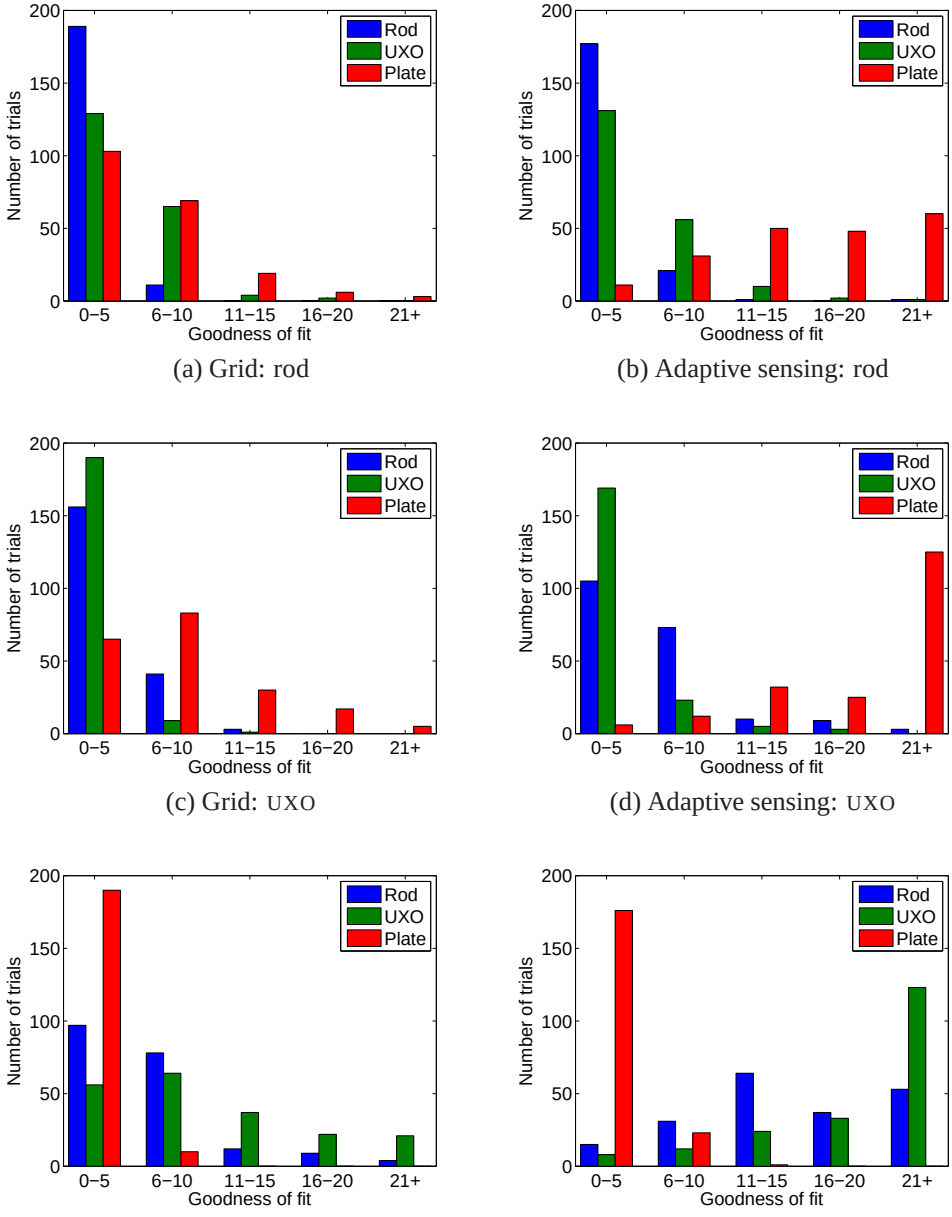

(a) Grid: rod

(b) Adaptive sensing: rod

(c) Grid: UXO

(d) Adaptive sensing: UXO

(e) Grid: plate

(f) Adaptive sensing: plate

Figure 5.4: Goodness of fit histograms

Each figure represents 200 simulated runs with sensor noise and position noise. Each row consolidates runs where the object buried is identical. The right column uses the adaptive sensing algorithm. The left column reprints the grid plots from Figure 3.10 for comparison.

5.2 Simulation

These simulations are similar to what is run in Section 3.2.1. Two hundred trials are done for each buried object executing an adaptive sensing trajectory. Noise is included for the EMI measurements and the odometry positioning errors. The target's actual location and orientation is randomly changed for each run. At the end of each traverse, a goodness of fit metric is calculated for each object in the library given the measurements taken and their corresponding sensor states.

Figure 5.4 plots the new goodness of fit histograms running the adaptive sensing algorithm. The left column reprints the histograms describing the grid search. Like the grid search, the adaptive sensing approach does a good job of having good fits for the correct items. The difference lies in how well the algorithm distinguishes between objects that are dissimilar. For the UXO situation, Figure 5.4d has the plate fits severely weakened as over a hundred of the trial runs resulted in goodness of fits of over 20. In the same plot, the rod still exhibits a strong fit for the data. They same trend is seen in the rod data set. The rod and UXO models both exhibit strong fits for each of the runs, but the plate model is diminished. This is reasonable because both the rod and UXO are similarly sized long axially symmetric objects and so the fits should not be far off.

Figure 5.5 summarizes the discrimination results from the previous lawnmower patterns using GPS and odometry along with two adaptive sensing operational modes. The first mode allows the sensor to rotate, the second does not. The receiver operating curve, ROC, curve shows that the adaptive sensing algorithm that can change orientation is better than the grid approach using GPS. However, it does not seem to be better than the grid approach using odometry. The ROC curve was generated only using the UXO goodness of fit. The next plot looks at all the fits. It identifies the target based on which model fits the data best. In that situation, the adaptive sensing has the best identification rate using only 20 measurements. After that, the discrimination ability deteriorates possibility due to the build up of odometry error. Section 3.1 points out how relative and absolute accuracy impact discrimination, and it shows why a grid pattern is particularly adept at retaining relative positioning accuracy. Adaptive sensing does not leverage relative accuracy.

In the same plots, it is clear that the adaptive sensing with fixed orientation does poorly.

The ability to change the orientation of the sensor allows the algorithm to gather unique information that the fixed orientation approaches cannot. The lawnmower pattern already forces the sensor to fully sample the space of fixed orientation measurements.

The histograms for the adaptive sensing trials shows a divergence in fit quality between the two long axially symmetric objects and the plate. Figure 5.6 looks at how well each trajectory identifies the two types of objects. The adaptive sensing outperforms the other options when its orientation is allowed to change.

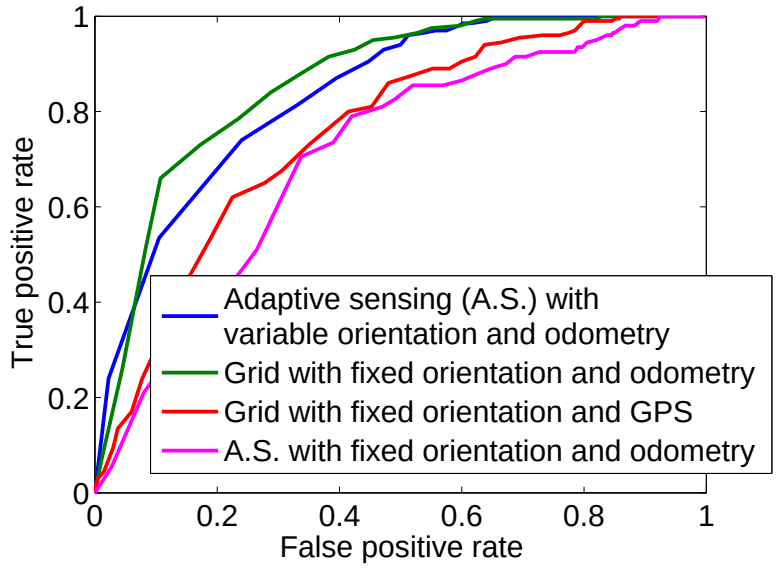

(a) Receiver operating curve

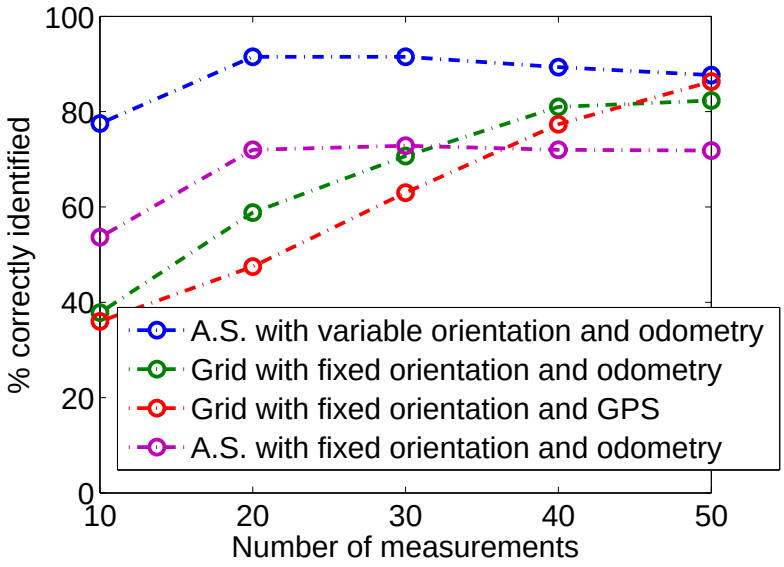

(b) Discrimination accuracy

Figure 5.5: Comparison between trajectories

These plots summarize the discrimination results from the histograms in Figure 5.4. It also includes the GPS *lawnmower trials and the adaptive sensing with fixed orientation trials. (a) The top plot only looks at the goodness of fit metrics from the* UXO *model. (b) The bottom plot discriminates based on which model has the best goodness of fit.*

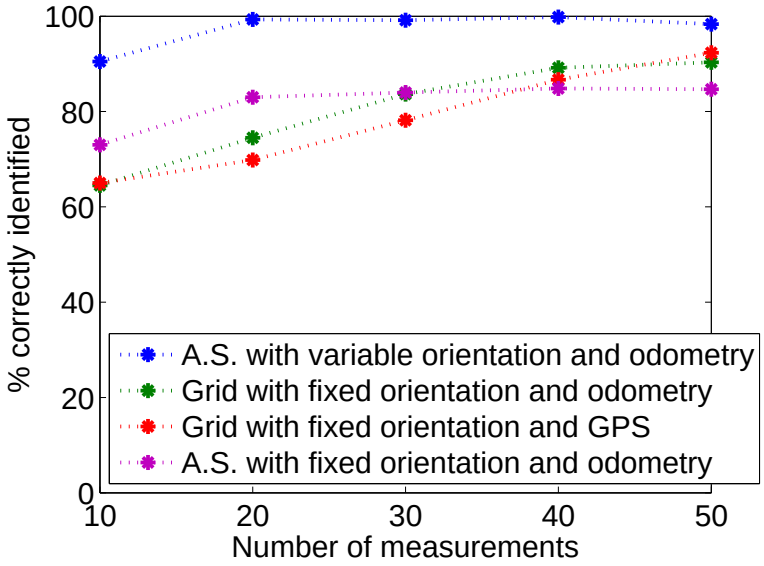

Figure 5.6: Accuracy of identifying long symmetric objects vs. plates

The histograms in Figure 5.4 show that adaptive sensing is particularly adept at separating the long axially symmetric objects from the plate. This plot looks into how well each traverse technique fares in that task.

Chapter 6

Conclusions

THE UNEXPLODED ORDNANCE, UXO, community has spent a large amount of time, energy, and money trying to solve the UXO discrimination problem. The traditional method is to completely cover a field with GPS tagged sensor readings, post process the data, and then excavate from the resulting dig list. This thesis motives two alternate strategies that allow for better UXO discrimination and eliminate the need for an external positioning sensor. The first option is to use an odometry based positioning system with a localized lawnmower pattern. The second option also uses odometry, but this time does an adaptive search of the area.

There are four assumptions made for this research. First, *an* EMI *sensor is used*. Both MAGs and GPRs were considered, but they do not provide the discriminatory abilities of the EMI sensor.

Second, *a target library exists of potential objects in the field*. The library contains the dipole response parameters for each of the objects. This data can be initialized with foreknowledge of objects in the field and then augmented when new items are uncovered.

Third, the sensing platform *has prior knowledge that something is in the area*. This can come from a map of potential targets generated from a previous field wide traverse. It can also be a vehicle currently performing a field wide traverse, detecting something interesting, and deciding to immediately investigate.

The last assumption is that each of the focused searches only has *one target in the area*. This is a reasonable assumption for several reasons. The EMI signal dies off at a rate

inversely proportional to the distance to the sixth power. Thus, only targets that are very close together will have overlapping sensor readings. The adaptive sensing also focuses its search close to the target further decreasing the chance of interfering targets. While there is no way to guarantee that there is always only one target in view, the future work section will discuss several ways of relaxing this constraint.

6.1 Summary of Contributions

This dissertation concentrates on focused investigations of a target to improve discrimination. Two recommendations are made to the UXO community. The first recommendation is to use the sensor with the best relative accuracy in a small lawnmower pattern. An odometry system is built into the sensing platform so no external positioning infrastructure needs to be deployed. This differs from differential GPS systems, robotic total stations, and other external based positioning systems which are can be affected by line of sight obstructions and the distance away from a base station. The second recommendation assumes a vehicle is carrying the sensor and can rotate it. The vehicle can now perform an adaptive trajectory that tries to maximize its information about the target.

These recommendations were developed as a result of three main contributions.

Designed and implemented a local odometry based search to compete with an existing GPS-based search for UXO discrimination.

Current discrimination strategies call for a complete coverage of a field with a GPS equipped sensor. A lawnmower pattern is typically used as the most efficient way to cover an open field. The GPS positioning error is independent of the vehicle's trajectory because measurement error from time step to time step is assumed to be independent. There are correlated error sources with GPS such as multi-path, but they are not dealt with here.

Chapter 3 starts off looking at the affects of relative error and absolute error on UXO discrimination. If the goal is to come up with a set of dipole parameters that best fit the data, then relative error is more important. Fitting data to an EMI model requires the location and orientation of each measurement relative to each other to be known. The resulting set of

position states could be biased. The extreme example is a set of data that is shifted several feet east. The parameters found with those sensor measurements will fit the data well, but the target location will be shifted the same distance.

Odometry inherently is a relative sensor. For large field wide traverses, the positioning error will continue to grow as the vehicle travels further and further. The error is much more manageable for a small focused search. Additionally, a lawnmower pattern is more conducive to an odometry system because of the way it reduces relative error. Several other trajectories were tried and did not exhibit the same properties.

Simulations were run comparing the effects on UXO discrimination from GPS with a 5 cm error versus an odometry system using 5% distance traveled as error. The goodness of fit metrics and ROC show that an odometry system is an improvement over the GPS system.

Finally, that chapter looked at the effects of having an improved positioning system and having an improved knowledge of the target's location. Not surprisingly, in both cases there is a significant improvement in discrimination.

Developed an algorithm that adapts a sensor trajectory to seek information for geophysical sensors tuned for UXO investigations.

An adaptive sensing framework is developed that is *fast* and can handle *highly nonlinear sensor functions* with *large state vectors*. Chapter 4 begins with a block diagram of the algorithm. An estimate containing a mean and a covariance represents the target parameters. The estimator takes a set of measurements and the sensor states and produces an estimate of the target. A trajectory generation block then decides where to move and rotate the sensor to maximize information. Finally, the sensor is moved to achieve the desired state, and a measurement is taken. A new estimate is calculated and the process is repeated.

The target generation block also has several components. A predicted sensor measurement is determined from the current best target estimate and a potential sensor state. The predicted measurement goes into an estimator that predicts the posterior estimate. The process is repeated until the entire trajectory is flown. A scalar cost is calculated from the final uncertainty. The trajectory that produces the minimum cost is the trajectory chosen.

A range sensor is used to give insight into each of the components. Several estimators

and information metrics are discussed before settling on the square root eigenvector sigma-point Kalman filter, eSPKF, and the determinant of the covariance matrix. The particle filter is a good nonlinear estimator, but it does not scale well with large state vectors. The extended Kalman filter can handle a large number of states, but it does not handle highly nonlinear sensor functions and it ignores prior uncertainties. The sigma-point Kalman filter allows for nonlinearities without suffering the scaling problem. The eigenvector version of it forces the sigma-points to align themselves along the eigenvector allowing the estimator to be rotationally invariant. The example in Section 4.4.3 shows that the sigma-points can affect the estimator due to how their locations are calculated and not from the sensor model. Finally, several forms of information are discussed. They are all related given a Gaussian assumption.

Adapted and validated adaptive sensing for UXO discrimination with an EMI sensor.

The adaptive sensing algorithm is modified to handle a target library. Borrowing from the fault detection field, a bank of filters is used to maintain an active estimate of the states for each object in the library. The target that best matches the current set of sensor readings has its estimate sent to the trajectory generation block. This allows the adaptive sensing to be performed, but not lose any information if the guess is wrong. After the final measurement, a goodness of fit is calculated for every object after running an optimization to fit the sensor data to the sensor models. This eliminates the Gaussian assumption built into the estimator and the inherent bias in the eSPKF. Simulations are run that show the adaptive sensing algorithm will improve UXO discrimination if the EMI sensor is allowed to rotate.

6.2 Future Work

6.2.1 UXO

There are many roads that can be taken to help improve UXO discrimination. The direct path from this research leads to more field test, construction of a sensor platform, and applying more advanced discrimination techniques. This odometry enabled platform allows the sensor to be used in the focused lawnmower search or for adaptive sensing. Autonomy

can be built into the platform, or have a separate system tell the human user where and how to move the vehicle. Afterwards, field trials at actual UXO sites should be run to characterize the information gathering ability of the methodology. The discrimination technique used in the thesis is purely based on goodness of fit. The added information should also continue to improve discrimination when more advanced machine learning techniques are applied.

A single target in view is assumed by this thesis. Fusing a GPR into the sensor suite can help eliminate that assumption. A GPR will be able to identify different objects in the immediate vicinity and help localize them. It can even help with the target shape [85]. An eSPKF based algorithm is well suited to handle the large state vector required to handle multiple objects.

Adaptive sensing also allows the fusion of other geophysical sensors or positioning sensors. The new geophysical sensors could add new parameters to the discrimination process or help better locate the target. There is the possibility of splitting the transmit and receive coils up. Maybe there is information lost by co-locating the coils. The positioning sensors can provide better sensor locations by incorporating location uncertainty and even using a simultaneous localization and mapping algorithm, SLAM. They could also be used to factor in relative accuracy.

The EMI sensor models used in this work were based on a single time-gated reading from a specific sensor. There are other sensors that can examine the decay rates of a signal, use different sensor models, or present measurements in the frequency domain. As better sensor models and sensors are developed, adaptive sensing can be applied to any of those situations.

The EM61-MK2 returns a scalar measurement of a component of the local magnetic field. Adaptive sensing uses a sensor's ability to move and rotate to quickly understand the entire vector magnetic field. If a sensor can instantaneously measure the direction and strength of the local magnetic vector, then the entire magnetic field can also be quickly determined. There are researchers designing systems to do that with several co-located transmit and receive coils. This is a field of research that has a large potential for improving UXO work, and it would be interesting to see the effect adaptive sensing has with such a sensor.

6.2.2 Adaptive Sensing

There are also many directions for future work outside the UXO field. There are situations that require a set of parameters to be identified as quickly as possible. This can come from a military requirement for locating an enemy quickly and stealthily or a scientific requirement for conserving power. Two potential targets are a RF source such as a enemy transmission or an avalanche rescue beacon [37]. Adaptive sensing allows the user to vary certain sensor states to accomplish that. This can be the actual position and orientation of the sensor, the type of sensor, or even the specific sensor settings.

Given a specific set of sensor models and target states, the cost metric and estimators presented here can also optimize the configuration of a suite of sensors. The only difference is that in adaptive sensing, the optimization occurs over several time steps. When optimizing a sensor suite, the algorithm decides which sensors to include and how to configure them.

In some situations, multiple vehicles are used for parameter estimation and so a decentralized adaptive sensing algorithm can be used. A common technique uses the extended information filter, EIF, to efficiently transfer information between vehicles. The current information forms of the SPKF do not exhibit the simplification of the covariance update step that allows the EIF to be used in this manner [54, 97, 102].

6.3 Concluding Remarks

A large amount of the current UXO research is focused on the sensor technology and the post processing algorithms which include sensor models and machine learning. The goal of this thesis was to investigate unexplored paths that bridge the two areas. Is there a way to use current sensor technology more efficiently? This thesis argues that the answer is yes and it details some of those methods.

Appendix A

Abbreviations & Acronyms

AUV	Autonomous Underwater Vehicle
EIF	Extended Information Filter
EKF	Extended Kalman Filter
EMI	Electromagnetic Induction
eSPKF	Eigenvector Sigma-Point Kalman Filter
GPR	Ground Penetrating Radar
GPS	Global Positioning System
IED	Improvised Explosive Device
MAG	Magnetometer
MTADS	Multi-Sensor Towed Array Detection System
PF	Particle Filter
ROC	Receiver Operating Curve
RF	Radio Frequency
SLAM	Simultaneous Localization and Mapping
SPIF	Sigma-Point Information Filter
SPKF	Sigma-Point Kalman Filter
UAV	Unmanned Aerial Vehicle
US	United States
UXO	Unexploded Ordnance

Appendix B

Localization with a Total-Field Magnetometer

TOTAL-FIELD MAGNETOMETER, MAG, is another sensor commonly used in the unexploded ordnance, UXO, field. This chapter applies the adaptive sensing algorithm with a MAG to UXO localization and not to UXO discrimination. Field tests were performed to validate the sensor models and simulations were run that show adaptive sensing improves localization.

The MAG measures the magnitude of the component of a magnetic field aligned with Earth's magnetic field [16]. Figure B.1a shows the static magnetic field, $\vec{B}$, produced by the UXO and it shows Earth's magnetic field, $\vec{B}_e$. The UXO's magnetic field is assumed to be a dipole that results from remnant and induced magnetization. Remnant magnetization is the permanent magnetization of the object and induced magnetization is the object's response to being placed in an ambient magnetic field. In Equation B.1, $\vec{r}$ and $\vec{R}$ represent the location of the sensor and the UXO respectively. This is the same equation as the dipole equation presented in Chapter 2. $\hat{B}_e$ is a unit vector that is pointed in the same direction as Earth's magnetic field [10, 15, 107]. The target state vector is a combination of the UXO's location and its dipole vector, $x_t^m = [\vec{R}^T, \vec{m}^T]^T$. The sensor states consist of the magnetometer's location, $\theta_t^m = \vec{r}_t \in \Re^{3\times 1}$.

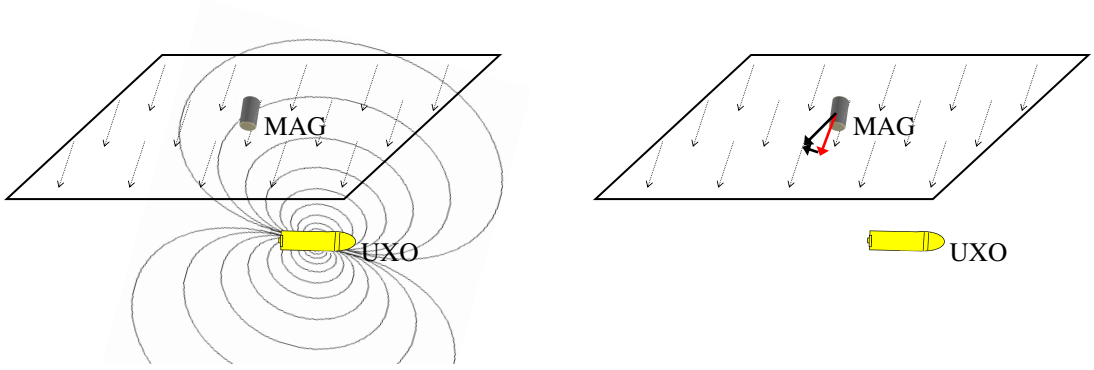

(a) Primary magnetic field (b) Measurement

Figure B.1: Description of MAG physics

These images depict the interactions between a MAG *sensor and an* UXO*. The target possesses a static magnetic field. The sensor detects the component of that magnetic field aligned with Earth's magnetic field.*

$$\vec{B}(\vec{r}) = \frac{\mu_0}{4\pi}(3[\vec{m}\cdot(\vec{r}-\vec{R})]\frac{(\vec{r}-\vec{R})}{\parallel \vec{r}-\vec{R} \parallel_2^5} - \frac{\vec{m}}{\parallel \vec{r}-\vec{R} \parallel_2^3}) \tag{B.1}$$

$$z_t = \hat{B}_e \cdot \vec{B}(\vec{r}) \tag{B.2}$$

In this thesis, a MAG will be used for detection and not discrimination because many non-UXO ferrous objects can also be treated as a magnetic dipole. Billings proposes that on impact, an UXO will lose its remnant magnetization leaving the induced magnetization to be the sole source of the detected magnetic field. This field's direction will be close to Earth's magnetic field. However, due to ambiguities between an object's shape, size, and dipole moment, actual classification is still difficult [12]. Zhang et al. uses parameters from a MAG to feed the electromagnetic induction, EMI, based discrimination algorithms [107].

B.1 Sensor

The Geometrics G-858 MagMapper was used in field tests to validate the dipole model. From its data sheet, this total-field MAG "is based on a self-oscillating split-beam Cesium Vapor." It can operate in a field between 20,000 and 100,000 nT and has an accuracy of

(a) Geometrics G-858 MagMapper

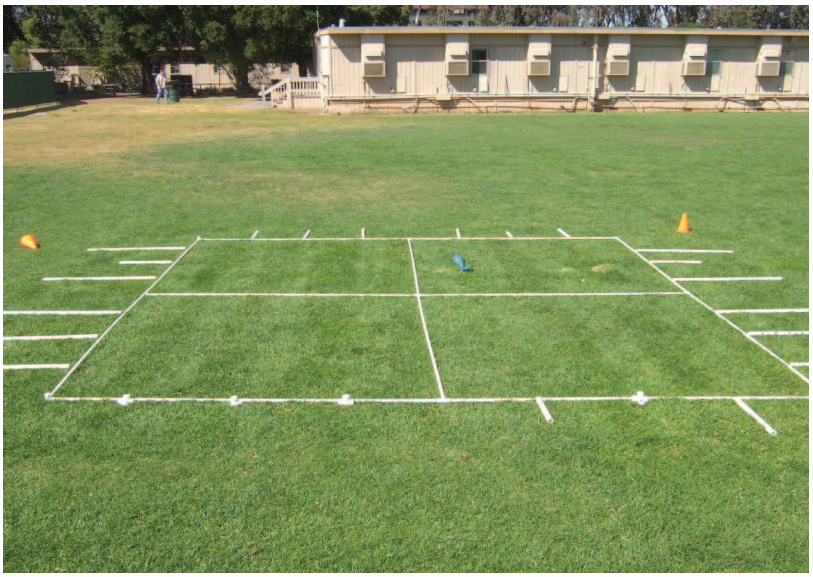

(b) Field test

Figure B.2: MAG hardware testing

This total-field MAG *was generously loaned by Geometrics for this research* [a]. *It was used to validate the* MAG *models by taking gridded data on a test field marked off by pvc pipes. Figure 2.1b is showing this sensor in use.*

[a] Image is courtesy of http://www.geoafrica.co.za/reddog/geometrics/magnetometer_g858.htm.

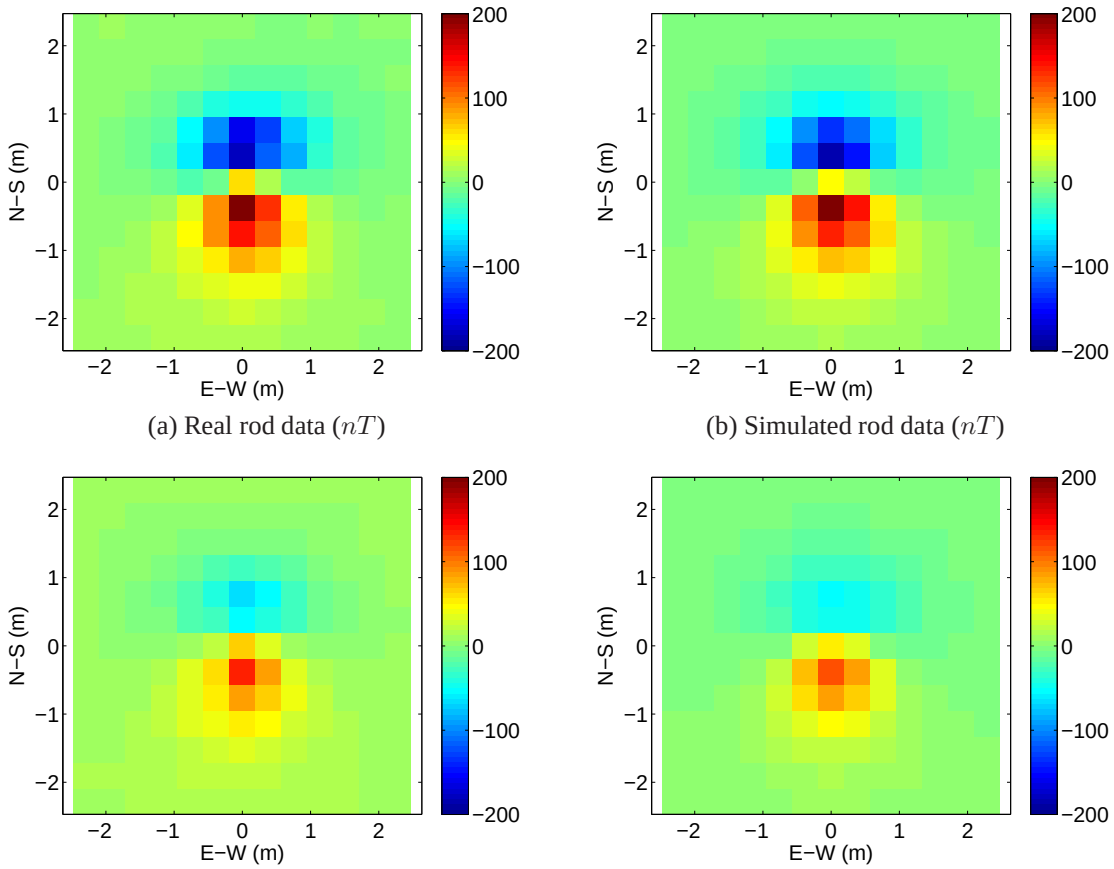

(a) Real rod data (nT)

(b) Simulated rod data (nT)

(c) Real UXO data (nT)

(d) Simulated UXO data (nT)

Figure B.3: Real vs. simulated measurements

Several sets of data were gathered with each object. The measurements were taken at discrete locations and a contour map was generated. The left column shows a single set of measurements for a rod and an UXO*. The background magnetic field is subtracted out. The right column shows corresponding simulated data based on the sensor models. The parameters of each target were obtained by fitting the sensor model to the data.*

less than 2 nT. [31, 91]

The sensor was taken into the field to measure the same objects, pictured in Figure 2.6, used for the EMI tests. Each object was placed on the ground in the center of a 4.5m $\times$ 4.5m area shown in Figure B.2b. The sensor was always oriented north because of its sensitivity to heading. In each data set, 169 measurements were taken with 38cm spacing between readings.

A rod and an UXO data sets are plotted in Figure B.3. The axes show the 2D location of the sensor and the color corresponds with the sensor reading in nT. The left column of the plots is the real readings while the right column is simulated readings from a best fit parameter set. The background noise was measured first and subsequently subtracted out of future readings. A plate data has the same shape and is not shown. For reference, a MRI or a loudspeaker magnet is several T's in strength, a refrigerator magnet is several mT's, and Earth's magnetic field is between 30μT and 60 μT.

B.2 Adaptive Sensing

The adaptive sensing used here is the same approach as described in Chapter 5 without a target library. Adaptive sensing is trying to decide where to place the sensor in x and y and is assuming that the sensor height is fixed. There is no effect from sensor orientation incorporated in this example, which is akin to having the sensor constantly facing the same heading. The parameter estimation is estimating the target dipole's location, orientation, and magnitude.

A run of 50 measurements arranged in a grid pattern was compared to 50 measurements taken at locations prescribed by adaptive sensing. An example of each pattern is shown in Figures B.4 and B.5. The initial guess of each estimator was that the target was located at the origin. There was no sensor position noise, but there was measurement noise. The location, orientation, and strength of the magnetic dipole was changed for every simulated run. The figures only show the target estimate and its uncertainty in 2D, but all six states are being estimated.

Table B.1 summarizes the localization results from 200 runs. The initial error is because the initial guess is the origin of the plot while the actual target is located somewhere else.

Table B.1: Simulation results of 200 Runs with MAG

	Initial	Grid	Adaptive Sensing
Localization Error (m)	0.62	0.24	0.18

The grid approach does improve on that accuracy, but the adaptive sensing improves it even more.

Adaptive sensing was used on one of the data sets from the field tests. The measurements were originally taken in a grid pattern. The best discrete location from the set of sensor positions was used as the next sensor position. Once that measurement had been used, the sensor cannot return to that location. Figures B.6 and B.7 show four time steps and the resulting estimation of the target's location and its uncertainty. The dipole vector is also being estimated, but is not being displayed.

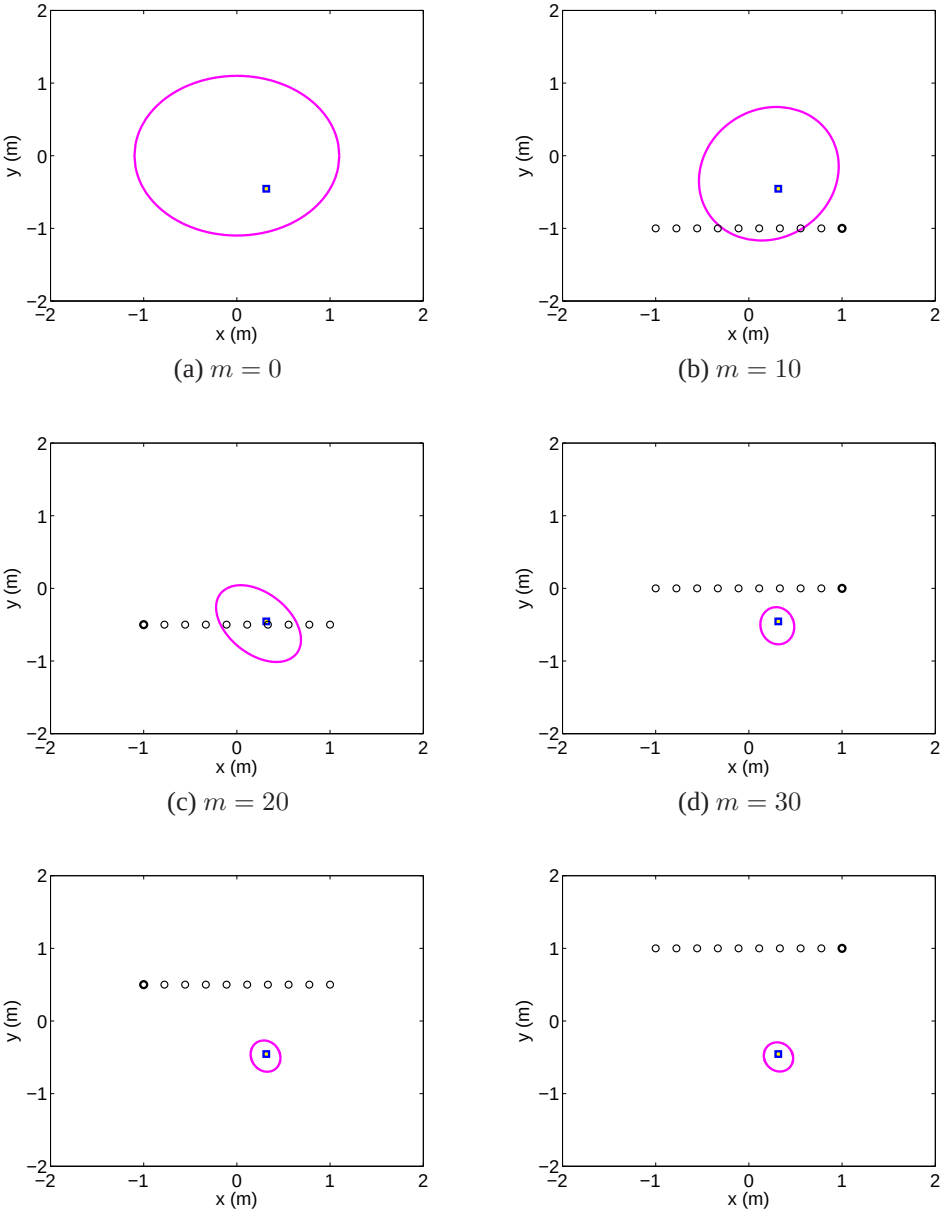

(a) $m = 0$ (b) $m = 10$

(c) $m = 20$ (d) $m = 30$

(e) $m = 40$ (f) $m = 50$

Figure B.4: Lawnmower trajectory

The MAG *equipped vehicle is driven in a small lawnmower pattern around the suspected target location. Each plot shows the last 10 measurement locations with the most recent measurement emphasized. The actual target is the yellow box and the estimate mean is the center of the magenta uncertainty ellipse.*

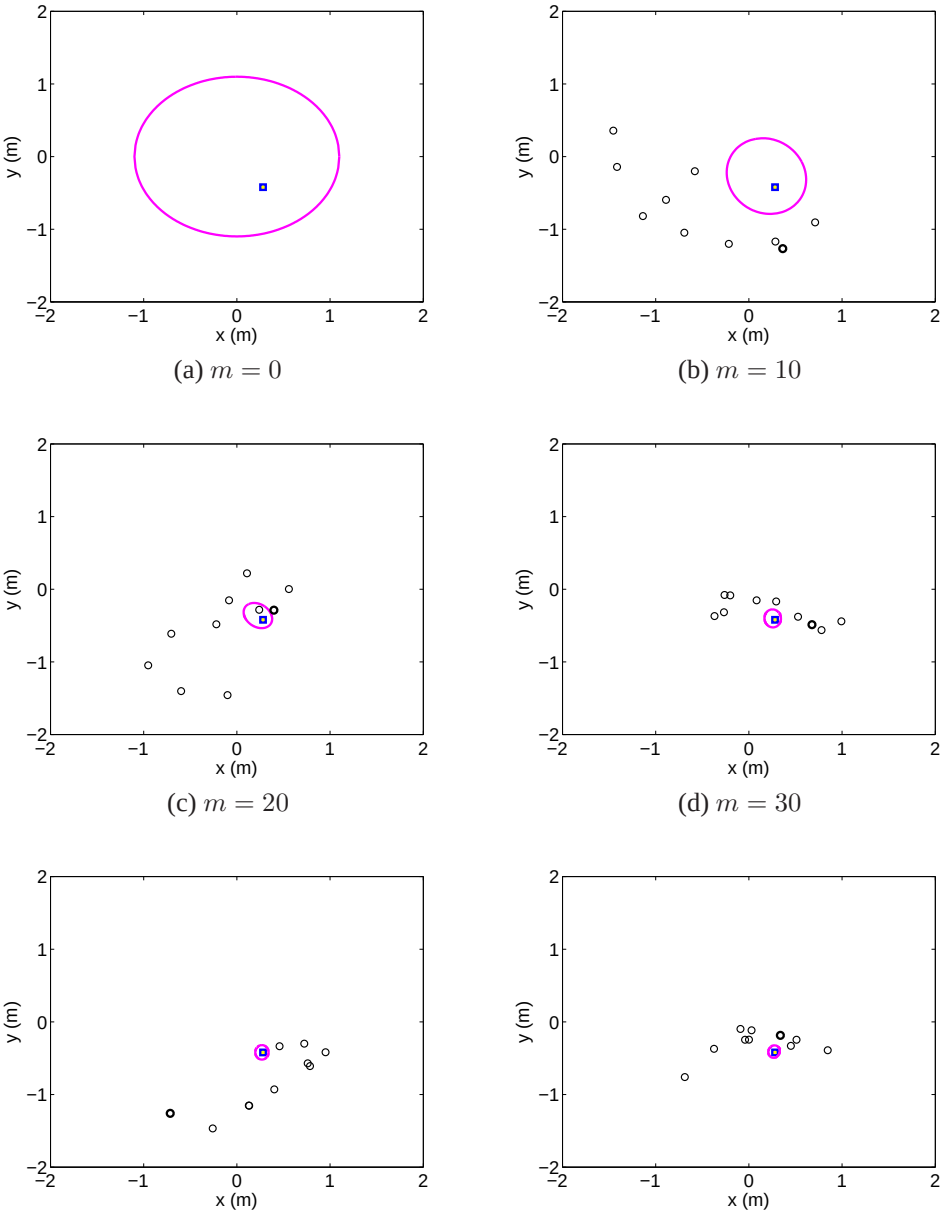

(a) $m = 0$ (b) $m = 10$

(c) $m = 20$ (d) $m = 30$

(e) $m = 40$ (f) $m = 50$

Figure B.5: Adaptive sensing trajectory

The MAG *equipped vehicle is moved according to adaptive sensing. Each plot shows the last 10 measurement locations with the most recent measurement emphasized. Adaptive sensing quickly locates the target and centers the search around that location.*

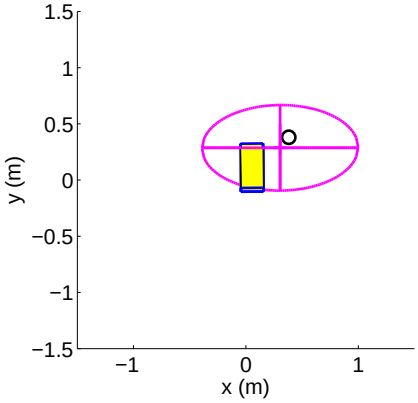

(a) Adaptive sensing $m = 0$

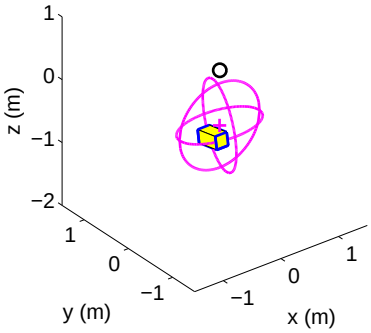

(b) Adaptive sensing $m = 0$

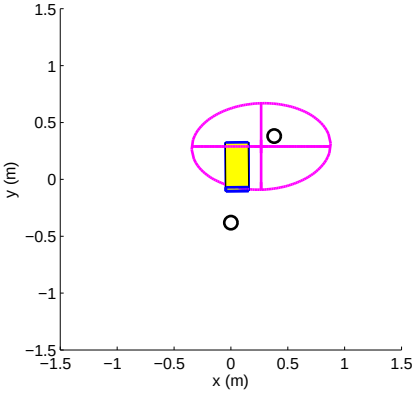

(c) Adaptive sensing $m = 1$

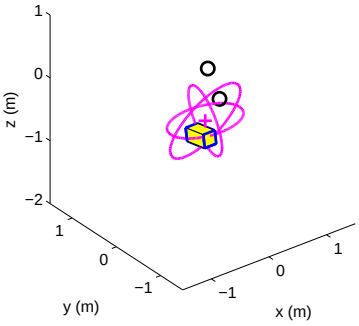

(d) Adaptive sensing $m = 1$

Figure B.6: Adaptive sensing with real data for 6D estimation, part 1

This uses real sensor data for the estimation procedure. The measurements and sensor locations are taken from a single data set. The left and right columns are respectively the top down view and isometric view of the scene.

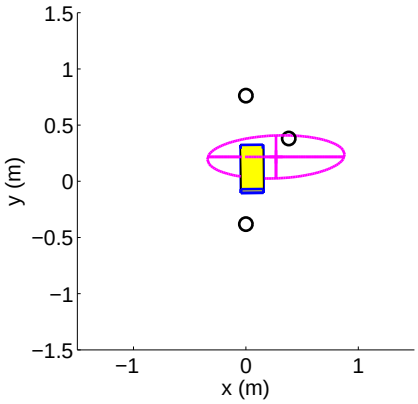

(a) Adaptive sensing $m = 2$

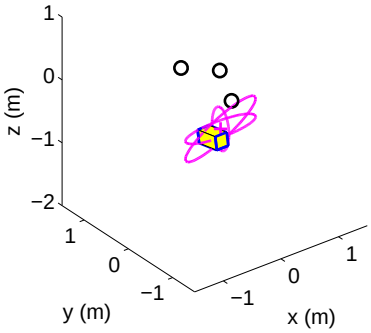

(b) Adaptive sensing $m = 2$

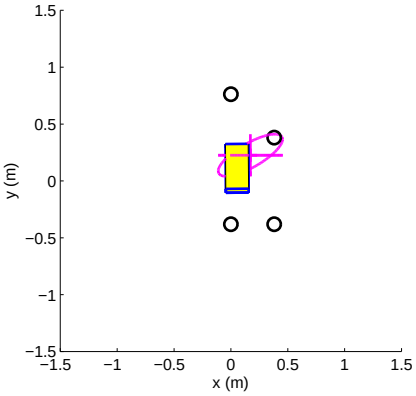

(c) Adaptive sensing $m = 3$

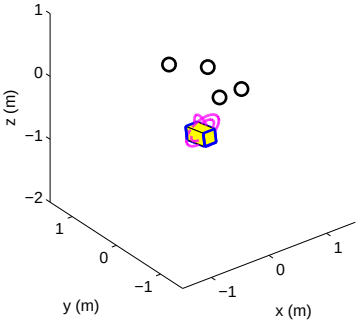

(d) Adaptive sensing $m = 3$

Figure B.7: Adaptive sensing with real data for 6D estimation, part 2

This is a continuation of the previous adaptive sensing plot.

Bibliography

[1] *Electromagnetic induction and magnetic sensor fusion for enhanced UXO target classification*, Tech. Report UX-9812, Environmental security technology certification program (ESTCP), 2004.

[2] *Survey of munitions response technologies*, Tech. report, The Environmental Security Technology Certification Program (ESTCP), The Interstate Technology & Regulatory Council (ITRC), The Strategic Environmental Research and Development Program (SERDP), June 2006.

[3] Francesco Amigoni and Vincenzo Caglioti, *An information-based criterion for efficient robot map building*, IEEE International Symposium on Virtual Environments, Human-Computer Interfaces and Measurement Systems (VECIMS), 27-29 July 2003, pp. 184–189.

[4] Chi O. Ao and Henning Braunisch, *Broadband electromagnetic induction response form conducting and permeable spheroids*, Detection and Remediation Technologies for Mines and Minelike Targets VI, vol. 4394, SPIE, 2001, pp. 1304–1315.

[5] Chi O. Ao, Henning Braunisch, Kevin O'Neill, and Jin A. Kong, *Quasi-magnetostatic solution for a conducting and permeable spheroid*, IEEE International Geoscience and Remote Sensing Symposium (IGARSS), vol. 4, 2000, pp. 1418–1420.

[6] ———, *Quasi-magnetostatic solution for a conducting and permeable spheroid with arbitrary excitation*, IEEE Transactions on Geoscience and Remote Sensing **40** (2002), no. 4, 887–897.

[7] Benjamin E. Barrowes, Kevin O'Neill, Tomasz M. Grzegorczyk, Xudong Chen, and Jin A. Kong, *Broadband analytical magnetoquasistatic electromagnetic induction solution for a conducting and permeable spheroid*, IEEE Transactions on Geoscience and Remote Sensing **42** (2004), no. 11, 2479–2489.

[8] Chet Bassani, *SAIC marine unexploded ordnance (UXO) survey system*, IEEE Oceans 2008, IEEE, September 2008.

[9] Thomas H. Bell, *Geo-location requirements for UXO discrimination*, Geolocation Workshop, 2005.

[10] Thomas H. Bell, Bruce J. Barrow, and Jonathan T. Miller, *Subsurface discrimination using electromagnetic induction sensors*, IEEE Transactions on Geoscience and Remote Sensing **39** (2001), no. 6, 1286–1293.

[11] Laurens Sander Beran, *Classification of unexploded ordnance*, Master's thesis, The University of British Columbia, March 2005.

[12] Stephen Billings, *Discrimination and classification of buried unexploded ordnance using magnetometry*, Geoscience and Remote Sensing, IEEE Transactions on **42** (2004), no. 6, 1241–1251.

[13] Stephen Billings and David Wright, *Optimal total-field magnetometer configuration for near-surface applications*, Leading Edge **28** (2009), no. 5, 522–527.

[14] Miro Bosnar, *Why did Geonics Limited build the EM61-MK2? Comparisons between EM61-MK2 and EM61*, Tech. report, Geonics Limited, March 2001.

[15] Sheldon Breiner, *Application manual for portable magnetometers*, Tech. report, Geometrics, 1999.

[16] H. Robert Burger, Anne F. Sheehan, and Craig H. Jones, *Introduction to applied geophysics : exploring the shallow subsurface*, W.W. Norton, New York, 2006.

[17] Diane M. Cargile, Hollis H. Bennett, Ricky A. Goodson, Tere' A. DeMoss, and Ernesto R. Cespedes, *Advanced UXO detection/discrimination technology demostration - Kaho'olawe, Hawaii*, Tech. Report TR-04-1, US Army Corps of Engineers: Engineer Research and Deveopment Center: Environmental Laboratory, Environmental Security Technology Certification Program, March 2004.

[18] Lawrence Carin, Nilanjan Dasgupta, and Hui Liao, *Optimal sensor management for next-generation EMI systems*, Tech. Report MM-1591, Strategic Enviromental Research & Development Program, June 2008.

[19] T.H. Chung, J.W. Burdick, and R.M. Murray, *A decentralized motion coordination strategy for dynamic target tracking*, Proc. IEEE International Conference on Robotics and Automation ICRA 2006, 2006, pp. 2416–2422.

[20] Leslie M. Collins, Ping Gao, and Lawrence Carin, *An improved Bayesian decision theoretic approach for land mine detection*, IEEE Transactions on Geoscience and Remote Sensing **37** (1999), no. 2, 811–819.

[21] Leslie M. Collins, Lisa G. Huettel, William A. Simpson, and Stacy L. Tantum, *Sensor fusion of EMI and GPR data for improved land mine detection*, Detection and Remediation Technologies for Mines and Minelike Targets VII **4742** (2002), no. 1, 872–879.

[22] Leslie M. Collins, Yan Zhang, Jing Li, Hua Wang, Lawrence Carin, Sean J. Hart, Susan L. Rose-Pehrsson, Herbert H. Nelson, and Jim R. McDonald, *A comparison of the performance of statistical and fuzzy algorithms for unexploded ordnance detection*, IEEE Transactions on Fuzzy Systems **9** (2001), no. 1, 17–30.

[23] Thomas M. Cover and Joy A. Thomas, *Elements of information theory*, Wiley-Interscience Publication, 1991.

[24] Matthew Dock, Mark Fisher, and Colin Cumming, *Novel detection apparatus for locating underwater unexploded ordnance*, Fifth International Symposium Mine Warfare Association, April 2002.

[25] Robert C. Doheny, Sean Burke, Roger Cresci, Peter Ngan, Richard Walls, and Jeff Chernoff, *Handheld standoff mine detection system (HSTAMIDS) field evaluation in Namibia*, Detection and Remediation Technologies for Mines and Minelike Targets XI **6217** (2006), no. 1.

[26] William E. Doll, T. Jeffrey Gamey, Les P. Beard, David T. Bell, J. S. Holladay, J. E. Nyquist, and J. Llopis, *Development and evaluation of a second-generation airborne electromagnetic system for detection of unexploded ordnance*, Symposium on the Application of Geophysics to Environmental and Engineering Problems, 2002.

[27] John S. Foster, James Brabham, Marvin D. Brailsford, Bert Fowler, Robert Frosch, Roy Goodwin, Richard H. Johnson, Gene H. McCall, Mike Myatt, Lenny Siegel, Drexel Smith, Lewis D. Walker, George Whitesides, and Monty Mathews, *Unexploded ordnance (UXO) clearance, active range UXO clearance, and explosive ordnance disposal (EOD) programs*, Tech. report, Defense Science Board Task Force, Office of the Under Secretary of Defense for Acquisition & Technology, Washington, D.C., April 1998.

[28] Eric W. Frew, *Trajectory design for target motion estimation using monocular vision*, Ph.D. thesis, Stanford University, Stanford, CA, August 2003.

[29] Eric W. Frew and Steve Rock, *Exploratory motion generation for monocular vision-based target localization*, IEEE Aerospace Conference, vol. 7, 9-16 March 2002, pp. 3633–3643.

[30] Geometrics, *Total field magnetometer performance published specifications and what they means*, January 2000.

[31] Geometrics, *G-858 MagMapper with AG114*, 2004.

[32] Geonics Limited, *Metal detectors: Time domain metal detection*.

[33] Geonics Limited, *Operating instructions EM61MK2a*, 1.36 ed., February 2003.

[34] Robert E. Grimm, *Triaxial modeling and target classification of multichannel multi-component em data for uxo discrimination*, Journal of Environmental and Engineering Geophysics **8** (2003), no. 4, 239–250.

[35] Ben Grocholsky, *Information-theoretic control of multiple sensor platforms*, Ph.D. thesis, The University of Sydney, Sydney, March 2002.

[36] Vijay Gupta, Timothy H. Chung, Babak Hassibi, and Richard M. Murray, *On a stochastic sensor selection algorithm with applications in sensor scheduling and sensor coverage*, Automatica **42** (2006), no. 2, 251–260.

[37] Gabriel M. Hoffmann, *Autonomy for sensor-rich vehicles: Interaction between sensing and control actions*, Ph.D. thesis, Stanford University, September 2008.

[38] Gabriel M. Hoffmann and Claire J. Tomlin, *Mobile sensor network control using mutual information methods and particle filters*, Submitted to IEEE Transactions on Automatic Control (2008).

[39] Michael A Jr. Houlemard, *Annual report: FY 2000-2001*, Tech. report, Fort Ord Resuse Authority, June 2001.

[40] Andreas Huster, *Relative position sensing by fusion monocular vision and inertial rate sensors.*, Ph.D. thesis, Stanford University, Stanford, CA, July 2003.

[41] Simon J. Julier, Jeffrey K. Uhlmann, and Hugh F. Durrant-Whyte, *A new approach for filtering nonlinear systems*, American Control Conference (ACC), 1995, pp. 1628–1632.

[42] Michael Kalandros and Lucy Y. Pao, *Covariance control for multisensor systems*, IEEE Transactions on Aerospace and Electonic Systems **38** (2002), no. 4, 1138–1157.

[43] ———, *Multisensor covariance control strategies for reducing bias effects in interacting target scenarios*, IEEE Transactions on Aerospace and Electonic Systems **41** (2005), no. 1, 153–173.

[44] Alexander A. Kaufman, *Geophysical field theory and method, part a*, International Geophysics, vol. 49, Academic Press, Inc, 1992.

[45] Jinwhan Kim and Stephen Rock, *Stochastic feedback controller design considering the dual effect*, AIAA Guidance, Navigation, and Control Conference and Exhibit, August 2006.

[46] Andrew T. Klesh, Anouck R. Girad, and Pierre T. Kabamba, *Real-time path planning for time-optimal exploration*, AIAA Guidance, Navigation and Control Conference and Exhibit, August 2008.

[47] Mark P. Kolba and Leslie M. Collins, *The effects of uncertainty and uncertainty modeling on information-based sensor manager performance*, Detection and Remediation Technologies for Mines and Minelike Targets XI **6217** (2006), no. 1.

[48] Mark P Kolba and Leslie M. Collins, *Information-theoretic sensor management for multimodal sensing*, IEEE International Conference on Geoscience and Remote Sensing Symposium (IGARSS), 2006, pp. 3935–3938.

[49] Mark P. Kolba and Leslie M. Collins, *Information-based sensor management in the presensce of uncertainty*, IEEE Transactions on Singal Processing **55** (2007), no. 6, 2731–2735.

[50] ———, *Managing landmine detection sensors: results from application to AMDS data*, Detection and Remediation Technologies for Mines and Minelike Targets XII, vol. 6553, SPIE, April 2007.

[51] Mark P. Kolba and Leslie M. Collins, *Sensor management for static target detection with non-binary sensor observations and observation uncertainty*, IEEE/SP 14th Workshop on Statistical Signal Processing (SSP), 2007, pp. 74–78.

[52] Chris Kreucher and Kevin Carter, *An information theoretic approach to processing management*, IEEE International Conference on Acoustics, Speech and Signal Processing (ICASSP), March 31–April 4 2008, pp. 1869–1872.

[53] Jacob Willem Langelaan, *State estimation for autonomous flight in cluttered environments*, Ph.D. thesis, Stanford University, March 2006.

[54] Deok-Jin Lee, *Unscented information filtering for distributed estimation and multiple sensor fusion*, AIAA Guidance, Navigation and Control Conference and Exhibit, August 2008.

[55] Xuejun Liao and L. Carin, *Application of the theory of optimal experiments to adaptive electromagnetic-induction sensing of buried targets*, **26** (2004), no. 8, 961–972.

[56] Andrew Logothetis, Alf Isaksson, and Robin J. Evans, *An information theoretic approach to observer observer path design for bearings-only tracking*, 36th Conference on Decision & Control, no. 4, 1997, pp. 3132–3137.

[57] Jacqueline MacDonald, J.R. Lockwood, John McFee, Thomas Altshuler, Thomas Broach, Lawrence Carin, Russell Harmon, Carey Rappaprt, Waymond Scott, and Richard Weaver, *Alternatives for landmine detection*, RAND Corporation, 2003.

[58] Jacqueline MacDonald and Carmen Mendez, *Unexploded ordnanace cleanup costs: Implications of alternative protocols*, RAND Corporation, 2005.

[59] MATLAB, *http://www.mathworks.com/*, June 2010.

[60] Larry Matthies, Erann Gat, Reid Harrison, Brian Wilcox, Richard Volpe, and Todd Litwin, *Mars microrover navigation: Performance evaluation and enhancement*, Autonomous Robots **2** (1995), 433–440.

[61] James D. McNeill and Miro Bosnar, *Application of TDEM techniques to metal detection and discrimination: A case history with the new Geonics EM-63 fully time-domain metal detector*, Tech. Report TN-32, Geonics Limited, April 2000.

[62] Martin Misakian, *Equations for the magnetic field produced by one or more rectangular loops of wire in the same plane*, Journal of Research on the National Institute of Standards and Technology **105** (2000), no. 4, 557–564.

[63] Frank Morrison, Torquil Smith, Alex Becker, and Erika Gasperikova, *Detection and classification of buried metallic objects*, Tech. Report UX-1225, Lawrence Berkeley National Laboratory, March 2005.

[64] DENIX Naval Explosive Ordnanace Disposal Technology Division, *Unexploded ordnance (UXO): An overview October 1996*, Tech. report, UXO Countermeasures Department, 1996.

[65] Frank III Navish and Michael May, *Autonomous mine detection sensors (AMDS)*, Detection and Remediation Technologies for Mines and Minelike Targets XI **6217** (2006), no. 1.

[66] Herb Nelson, Katherine Kaye, and Anne Andrews, *Estcp pilot program classification approaches in munitions response*, Tech. report, Environmental Security Technology Certification Program, November 2008.

[67] Herb H. Nelson and Jim R. McDonald, *Multisensor towed array detection system for UXO detection*, Geoscience and Remote Sensing, IEEE Transactions on **39** (2001), no. 6, 1139–1145.

[68] Herb H. Nelson, Jim R. McDonald, and David Wright, *Airborne UXO surveys using the MTADS*, Tech. report, Naval Research Laboratory, April 2005.

[69] Peter Ngan, Sean Burke, Roger Cresci, Joseph N. Wilson, Paul Gader, and Dominic K. C. Ho, *Region processing algorithm for HSTAMIDS*, Detection and Remediation Technologies for Mines and Minelike Targets XI **6217** (2006), no. 1.

[70] Stephen J. Norton, *Ordnance/clutter discrimination by broadband electromagnetic induction*, Tech. Report UX-1323, Strategic Environmental Research and Development Program (SERDP), December 2003.

[71] Clark F. Olson, Larry H. Matthies, Marcel Schoppers, and Mark W. Maimone, *Rover navigation using stereo ego-motion*, Robotics and Autonomous Systems **43** (2003), 215–229.

[72] Ford Ord, *The ordnance detection and discrimination study*, Tech. report, Ford Ord.

[73] Leonard R. Pasion and Douglas W. Oldenberg, *Locating and characterizing unexploded ordnance using time domain electromagnetic induction*, Tech. Report ERDC/GSL TR-01-10, U.S. Army Corps of Engineers, 2001, Geophysical Inversion Facility UBC.

[74] Leonard Rodriguez Pasion, *Detecting unexploded ordnance with time domain electromagnetic induction*, Master's thesis, The University of British Columbia, 1999.

[75] _____, *Inversion of time domain electromagnetic data for the detection of unexploded ordnance*, Ph.D. thesis, The University of British Columbia, 2007.

[76] Laura Perea, Jonathan P. How, Louis Breger, and Pedro Elosegui, *Nonlinearity in sensor fusion: divergence issues in EKF, modified truncated SOF, and UKF*, AIAA Guidance, Navigation and Control Conference and Exhibit, AIAA, 20-23 August 2007.

[77] Rich Phillips and John Zarrella, *Live bombs haunt Orlando neighborhood*, CNN, 2008.

[78] Pedro Piniés, Todd Lupton, Salah Sukkarieh, and Juan D. Tardós, *Inertial aiding of inverse depth slam using a monocular camera*, Robotics and Automation, 2007 IEEE International Conference on, 10-14 April 2007, pp. 2797–2802.

[79] Pedro Piniés and Juan D. Tardós, *Fast localization of avalanche victims using sum of Gaussians*, IEEE International Conference on Robotics and Automation (ICRA), 15-19 May 2006, pp. 3989–3994.

[80] Pedro Piniés, Juan D. Tardós, and José Neira, *Localization of avalanche victims using robocentric SLAM*, IEEE/RSJ International Conference on Intelligent Robots and Systems, October 2006, pp. 3074–3079.

[81] Battelle-Oak Ridge and Oak Ridge National Laboratory, *Final report: Airborne geophysical survey, Fort Ord, California. January 29-February 17, 2005*, September 30 2005, Prepared for Fort Ord BRAC Office, Presdio of Monterey, Monterey Country, CA and U.S. Army Engineer Research and Development Center, Vicksburg, MS.

[82] Paul Rigby and Stefan B. Williams, *Adaptive sensing for localisation of an autonomous underwater vehicle*, Australasian Conference on Robotics and Automation (Claude Sammut, ed.), December 2005.

[83] Allison Ryan, *Information-theoretic tracking control based on particle filter estimate*, AIAA Guidance, Navigation and Control Conference and Exhibit, August 2008.

[84] Waymond R. Scott, Jr. and James S. Martin, *An experimental model of a acousto-electromagnetic sensor for detecting land mines*, IEEE Antennas and Propagation Society International Symposium, vol. 2, 21-26 June 1998, pp. 978–981.

[85] Irma Shamatava, Fridon Shubitidze, Chi-Chih Chen, Hyoun-Sun Youn, Kevin O'Neill, and Keli Sun, *Potential benefits of combining EMI and GPR for enhanced UXO discrimination at highly contaminated sites*, Detection and Remediation Technologies for Mines and Minelike Targets IX **5415** (2004), no. 1, 1201–1210.

[86] Fridon Shubitidze, Benjamin E. Barrowes, Kevin O'Neill, Irma Shamatava, Jaun P. Fernández, and Keli Sun, *NSMC for UXO discrimination in cases with overlapping signatures*, Detection and remediation technologies for mines and minelike targets XII, vol. 6553, SPIE, April 2007.

[87] Fridon Shubitidze, Benjamin E. Barrowes, Kevin O'Neill, Irma Shamatava, and Juan P. Fernández, *A combined NSMC and pole series expansion approach for UXO discrimination*, Detection and remediation technologies for mines and minelike targets XII, vol. 6553, SPIE, April 2007.

[88] Fridon Shubitidze, Benjamin E. Barrowes, Kevin O'Neill, Irma Shamatava, Juan P. Fernández, Keli Sun, and Keith D. Paulsen, *The generalized SEA to UXO discrimination in geophysical environments producing EMI response*, Detection and Remediation Technologies for Mines and Minelike Targets XI **6217** (2006), no. 1.

[89] Fridon Shubitidze, Eugene Demidenko, Benjamin E. Barrowes, Irma Shamatava, Juan P. Fernández, and Kevin O'Neill, *Combining dipole and mixed model approaches for UXO discrimination*, Detection and Sensing of Mines, Explosive Objects, and Obscured Targets XIII, vol. 6953, SPIE, April 2008.

[90] Janet E. Simms, Robert J. Larson, William L. Murphy, and Dwain K. Butler, *Guidlines for planning unexploded ordnance (UXO) detection surveys*, Tech. Report ERDC/GSL TR-04-8, US Army Corps of Engineers: Engineer Research and Development Center, Geotechnical and Structures Laboratory, August 2004.

[91] J. Torquil Smith and H. Frank Morrison, *Approximating spheroid inductive responses using spheres*, Geophysics **71** (2006), no. 2, G21–G25.

[92] Kenneth Smith, *Cesium optically pumped magnetometers*, Tech. Report M-TR91, Geometrics, 1997.

[93] John M. Stanley and Malcolm K. Cattach, *Magnetometer systems for exploded ordnance detection on land*, Tech. report, Geophysical Technology Limited, 2002.

[94] Dan Steinhurst, Nagi Khadr, Bruce Barrow, and Herb Nelson, *Moving platform orientation for an unexploded ordnance discrimination system*, GPS World **16** (2005), no. 5, 28–34.

[95] Vivek A. Sujan and Steven Dubowsky, *Efficient information-based visual robotic mapping in unstructured environments*, The International Journal of Robotics Research **24** (2005), no. 4, 275–293.

[96] Keli Sun, Kevin O'Neill, Benjamin. E. Barrowes, Juan Pablo Fernández, Fridon Shubitidze, Irma Shamatava, and Keith D. Paulsen, *Dumbbell dipole model and its application in UXO discrimination*, Detection and Remediation Technologies for Mines and Minelike Targets XI **6217** (2006), no. 1.

[97] Gabriel Terejanu, Tarunraj Singh, and Peter D. Scott, *Unscented Kalman filter/smoother for a CBRN puff-based dispersion model*, 10th International Conference on Information Fusion (Tarunraj Singh, ed.), 2007, pp. 1–8.

[98] Sebastian Thrun, Wolfram Burgard, and Dieter Fox, *Probabilistic robotics*, The MIT Press, 2005.

[99] John Tisdale, Zu Kim, and J. Karl Hedrick, *An autonomous system for cooperative search and localization using unmanned vehicles*, AIAA Guidance, Navigation and Control Conference and Exhibit, August 2008.

[100] Rudolph van der Merwe, *Sigma-point Kalman filters for probabilistic inference in dynamic state-space models*, Ph.D. thesis, OGI School of Science & Engineering, Oregon Health & Science University, April 2004.

[101] Rudolph van der Merwe and Eric A. Wan, *The square-root unscented Kalman filter for state and parameter estimation*, IEEE International Conference on Acoustics, Speech, and Signal Processing (ICASSP), May 2001.

[102] Tom Vercauteren and Xiaodong Wang, *Decentralized sigma-point information filters for target tracking in collaborative sensor networks*, IEEE Transactions on Signal Processing **53** (2005), no. 8, 2997–3009.

[103] William W. Whitacre, George Tillinghast, and Mark E. Campbell, *Information-theoretic optimization of periodic orbits for persistent cooperative geolocation*, AIAA Guidance, Navigation and Control Conference and Exhibit, August 2008.

[104] Alan S. Willsky, *A survey of design methods for failure detection in dynamic systems*, Automatica **12** (1976), 601–611.

[105] Beijia Zhang, Kevin O'Neill, Tomasz M. Grzegorczyk, and Jin Au Kong, *Use of EMI response coefficients from spheroidal excitation and scattering modes to classify objects via SVM*, Detection and Remediation Technologies for Mines and Minelike Targets XI **6217** (2006), no. 1.

[106] Fumin Zhang and Naomi E. Leonard, *Generating contour plots using multiple sensor platforms*, IEEE Swarm Intelligence Symposium (SIS), 8-10 June 2005, pp. 309–316.

[107] Yan Zhang, L. Collins, Haitao Yu, C.E. Baum, and L. Carin, *Sensing of unexploded ordnance with magnetometer and induction data: Theory and signal processing*, IEEE Transactions on Geoscience and Remote Sensing **41** (2003), no. 5, 1005–1015.

[108] Yan Zhang, Leslie M. Collins, and Lawrence Carin, *Unexploded ordnance detection using Bayesian physics-based data fusion*, Integrated Computer-Aided Engineering **10** (2003), 231–247.

[109] Youmin Zhang and X. Rong Li, *Detection and diagnosis of sensor and actuator failures using IMM estimator*, IEEE Transactions on Aerospace and Electronic Systems **34** (1998), no. 4, 1293–1313.

[110] Feng Zhao, Jaewon Shin, and J. Reich, *Information-driven dynamic sensor collaboration*, IEEE Signal Processing Mazagine **19** (2002), no. 2, 61–72.